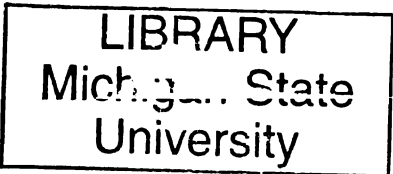




2
2009



This is to certify that the
dissertation entitled

**A VISCOELASTIC FINITE DIFFERENCE TIME DOMAIN
MODEL OF HUMAN THORAX TO DEVELOP AND VALIDATE
SOURCE LOCALIZATION ALGORITHMS**

presented by

Sridhar Ramakrishnan

has been accepted towards fulfillment
of the requirements for the

Doctoral degree in Electrical Engineering

Sathya Vepi

Major Professor's Signature

August 7, 2009

Date

PLACE IN RETURN BOX to remove this checkout from your record.
TO AVOID FINES return on or before date due.
MAY BE RECALLED with earlier due date if requested.

DATE DUE	DATE DUE	DATE DUE
APR 23 2011 OCT 23 2011		

**A VISCOELASTIC FINITE DIFFERENCE TIME DOMAIN MODEL OF
HUMAN THORAX TO DEVELOP AND VALIDATE SOURCE
LOCALIZATION ALGORITHMS**

By

Sridhar Ramakrishnan

A DISSERTATION

**Submitted to
Michigan State University
in partial fulfillment of the requirements
for the degree of**

DOCTOR OF PHILOSOPHY

Electrical Engineering

2009

ABSTRACT

A VISCOELASTIC FINITE DIFFERENCE TIME DOMAIN MODEL OF HUMAN THORAX TO DEVELOP AND VALIDATE SOURCE LOCALIZATION ALGORITHMS

By

Sridhar Ramakrishnan

Auscultation sounds offer a rich source of diagnostic information that could potentially be used to detect a vast number of heart and lung pathologies non-invasively. Recent times have seen efforts directed towards the possibility of using an array of acoustic sensors for the localization of sounds, thereby leading to improved diagnosis. However, a majority of the existing array processing and inverse-source solution schemes proposed to date rely on simplifying assumptions, and many of the factors that contribute to violation of the assumptions, such as heterogeneity of the thoracic cavity, shear wave contributions, extreme near-field conditions, to name a few, are not taken into account. This work presents a test bed capable of simulating the sound distribution around the thorax. Specifically, a finite-difference time-domain (FDTD) forward model of the human thorax that solves the viscoelastic wave equations while taking the intrinsic anatomy and the associated viscoelastic properties of the various tissues and structures into account is presented. The test bed can be employed to develop and validate various array signal processing algorithms and inverse problem techniques used for localizing sound. Test results demonstrating the utility as well as effectiveness of the test bed are presented.

ACKNOWLEDGMENTS

I wish to express my sincere gratitude to my advisor Dr. Satish Udpa and my committee members Dr. Lalita Udpa, Dr. Joe Hauptman, and Dr. Ramakrishna Mukkamala for their guidance and support in my PhD study. Their advice on technical matters, encouragement, motivation and constructive criticism were greatly acknowledged. I owe special thanks to Dr. Satish Udpa for having bolstered my confidence at every stage of my graduate student life and guiding me in making wise career decisions.

Throughout the period of my graduate study, I was financially supported by various research projects undertaken by Dr. Satish Udpa, Dr. Lalita Udpa and Dr. Pradeep Ramuhalli. This support, specially the one provided by Electric Power Research Institute, is gratefully acknowledged. Being a member of the Nondestructive Evaluation Laboratory, I feel gifted having had an opportunity to work with a team of dedicated graduate students, interns, visiting scholars and professors over the past 6 years on different research problems, which have not only widened my academic experience but have also improved my interpersonal skills and instilled team ethics in me. I sincerely thank all my laboratory members for thus having enriched my graduate student experience. I also acknowledge Prof. Antonello Tamburrino for his tutoring in the Inverse Problems course and his valuable advice during my PhD.

I would like to thank the Department of Electrical and Computer Engineering, the High Performance Computing Center and the College of Engineering at Michigan State University for providing the best research resources and facilities. I thank the entire staff

of Electrical and Computer Engineering, Office of the Dean of College of Engineering, OISS, DECS and Graduate School for their valuable timely assistance on various occasions. I would like to specially acknowledge Linda Clifford for not only having assisted me in all the paper work throughout the course of my graduate studies but also for helping all of our laboratory members to forge family-like bonds amongst our group.

Finally, I wish to express my heartfelt gratitude to my parents, my sister and my brother-in-law for their constant support and encouragement. Without their support this dissertation would not have been possible.

TABLE OF CONTENTS

LIST OF TABLES.....	viii
LIST OF FIGURES	x
NOMENCLATURE	xv
CHAPTER 1	1
INTRODUCTION	1
1.1 General.....	1
1.2 Dissertation layout.....	3
CHAPTER 2	4
PRIOR WORK.....	4
2.1 Introduction	4
2.2 Acoustic Modeling Studies of the Thorax.....	5
2.3 Signal Processing Methods for Acoustic Diagnostics.....	10
CHAPTER 3	12
VISCOELASTIC FDTD MODEL FOR HUMAN THORAX.....	12
3.1 Introduction	12
3.2 Governing Equations	12
3.2.1 Elastodynamic Equations	13
3.2.2 Popular Viscoelastic Models	15
3.2.3 Viscoelastic Wave Propagation Equation	16
3.3 Thorax Anatomy and Material Properties	19
3.4 Boundary Conditions.....	25
3.4.1 Concept of PML.....	25
3.4.2 Recursive Integration PML	26
3.5 Source Model and Initial Conditions.....	30
3.6 Finite-Difference Time-Domain Implementation	33
3.6.1 Discretization scheme	33
3.6.2 Numerical Stability	38
3.7 Numerical Results.....	40
3.7.1 Validation of FDTD codes.....	40
3.7.1.1 Comparison with analytical solution.....	40
3.7.1.2 Comparison with results published in literature.....	46
3.7.2 Simulation results on human thorax.....	48
3.7.3 Wave Propagation Characteristics.....	57
3.8 Effects of Anatomical Variations	60
3.8.1 Effects of ribs and shear elasticity of tissues.....	60
3.8.2 Effect of size of thorax.....	62

CHAPTER 4	64
STUDY OF SOUNDS UNDER PNEUMOTHORAX CONDITIONS	64
4.1 Introduction	64
4.2 Simulation of Pneumothorax	66
4.3 Results and Conclusion	68
CHAPTER 5	74
SOURCE LOCALIZATION	74
5.1 Introduction	74
5.1.1 Beamforming concept	75
5.1.2 Near-Field Propagation Model	77
5.2 Near-Field Propagation Model based Source Localization Algorithms.....	80
5.2.1 Multiple Signal Classification (MUSIC).....	80
5.2.2 Conventional Focused Beamformer (CFB).....	81
5.2.3 Linearly Constrained Minimum Variance Beamformer (LCMV).....	82
5.3 Algorithm Parameters.....	84
5.4 Algorithm Testing Procedure	89
5.5 Results using the Near-Field Propagation Model based Techniques	92
5.5.1 Homogeneous Thorax.....	92
5.5.2 Mitral Valve Source.....	96
5.5.3 Right Lung Source	101
5.5.4 Discussion	105
5.6 Transfer Function based Source Localization Algorithms	110
5.6.1 Transfer Function – Source Waveform Energy (SWE).....	111
5.6.2 Transfer Function – MUSIC.....	112
5.6.3 Transfer Function – CFB.....	113
5.6.4 Transfer Function – LCMV	113
5.7 Results using Transfer Function based Techniques	115
5.7.1 Mitral Valve Source.....	115
5.7.2 Right Lung Source	118
5.7.3 Left Lung Source.....	121
5.7.4 Discussion	125
5.8 Methods to improve Near-Field Propagation Model based Techniques	127
5.8.1 Distributed Source Model	127
5.8.2 Preliminary results using Distributed Source Model Techniques	128
5.8.2.1 Homogeneous Thorax	128
5.8.2.2 Mitral Valve Source	132
5.9 Conclusion	137
CHAPTER 6	138
SUMMARY AND CONCLUSIONS	138
6.1 Summary.....	138
6.2 Conclusions and Future Work	140
REFERENCES	142

LIST OF TABLES

Table 3-1 Material properties (density, volume compressibility, shear elasticity, volume viscosity, shear viscosity) and longitudinal wave velocity c_p of the tissues that use the Voigt model of viscoelasticity in the thoracic cavity.	22
Table 3-2 Material properties (density, volume compressibility, volume viscosity, shear elasticity, shear viscosity) of air surrounding the thoracic cavity.	23
Table 3-3 Material properties (density, volume compressibility, shear elasticity, volume viscosity, shear viscosity), longitudinal wave velocity c_p and Young's modulus E of the spinal cord and intervertebral disc in the thoracic cavity.	23
Table 3-4 Material properties (density, volume compressibility, shear elasticity, resistance coefficient to normal and shear stresses), longitudinal wave velocity c_p and Young's modulus E of the ribs and scapula bone that use the Maxwell model of viscoelasticity in the thoracic cavity.	24
Table 5-1 Localization error ε in cm versus SNR in dB obtained in all three source localization algorithms using $\eta = 0$, for both pressure and velocity input signals in a homogeneous thoracic medium.	95
Table 5-2 Localization error ε in cm versus SNR in dB obtained in all three source localization algorithms using $\eta = 0$, for both pressure and velocity input signals for a mitral valve source.	100
Table 5-3 Localization error ε in cm versus SNR in dB obtained in all three source localization algorithms using $\eta = 1$, for both pressure and velocity input signals for a mitral valve source.	100
Table 5-4 Localization error ε in cm versus SNR in dB obtained in all three source localization algorithms using $\eta = 0$, for both pressure and velocity input signals for a right lung source.	104
Table 5-5 Localization error ε in cm versus SNR in dB obtained in all three source localization algorithms using $\eta = 1$, for both pressure and velocity input signals for a right lung source.	104
Table 5-6 Localization error ε in cm versus SNR in dB obtained in all three source localization algorithms using $\eta = 0$, for only pressure input signals in a homogeneous thoracic medium.	108

Table 5-7 Localization error ε in cm versus SNR in dB obtained in all four source localization algorithms for both pressure and velocity input signals for a mitral valve source..... 118

Table 5-8 Localization error ε in cm versus SNR in dB obtained in all four source localization algorithms for both pressure and velocity input signals for a right lung source..... 121

Table 5-9 Localization error ε in cm versus SNR in dB obtained in all four source localization algorithms for both pressure and velocity input signals for a left lung source. 124

Table 5-10 Localization error ε in cm versus SNR in dB obtained in all distributed source based algorithms using $\eta = 0$, for both pressure and velocity input signals in a homogeneous thoracic medium. 131

Table 5-11 Localization error ε in cm versus SNR in dB obtained in all distributed source based algorithms using $\eta = 0$, for both pressure and velocity input signals for a mitral valve source. 135

Table 5-12 Localization error ε in cm versus SNR in dB obtained in all distributed source based algorithms using $\eta = 1$, for both pressure and velocity input signals for a mitral valve source. 135

LIST OF FIGURES

Images in this thesis/dissertation are presented in color.

Figure 3-1 Photographic cross-sectional slice of the human thorax acquired from the Visible Human Project database [40], [41]	20
Figure 3-2 (a) Cross-sectional slice of human thorax partitioned into distinct anatomical regions, each tissue color-coded with a unique color (b) Corresponding color-code key to identify the different tissues	21
Figure 3-3 Staggered grid layout for the 2D velocity-stress FDTD scheme indicating the relative spatial and time indices at which the variables are computed	34
Figure 3-4 Geometry of the problem for validating the FDTD code. Black circles represent the array of receiver locations. Black cross represents the source location.	41
Figure 3-5 f_z components of the forcing functions (a) Gaussian first derivative forcing pulse (b) Sinusoidal forcing pulse	43
Figure 3-6 Comparison of v_x and v_z components obtained via FDTD to their corresponding analytical counterparts for the 1 kHz Gaussian first derivative forcing pulse (all color-bar units are in m/s)	44
Figure 3-7 Comparison of v_x and v_z components obtained via FDTD to their corresponding analytical counterparts for the 1 kHz sinusoidal forcing pulse (all color-bar units are in m/s)	45
Figure 3-8 Comparison of numerical FDTD with analytical results for a 1 kHz Gaussian first-derivative point forcing f_z source located at origin in a 2D homogeneous medium ($\rho = 1000 \text{ kg/m}^3$, $c_p = 1500 \text{ m/sec}$, $c_s = 500 \text{ m/sec}$) – Normalized v_z component of velocity at 11 receiver locations located at $z = 0.8 \text{ m}$ and $x = (-1 \text{ m to } 1 \text{ m, in steps of } 0.2 \text{ m})$	46
Figure 3-9 Elastic wave propagation results as presented by Collino <i>et al.</i> [58] – Snapshots of absolute velocity over the entire homogeneous domain caused due to an explosive source located at the top left corner of the domain	47
Figure 3-10 FDTD simulation results for the elastic wave propagation problem defined in Collino <i>et al.</i> [58] – Snapshots of absolute velocity over the entire domain caused due to an explosive source located at the top left corner of the domain	48
Figure 3-11 Source (white cross) and receiver (white circles and triangles) locations in the thoracic geometry. (The axes are in units of m).	50

Figure 3-12 A 300Hz Gaussian first derivative source signal f_z used in the FDTD simulations (a) Time waveform of the forcing signal (b) Corresponding Fourier spectrum.	52
Figure 3-13 Magnitude of source-to-receiver transfer functions (TF) for a source at the mitral valve location – TF plots at receiver #s 4, 8, 12, 16 and 20 in the 0-100 Hz frequency range	53
Figure 3-14 Magnitude of source-to-receiver transfer functions (TF) for a source at the mitral valve location – TF plots at receiver #s 4, 8, 12, 16 and 20 in the 100-400 Hz frequency range	54
Figure 3-15 Magnitude of source-to-receiver transfer functions (TF) for a source at the mitral valve location – TF image at all receivers in the 0-100 Hz frequency range	55
Figure 3-16 Magnitude of source-to-receiver transfer functions (TF) for a source at the mitral valve location – TF image at all receivers in the 100-400 Hz frequency range	56
Figure 3-17 Snapshots (at 3, 7, 15, 25 and 40 ms) of velocity v_x and v_z distributions in the entire thorax as a sound wave caused due to a 300 Hz Gaussian first-derivative forcing source propagates from the mitral valve location. (The axes on each of the subplots are in units of m and the color-bars have units of m/s)	59
Figure 3-18 Normal component of the velocity v_n at receiver #15 due to a 300 Hz Gaussian first-derivative forcing source at the mitral valve location under three cases – normal thorax, rib-less thorax and shear-less thorax	61
Figure 3-19 Normal component of the velocity v_n at receiver #12 due to a 300 Hz Gaussian first-derivative forcing source at the mitral valve location for three different thorax sizes ($L_x \times L_z$) – 35 cm X 25 cm, 30 cm X 20 cm and 40 cm X 30 cm	63
Figure 4-1 Anatomical simulation of a pneumothoracic air cavity on a 2D cross-sectional slice of the human thorax.....	66
Figure 4-2 Left column of images show the cross-sectional slice of the thorax for varying sizes of the pneumothoracic air pocket in the lung. The labels on the left side indicate the size of the air pocket. The right column of plots represent the corresponding amplitude of the source(o)-to-sensor(x) transfer functions.	69
Figure 4-3 Comparison of the amplitudes of the source-to-sensor transfer functions corresponding to varying sizes of the pneumothoracic air pocket	71
Figure 4-4 Comparison of amplitudes of difference of the transfer functions of varying degrees of pneumothoracic severity and that of a normal thorax.....	72
Figure 5-1 Concept of beamforming	76

Figure 5-2 Near-field propagation model.....	77
Figure 5-3 The outer white box corresponds to the x - z search space used in the algorithms. The inner white box shows the size of the finest cell used in the search.	85
Figure 5-4 Velocity c search values	86
Figure 5-5 Sensor index and locations of the 19 sensor sites used in the source localization algorithms	87
Figure 5-6 An illustration of noisy waveforms at 10 dB, 0dB and -10dB compared to the corresponding noiseless normalized pressure p and velocity v_n signals at four different receiver sites - #s 9, 25, 41 and 57.....	90
Figure 5-7 Location of the true source in the homogeneous thoracic medium is indicated by the white cross. The white circles correspond to the sensor locations used in the source localization codes.	93
Figure 5-8 Objective function images of all three source localization algorithms using $\eta = 0$ obtained on both pressure and velocity input signals at an SNR of 5 dB in a homogeneous thoracic medium. Both x and z axes of all images are in m. White cross indicates the true source location while the white circle corresponds to the estimated source location.....	94
Figure 5-9 Plot of localization error ε in m versus SNR in dB obtained in all three source localization algorithms using $\eta = 0$, for both pressure and velocity input signals in a homogeneous thoracic medium.....	95
Figure 5-10 Location of the true source at the mitral valve in the thoracic medium is indicated by the white cross. The white circles correspond to the sensor locations used in the source localization codes.....	97
Figure 5-11 Objective function images of all three source localization algorithms using $\eta = 1$ obtained on both pressure and velocity input signals at an SNR of 10 dB for a mitral valve source. Both x and z axes of all images are in m. White cross indicates the true source location while the white circle corresponds to the estimated source location.	98
Figure 5-12 Plot of localization error ε in m versus SNR in dB obtained in all three source localization algorithms using $\eta = 0$ (top row) and $\eta = 1$ (bottom row), for both pressure and velocity input signals for a mitral valve source.....	99
Figure 5-13 Location of the true source in the right lung of the thorax is indicated by the white cross. The white circles correspond to the sensor locations used in the source localization codes.....	101

Figure 5-14 Objective function images of all three source localization algorithms using $\eta = 1$ obtained on both pressure and velocity input signals at an SNR of 10 dB for a right lung source. Both x and z axes of all images are in m. White cross indicates the true source location while the white circle corresponds to the estimated source location. 102

Figure 5-15 Plot of localization error ϵ in m versus SNR in dB obtained in all three source localization algorithms using $\eta = 0$ (top row) and $\eta = 1$ (bottom row), for both pressure and velocity input signals for a right lung source..... 103

Figure 5-16 Location of the true source in the homogeneous thoracic medium is indicated by the white cross. The white circles correspond to the sensor locations used in the source localization codes. 106

Figure 5-17 Objective function images of all three source localization algorithms using $\eta = 0$ obtained on only the pressure input signals at an SNR of 5 dB in a homogeneous thoracic medium. Both x and z axes of all images are in m. White cross indicates the true source location while the white circle corresponds to the estimated source location. 107

Figure 5-18 All source and sensor locations considered for the transfer functions 111

Figure 5-19 Objective function images of all four source localization algorithms obtained on both pressure and velocity input signals at an SNR of 5 dB for a mitral valve source. Both x and z axes of all images are in m. White cross indicates the true source location while the white circle corresponds to the estimated source location..... 116

Figure 5-20 Plot of localization error ϵ in m versus SNR in dB obtained in all four source localization algorithms for both pressure and velocity input signals for a mitral valve source..... 117

Figure 5-21 Objective function images of all four source localization algorithms obtained on both pressure and velocity input signals at an SNR of 10 dB for a right lung source. Both x and z axes of all images are in m. White cross indicates the true source location while the white circle corresponds to the estimated source location..... 119

Figure 5-22 Plot of localization error ϵ in m versus SNR in dB obtained in all four source localization algorithms for both pressure and velocity input signals for a right lung source..... 120

Figure 5-23 Location of the true source in the left lung of the thorax is indicated by the white cross. The white circles correspond to the sensor locations used in the source localization codes. 122

Figure 5-24 Objective function images of all four source localization algorithms obtained on both pressure and velocity input signals at an SNR of 10 dB for a left lung source. Both x and z axes of all images are in m. White cross indicates the true source location while the white circle corresponds to the estimated source location..... 123

Figure 5-25 Plot of localization error ϵ in m versus SNR in dB obtained in all four source localization algorithms for both pressure and velocity input signals for a left lung source. 124

Figure 5-26 Distributed source model 128

Figure 5-27 Objective function images of all three distributed source based algorithms using $\eta = 0$ obtained on both pressure and velocity input signals at an SNR of 5 dB in a homogeneous thoracic medium. Both x and z axes of all images are in m. White cross indicates the true source location while the black diamond corresponds to the estimated source location. 130

Figure 5-28 Plot of localization error ϵ in m versus SNR in dB obtained in all distributed source based algorithms using $\eta = 0$, for both pressure and velocity input signals in a homogeneous thoracic medium. 131

Figure 5-29 Objective function images of all distributed source based algorithms using $\eta = 0$ obtained on both pressure and velocity input signals at an SNR of 5 dB for a mitral valve source. Both x and z axes of all images are in m. White cross indicates the true source location while the black diamond corresponds to the estimated source location. 133

Figure 5-30 Plot of localization error ϵ in m versus SNR in dB obtained in all distributed source based algorithms using $\eta = 0$ (top row) and $\eta = 1$ (bottom row), for both pressure and velocity input signals for a mitral valve source. 134

NOMENCLATURE

ρ	density
η	damping factor
\bar{v}	velocity vector
\bar{T}	stress tensor
\bar{f}	force per unit volume vector
S	strain components
c	constitutive parameters
(λ, μ)	Lamé constants
σ	stress
ε	strain
E	elastic modulus
$\tilde{\eta}$	viscosity
$\tilde{\eta}_M$	viscosity in Maxwell's model
$\tilde{\eta}_V$	viscosity in Voigt's model
v_l	particle velocity in l direction
T_{ll}	normal stress component in l direction
T_{xz}	shear stress component in x - z plane
γ_{ij}	resistance coefficient in the i - j direction
f_l	forcing functions in the l direction
λ_1	coefficient of volume compressibility
μ_1	coefficient of shear elasticity
λ_2	coefficient of volume viscosity
μ_2	coefficient of shear viscosity

ω	angular frequency
k	wave-number
ε_l	stretching function in the l direction
a_l	scaling factor of the stretching function
w_l	loss factor of the stretching function
S	stress-rate tensor
E	strain-rate tensor
S_{ij}	stress-rate tensor components
E_{ij}	strain-rate tensor components
d	thickness of PML
m	scaling order of the PML loss factor profile
R	theoretical reflection coefficient of PML
c_p	longitudinal wave velocity
f_0	center frequency of forcing function
(x_0, z_0)	x - z location coordinates of source
σ	standard deviation of Gaussian pulse
B	amplitude of forcing pulse
A	peak magnitude at center frequency
t_0	time-shift of Gaussian pulse
$1_{B(a)}$	unity disc with center (x_0, z_0) and radius a
Δx	grid step in x direction
Δz	grid step in z direction
Δt	grid step in time
Ω_{ij}	stress-rate cumulative sum components
Ψ_{ij}	strain-rate cumulative sum components

$c_{p,max}$	maximum longitudinal wave velocity
c_s	shear wave velocity
$c_{s,min}$	slowest shear wave speed
K_S	number of spatial sample points to track $c_{s,min}$
L_x	thorax dimension in x direction
L_z	thorax dimension in z direction
N_x	number of grid cells in x direction
N_z	number of grid cells in z direction
F_S	sampling frequency
v_n	normal component of velocity
TF	source-to-receiver transfer function
p	mean pressure
x_i	i^{th} sensor signal input to beamformer
\mathbf{x}	sensor signal input vector
N	number of sensors
w_i	beamformer weight of the i^{th} sensor
\mathbf{w}	beamformer weight vector
y	output signal of beamformer
\mathbf{y}	beamformer output vector
c	velocity of wave propagation
K	number of acoustic sources
r_{0k}	distance of k^{th} source from reference sensor
r_{ik}	distance of k^{th} source from i^{th} sensor
s_k	k^{th} source waveform
f	source waveform frequency

n_i	noise at the i^{th} sensor
a_k	near-field propagation model steering vector of k^{th} source
\mathbf{A}	near-field propagation model steering matrix
β	geometric spreading loss factor
η	exponential loss factor
\mathbf{R}	sensor data covariance matrix
v_k	k^{th} eigen vector of data covariance matrix
$a(r, \theta, \square)$	near-field propagation model steering vector corresponding to the location (r, θ, \square) in a 3D polar coordinate search space
$a(x, z)$	near-field propagation model steering vector corresponding to the location (x, z) in a 2D cartesian coordinate search space
P	objective function of the source localization algorithms
\mathbf{C}	constraint steering vector matrix
\mathbf{g}	constraint values vector
D_x	rectangular search space dimension in x direction
D_z	rectangular search space dimension in z direction
SNR	signal-to-noise ratio
ε	localization error
h_{kl}	k^{th} source-to- l^{th} sensor transfer function
\mathbf{h}_k	k^{th} source-to-sensor transfer function vector
f_{zk}	z component of the k^{th} source function
\hat{f}_{zkl}	estimate of k^{th} source function using l^{th} sensor signal and corresponding transfer function
Q	number of closely spaced omnidirectional point sources

CHAPTER 1

INTRODUCTION

1.1 General

Chest auscultation offers vast amounts of information that can assist in the diagnosis of various diseases of the heart and lungs [1], [2]. Specifically, a multi-sensor acoustic chest pad could be an extremely low-cost, powerful, light-weight and portable tool for accurate quantitative diagnosis of thoracic pathologies. Existing technologies like echocardiography are fairly expensive and are typically not available at all places, for instance, in out-patient home monitoring or battlefield situations.

Recent years have seen many studies that attempt to exploit the spatio-temporal distribution of thoracic sounds on the human torso for characterizing different pathologies in patients with heart or lung diseases. Most of these rely on pattern recognition techniques or array-signal processing algorithms or a combination of both. Although there has been some success in these efforts, not many of these studies have addressed the effects of heterogeneity of the medium on the performance of the algorithms [3], [4]. In addition, at lower audible range frequencies, the effects of shear waves in the signals measured cannot be ignored [5], [6]. The complexity of the problem increases further because of the extreme near-field conditions that prevail. The algorithms would thus seem to benefit if they incorporate a more accurate physics-based model, one that governs the sound propagation in the human thoracic cavity.

In order to have a better understanding of the transmission of sounds in the human thoracic cavity, this thesis attempts to numerically model the sound propagation using a finite-difference time-domain (FDTD) approach laying emphasis on the true geometry and material properties of the various tissues and organs in the human torso. The model thus allows one to study the effects of the heterogeneities on the acoustic sensor signals and can be used to validate all the existing signal processing algorithms used in previous studies. It also allows one to develop and validate newer signal processing and inverse problem solutions to localize the pathological sites in the thorax in a non-invasive manner. In addition, it can also be used as a tool to simulate different pathological conditions of the heart and lungs and allow one to study the associated sound distribution around the torso.

1.2 Dissertation layout

The layout of this dissertation is as follows:

Chapter 2 discusses some of the prior studies done in the fields of thorax acoustic modeling and signal processing used for diagnostic purposes. Chapter 3 provides details of the development of the viscoelastic FDTD model for sound propagation in the human thorax proposed in this work and discusses some of the modeling results obtained using the model. Chapter 4 employs the model developed to study the pneumothorax condition of the lung and provides some results that might be of diagnostic utility. Chapter 5 discusses some of the traditional source localization algorithms that are validated using the simulated signals obtained via the FDTD model and compares their performance to a transfer-function based algorithm developed using the forward model. Concluding remarks are provided in Chapter 6 that also discusses the future steps to be taken to address some of the unresolved issues.

CHAPTER 2

PRIOR WORK

2.1 Introduction

Studies related to understanding the origin, transmission, and characteristics of auscultation sounds in addition to its diagnostic utility have been going on for more than a few decades now. There have been various models proposed that attempt to simulate the sound wave propagation in the thorax, and a thorough survey of these works allow us to have a better understanding of the issues involved in pursuing this task. In addition to the modeling work, there are many studies in literature that have focused their efforts to developing signal processing algorithms either for source localization or for improved diagnostic ability.

2.2 Acoustic Modeling Studies of the Thorax

The earliest studies [7] – [9] lay emphasis on estimating the transfer function of the heart-thorax acoustic system and understanding the frequency response and attenuation characteristics of the heart sounds. These studies revealed that the heart sounds, in the low frequency range of 50 Hz to 400 Hz, are damped by both the viscosity and the geometrical spread in the medium, and attenuated by around 30 dB – 40 dB as they reached the chest surface. Phonocardiogram recordings indicated that almost 80% of the power of sounds recorded on the chest wall arose due to a linear transmission of sounds from the left ventricle. The remaining 20% are due to thoracic noise, noncoherent contributions from extraneous signals and from system nonlinearities.

Verburg's study [10] was one of the most significant works of the 1980s that attempted to model the heart sound propagation using visco-elastic wave equations, although in a homogeneous media. A dipole model of the heart sound source was proposed and the analytically simulated results of the model compared well with experimental observations in many aspects. The thoracic media was considered to be a linear viscoelastic body with complex material properties to account for the viscosity of the tissues. It was observed that both shear and compressional waves propagated. The study concluded that the lung tissue and the muscular connective tissue of the thoracic wall are the two primary tissues to be considered in the media for wave propagation modeling. These results formed the basis of all future thorax modeling efforts.

While efforts to understand the transmission of heart sounds continued, studies focused on lung sounds were beginning to gather more interest in the scientific and medical community. Wodicka *et al.* [11] – [15] developed an acoustic sound transmission

model from the respiratory tract to the chest wall via an equivalent acoustic circuit, wherein the circuit elements represented different transmission characteristics of the parenchyma and the chest wall. The resonance peaks of the transmission spectra could be estimated fairly well using these models. In addition, the models also estimated the frequency dependent propagation time (or phase delay) of sonic transmission from the trachea to the chest wall. However, all of these studies assume a very simple axisymmetric cylindrical geometry of the torso. Also, the tissue pathway to the chest is treated simply as a mass load on the parenchyma.

Vovk *et al.* [16] – [17] employed a similar axisymmetric cylindrical model to model the acoustic properties of the chest in order to study the transmission of breath sounds to the chest. His work however, did incorporate the tissue pathway to the chest as a layered structure of muscular rib cage, muscular fatty tissue and the skin. The study's elegance lay in the fact that for each layer, an appropriate set of differential equations of motion was analytically solved to characterize the behavior of that layer. Also, the effect of mechanical loading of the pick-up transducers on the measured surface sounds was carefully analyzed. It was observed that the presence of a transducer inevitably leads to the conversion of longitudinal wave into surface waves. This can pose significant challenges when multi-sensor signal processing techniques are employed for analysis. Vermarien too, in [18] had observed that the mechanical loading of the sensors on to the chest wall distorted the recordings of the sensor. Hence, the loading effect of the pick-up sensors should be taken into account in any experimental study.

In an effort to employ sound measurements to differentiate between normal and diseased lungs, Leung and Sehati [19], estimated the average speed of propagation of

sound from the trachea to various sites on the chest wall over a range of frequencies based on a cross-correlation function of the input and the measured sound. The speed estimates over a region of the thorax has been proposed to be used for diagnostic purposes.

A one dimensional model for the propagation of pressure waves through the lung using an equivalent mass spring chain model assuming a bi-periodic stack of tissue and air layers has been studied in [20]. The work revealed that while the lung does show dispersive behavior, i.e. signals of different frequencies travel at significantly different speeds, for sufficiently slow rising pressure waves, the lung could well be approximated using an equivalent homogeneous material in modeling studies.

The last few years have seen significant developments in the field of thorax modeling, in particular, the study of sound propagation through lungs. Royston *et al.* [5] have developed a 1D axisymmetric model similar to the work described in [16], accounting for both attenuation and viscous damping losses in the medium to study the effect of pneumothorax (PTX) on sound propagation from the bronchial airways to the skin surface. In addition, a finite element model simulating a non-axisymmetric 2D geometry was used to study the same problem. The complex 2D geometry resulted in increased non-radial scattering of sound than predicted by the 1D simple axisymmetric theory, thus resulting in increased attenuation.

Royston *et al.* in [21] points out that at low audible frequencies, compression and shear wave propagation from point sources can both be significant although the shear component becomes less significant relative to the compression wave component beyond a few hundred Hz. Royston *et al.* [22] extended their work in [5], [21] by modeling a lung

phantom and the true lung geometry (obtained from an X-ray CT image) using a boundary element formulation. Experimental results were compared with modeling estimates for the lung phantom. It was observed that the shear waves were prominent especially in the non-parenchymal soft tissue regions composed of fat, muscle and visceral material. Also, the acoustic response field created by an internal acoustic source was significantly different from that predicted by a free-field propagation model, thereby emphasizing the importance of incorporating realistic geometries for modeling. Further, the study also investigated the possibility of using acoustic sound measurements on the parenchymal surface to localize the lung sound source.

The finite difference time domain model developed by Narasimhan *et al.* [23] used the actual thoracic geometry of the thorax obtained from the Visible Human Project to model the sound propagation in the thorax. However, the model assumes a fluid medium throughout and ignores elastic wave contributions for the sake of simplicity. Key observations of this work are:

- Resonance effects of the thorax are significantly lesser at lower frequencies (~ 100 Hz) and are prominent at higher excitation frequencies (> 500 Hz). Also, frequencies of the order of 100 Hz are most effectively transmitted through the thorax.
- The size of the thorax has a profound effect on the transmission of breath sounds.
- The spectrum of the human thoracic recordings is far richer relative to the spectrum predicted by a homogeneous model simulation. This is probably due to the various anatomical features in the thorax.

- Chest wall sounds are affected by sound generated at the airways as well as the manner in which they are propagated in the thorax. Hence, accurate models for both sound generation and propagation are needed to simulate breath sounds.

Banks and Luke [24] employed the quasi-linear viscoelastic equation proposed by Fung [25] in a 2D ring-like geometry to study the propagation of shear waves in biotissue. The model can be used in developing a noninvasive method to diagnose coronary artery diseases caused by stenosis. The study justifies the use of a viscoelastic model as opposed to an elastic model for modeling shear wave propagation in biotissue.

All of the above discussed prior acoustic modeling studies, while, provide significant insight into the characteristics of sound propagation in the thorax, typically they either assume a simple geometry or ignore the shear wave contributions [12], [16], [22], [23]. The work proposed in this dissertation attempts to overcome these limitations by numerically modeling the viscoelastic sound propagation using a finite-difference time-domain (FDTD) approach laying emphasis on the true anatomical geometry and experimentally obtained estimates of viscoelastic material properties of the various tissues and organs in the human torso.

2.3 Signal Processing Methods for Acoustic Diagnostics

One of the earliest studies [26] on multi-sensor chest auscultation involved the simultaneous recording of precordial vibrations on 22 sites on the chest and displaying the peak amplitude spatial distribution as a function of time, which was used to analyze the radiation and propagation patterns of the thoracic sounds. However, as mentioned in [27], signal processing techniques that make use of the underlying physics, measurement dynamics and noise models would prove to be more useful in practice. Emphasis needs to be on model-based signal processing strategies that can provide more meaningful and useful results.

One such model based approach discussed in [3] uses the Multiple Signal Classification (MUSIC) algorithm for localization of acoustic sources in the heart by employing a near-field propagation model. The main drawbacks of this approach are that it assumes:

- a homogeneous medium of propagation
- there is no scattering or reflection of sound in the thoracic medium

The authors extend their work in [28] employing the same model, but use a Choi-Williams distribution to compute a spatial time-frequency matrix that provides important clues on the likely source locations in the heart.

Kompis *et al.* in [29], [30] and [31] employ a similar simplified model assuming homogeneous wave propagation and a constant damping factor in their least-squares estimation approach.

Owsley in [4], [32] uses multiple auscultation recordings for localizing the artery-blockage sites. A near-field focused beamformer is used to perform imaging of the spatial

shear wave energy field intensity. The beamformer model, as in [3] assumed a spherical wavefront impingement along with homogeneous propagation characteristics.

To summarize, all the existing signal processing strategies for source localization in the thorax [3], [4], [26] – [35] assume a constant propagation velocity in their models. Although some of the algorithms do provide marginally decent results, significant improvement would be necessary before any of these techniques could be employed for diagnostic purposes in a clinical environment. The viscoelastic forward model of sound propagation in the thorax proposed in this dissertation, being based on wave propagation physics specifically designed for human thorax, could thus potentially form the basis of alternate signal processing algorithms for source localization and source waveform estimation that might potentially yield better results as compared to traditional algorithms, eventually leading to clinical diagnostic solutions.

CHAPTER 3

VISCOELASTIC FDTD MODEL FOR HUMAN THORAX

3.1 Introduction

Auscultation sounds typically contain most of their energy at the lower audible range of frequencies. At these frequencies, it is observed that compression and shear wave propagation can both be significant in tissue like materials. In general as the frequency increases beyond a few hundreds of Hz, the shear wave component gradually becomes less important. However, unlike the case of ultrasonic imaging, at the lower range of frequencies, one cannot necessarily assume that compression waves dominate the response over the shear and surface waves. In addition, the acoustic paths are far more complex at sonic frequencies due to multiple reflections and standing wave patterns within the thoracic cavity. Thus, in order to develop a reasonably accurate sound propagation model in the human thorax, one is required to take into account both the bulk and shear modulus of elasticity and viscosity along with realistic estimates of the geometries of the various tissues and anatomical structures in the thorax.

3.2 Governing Equations

As mentioned in the previous section, there is sufficient evidence of the transmission of shear waves in addition to longitudinal waves in the human torso at the lower audible range frequencies. Hence, the governing equations of sound transmission in the torso requires to incorporate both these types of waves, and this is achieved through the

Elastodynamic equations, otherwise known as Elastic Wave equations. In addition, the viscosities of the tissues are to be accounted for into these equations by suitably modifying the coefficients or adding appropriate terms.

3.2.1 Elastodynamic Equations

These equations draw their roots from the Navier Stokes equation (force equation) and the Hooke's Law of elasticity [36], [37]. The Navier Stokes equation in its nonlinear form is as follows:

$$\rho \left[\frac{\partial \vec{v}}{\partial t} + (\vec{v} \cdot \nabla) \vec{v} \right] + \eta \vec{v} = \nabla \cdot \vec{T} + \vec{f} \quad (1)$$

Here ρ , η , \vec{v} , \vec{T} and \vec{f} denote the density, damping factor, velocity vector, stress tensor, and the force per unit volume vector, respectively. (Note: For fluid flow, equation (1) would include terms with shear and bulk viscosity. Also, tissues show visco-elastic properties. One of the ways to incorporate damping characteristic of the viscous medium into the above equations is through the damping factor η).

In 2D, the equations can be written as:

$$\begin{aligned} \rho \left[\frac{\partial v_x}{\partial t} + v_x \frac{\partial v_x}{\partial x} + v_z \frac{\partial v_x}{\partial z} \right] + \eta v_x &= \frac{\partial T_{xx}}{\partial x} + \frac{\partial T_{xz}}{\partial z} + f_x \\ \rho \left[\frac{\partial v_z}{\partial t} + v_x \frac{\partial v_z}{\partial x} + v_z \frac{\partial v_z}{\partial z} \right] + \eta v_z &= \frac{\partial T_{xz}}{\partial x} + \frac{\partial T_{zz}}{\partial z} + f_z \end{aligned} \quad (2)$$

The effect of the nonlinear term $(\vec{v} \cdot \nabla) \vec{v}$ was independently studied at the audible range of frequencies as a 1D problem. The study revealed that its effect was negligible and the

additional level of complexity introduced due to the nonlinearity may well be ignored for all practical purposes.

The Hooke's law provides the relationship between the stresses \vec{T} and strains S acting on an element through the constitutive parameters. In its simplest form, for an isotropic medium, the constitutive parameters that describe the medium completely are functions of the Lamé constants (λ, μ) .

$$\begin{aligned}\vec{T} &= c(\lambda, \mu) : S \\ \frac{\partial \vec{T}}{\partial t} &= c(\lambda, \mu) : \nabla \vec{v}\end{aligned}\tag{3}$$

Ignoring the nonlinear terms in equations (2) and combining the equations (2) and (3), we can write the elastic wave equations for a 2D problem in terms of the velocity and stress variables as:

$$\begin{aligned}\rho \frac{\partial v_x}{\partial t} + \eta v_x &= \frac{\partial T_{xx}}{\partial x} + \frac{\partial T_{xz}}{\partial z} + f_x \\ \rho \frac{\partial v_z}{\partial t} + \eta v_z &= \frac{\partial T_{xz}}{\partial x} + \frac{\partial T_{zz}}{\partial z} + f_z\end{aligned}\tag{4}$$

$$\begin{aligned}\frac{\partial T_{xx}}{\partial t} &= (\lambda + 2\mu) \frac{\partial v_x}{\partial x} + (\lambda) \frac{\partial v_z}{\partial z} \\ \frac{\partial T_{zz}}{\partial t} &= (\lambda) \frac{\partial v_x}{\partial x} + (\lambda + 2\mu) \frac{\partial v_z}{\partial z} \\ \frac{\partial T_{xz}}{\partial t} &= \mu \left(\frac{\partial v_x}{\partial z} + \frac{\partial v_z}{\partial x} \right)\end{aligned}\tag{5}$$

Equations in (4) are called the momentum equations, while equations in (5) are termed as the constitutive equations.

3.2.2 Popular Viscoelastic Models

Although the equations in (4) and (5) could be utilized for modeling the viscoelastic wave propagation, the parameters corresponding to the damping factor η aren't available for most tissues in the thorax. A standard linear viscoelastic, as opposed to the elastodynamic model, is thus more appropriate for this problem as it incorporates the viscous loss in the tissues in addition to their density and elasticity properties via parameters that are more widely available in literature [38]. The Voigt and Maxwell's models are two of the most commonly employed rheological models of viscoelasticity of tissues for numerical modeling purposes [25]. While the former is the more widely used, the latter is also used for certain tissue structures like bones [39].

Both these models use springs and dashpots to simulate the elastic and viscous components of the stress-strain (σ - ϵ) relation. The spring component, associated with the elasticity of the medium obeys the following relation:

$$\sigma = E\epsilon \tag{6}$$

where E corresponds to the elastic modulus of the medium. The dashpot component, associated with the viscosity of the medium $\tilde{\eta}$ is governed by:

$$\sigma = \tilde{\eta} \frac{\partial \epsilon}{\partial t} \tag{7}$$

The Maxwell model consists of a spring and dashpot in series. The governing stress-stress equation for this model thus becomes:

$$\frac{1}{E} \frac{\partial \sigma}{\partial t} + \frac{\sigma}{\tilde{\eta}} = \frac{\partial \varepsilon}{\partial t} \quad (8)$$

However, the Voigt model consists of the spring and dashpot in parallel, and the corresponding stress-strain equation thus becomes:

$$\sigma = E\varepsilon + \tilde{\eta} \frac{\partial \varepsilon}{\partial t} \quad (9)$$

Since most viscoelastic studies on tissues employ either one of these two models to incorporate the viscosity parameter, it would benefit to combine these two models into one framework that allows one to use parameters of either model. If we define $\tilde{\eta}_M$ and $\tilde{\eta}_V$ as the viscosity parameters associated with Maxwell and Voigt models respectively, then the governing equations can be written as:

$$\frac{\partial \sigma}{\partial t} + \frac{E}{\tilde{\eta}_M} \sigma = E \frac{\partial \varepsilon}{\partial t} + \tilde{\eta}_V \frac{\partial^2 \varepsilon}{\partial t^2} \quad (10)$$

3.2.3 Viscoelastic Wave Propagation Equation

In order to incorporate the viscosity parameters associated with either of the Maxwell and Voigt models into the governing equations, we employ the stress-strain relation as described in equation (10) together with the momentum equations in (4) and obtain the following equations that govern the wave propagation in a 2D viscoelastic medium:

$$\rho \frac{\partial v_x}{\partial t} = \frac{\partial T_{xx}}{\partial x} + \frac{\partial T_{xz}}{\partial z} + f_x \quad (11)$$

$$\rho \frac{\partial v_z}{\partial t} = \frac{\partial T_{xz}}{\partial x} + \frac{\partial T_{zz}}{\partial z} + f_z \quad (12)$$

$$\begin{aligned} \frac{\partial T_{xx}}{\partial t} + \gamma_{xx} T_{xx} &= (\lambda_1 + 2\mu_1) \frac{\partial v_x}{\partial x} + \lambda_1 \frac{\partial v_z}{\partial z} \\ &+ (\lambda_2 + 2\mu_2) \frac{\partial}{\partial t} \left(\frac{\partial v_x}{\partial x} \right) + \lambda_2 \frac{\partial}{\partial t} \left(\frac{\partial v_z}{\partial z} \right) \end{aligned} \quad (13)$$

$$\begin{aligned} \frac{\partial T_{zz}}{\partial t} + \gamma_{zz} T_{zz} &= \lambda_1 \frac{\partial v_x}{\partial x} + (\lambda_1 + 2\mu_1) \frac{\partial v_z}{\partial z} \\ &+ \lambda_2 \frac{\partial}{\partial t} \left(\frac{\partial v_x}{\partial x} \right) + (\lambda_2 + 2\mu_2) \frac{\partial}{\partial t} \left(\frac{\partial v_z}{\partial z} \right) \end{aligned} \quad (14)$$

$$\frac{\partial T_{xz}}{\partial t} + \gamma_{xz} T_{xz} = \mu_1 \left(\frac{\partial v_x}{\partial z} + \frac{\partial v_z}{\partial x} \right) + \mu_2 \frac{\partial}{\partial t} \left(\frac{\partial v_x}{\partial z} + \frac{\partial v_z}{\partial x} \right) \quad (15)$$

where v_l ($l = x, z$) are the particle velocities in the l direction, T_{ll} are the normal stress components and γ_{ll} are the corresponding resistance coefficients in the l direction, T_{xz} is the shear stress and γ_{xz} is the corresponding resistance coefficient in the x - z plane, f_l are the forcing functions in the l direction, ρ is the density and $\lambda = \lambda_1 + i\omega\lambda_2$, $\mu = \mu_1 + i\omega\mu_2$ are the complex Lamé constants of the medium. λ_1 and μ_1 define the stiffness of the

isotropic medium under consideration and are termed as coefficients of volume compressibility and shear elasticity, respectively. λ_2 and μ_2 define the viscosity of the medium as parameterized by the Voigt model and are termed as coefficients of volume viscosity and shear viscosity, respectively. ω is used to represent the angular frequency of the wave. The resistance coefficients of stress, originating from the Maxwell's model of viscosity, also control the viscous absorptive loss in the medium and are related to the attenuation coefficients of the tissues. Due to the heterogeneity of the medium, the density ρ , Lamé constants (λ and μ) and the resistance coefficients γ_{ij} are all functions of space governed by the viscoelastic properties of the various tissues in the thoracic cavity. Equations (11) and (12) are called the momentum equations, while equations (13) – (15) are termed as the constitutive equations.

3.3 Thorax Anatomy and Material Properties

In order to obtain an accurate structural representation of the various anatomical features of the thorax, a photographic image of the thoracic cavity of a 39 year old male human cadaver was acquired from the United States National Library of Medicine's Visible Human Project database [40], [41]. A transverse cross-sectional slice at the mid-thorax level passing through the heart, as shown in Figure 3-1, is chosen as the 2D image for the model study. The various anatomical features, inclusive of the organ and tissue boundaries are identified and the image is partitioned accordingly. Figure 3-2 shows this partitioned color-coded image where each color represents a distinct anatomical feature. The material properties corresponding to these features are assigned to the respective partitioned regions. The density, elasticity and viscosity parameters for each of these tissues are obtained from existing literature [5], [12], [42] – [55] and are listed in Table 3-1 to Table 3-4. Some of these properties are observed to have a wide range of values across different publications. In such cases, the most consistently reported value has been chosen in the present work.

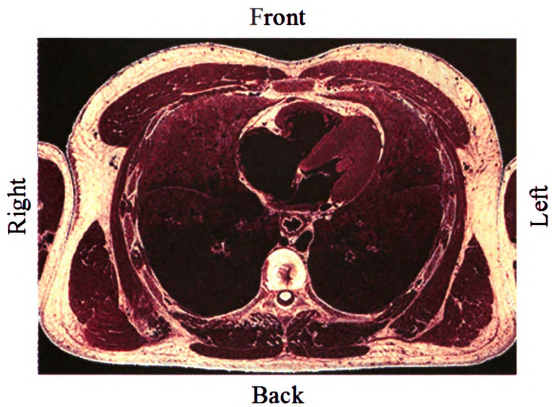


Figure 3-1 Photographic cross-sectional slice of the human thorax acquired from the Visible Human Project database [40], [41]



(a)

	Air – Background
	Ribs
	Fashia – Subcutaneous Fatty Tissue
	Serratus Anterior Muscle
	Left Atrium
	Erector Spinae Muscle, Trapezius Muscle
	Pericardium
	Right Atrium
	Left Ventricle
	Esophagus
	Scapula Bone
	Intervertebral Disc
	Azygous Vein
	Skin
	Latissimus Dorsi Muscle
	Lungs
	Spinal Cord
	Pectoralis Major
	Right Ventricle
	Aorta

(b)

Figure 3-2 (a) Cross-sectional slice of human thorax partitioned into distinct anatomical regions, each tissue color-coded with a unique color (b) Corresponding color-code key to identify the different tissues

Table 3-1 Material properties (density, volume compressibility, shear elasticity, volume viscosity, shear viscosity) and longitudinal wave velocity c_p of the tissues that use the Voigt model of viscoelasticity in the thoracic cavity.

Material	ρ^a (kg/m ³)	λ_1 (Pa)	μ_1 (Pa)	μ_2 (Pa-s)	c_p^a (m/s)
Fashia	985	2.114G	5k ^b	4 ^c	1465
Chest Muscles ^d	1050	2.621G ^e	8.68k ^e	9.73 ^e	1580
Heart	1060	2.633G	124k ^f	15.9m ^f	1576
Blood	1060	2.660G	0	3.2m ^g	1584
Skin / Dermis	1090	2.839G	2M ^h	0.131 ^f	1615
Lungs	250 ⁱ	124.3k	4k ^j	20.02 ^k	23 ⁱ

$\lambda_2 = 0$ Pa-s [48]

^a ρ and c_p are obtained from Reference 46 unless explicitly mentioned

^b Reference 47

^c Reference 48

^d Includes Serratus Anterior, Erector Spinae, Trapezius, Latissimus Dorsi and Pectoralis Major Muscles

^e Reference 49

^f Reference 50

^g Reference 52

^h Reference 53

ⁱ Reference 12

^j Reference 54. Shear wave velocity of 4 m/s is used to calculate the shear elasticity.

^k Reference 5

Table 3-2 Material properties (density, volume compressibility, volume viscosity, shear elasticity, shear viscosity) of air surrounding the thoracic cavity.

Material	ρ (kg/m ³)	λ_1 (Pa)	λ_2 (Pa-s)
Air ^a	1.24	147k	0.13

$$\mu_1 = \mu_2 = 0 \text{ Pa-s [42]}$$

^aReference 42

Table 3-3 Material properties (density, volume compressibility, shear elasticity, volume viscosity, shear viscosity), longitudinal wave velocity c_p and Young's modulus E of the spinal cord and intervertebral disc in the thoracic cavity.

Material	ρ (kg/m ³)	λ_1 (Pa)	μ_1 (Pa)	c_p (m/s)	E (Pa)
Spinal Cord	1038 ^a	2.467G	466.7k	1542 ^a	1.4M ^b
Intervertebral Disc	1000 ^c	16.4M	335.6k	-	1M ^c

$$\lambda_2 = 0 \text{ Pa-s [48]}$$

$$\mu_2 = 4 \text{ Pa-s [48]}$$

^aReference 46

^bReference 55

^cReference 51 – Poisson ratio of 0.49 is also provided in this reference.

Table 3-4 Material properties (density, volume compressibility, shear elasticity, resistance coefficient to normal and shear stresses), longitudinal wave velocity c_p and Young's modulus E of the ribs and scapula bone that use the Maxwell model of viscoelasticity in the thoracic cavity.

Material	ρ (kg/m ³)	λ_1 (Pa)	μ_1 (Pa)	c_p^d (m/s)	E (Pa)
Ribs, Scapula	1990 ^a	14.81G	5.063G	3540 ^a	13.9G ^b

$$\gamma_{xx} = \gamma_{zz} = 1.57k \text{ 1/s [45]}$$

$$\gamma_{xz} = 10.1k \text{ 1/s [45]}$$

^aReference 43

^bReference 44

3.4 Boundary Conditions

The boundary conditions play a key role any numerical modeling scheme. In the present application of viscoelastic wave transmission in the human thorax, boundary conditions need to be imposed at the chest-air interface. There are numerous ways to incorporate appropriate boundary conditions at this interface. The most common approach involves imposing a stress-free condition on the torso surface. However, for a finite-difference approach using a rectangular grid, imposing a stress-free condition on a complex torso boundary often becomes challenging. Instead, we propose to use a perfectly matched layer (PML) of air surrounding a thin layer of air around the torso, which can be incorporated into the finite-difference framework seamlessly.

3.4.1 Concept of PML

The basic idea of PML is to create an additional layer of a reflection-less absorbing material around the geometry function that absorbs the waves in this region. This is achieved through the use of complex stretching coordinates for the spatial variables. To see how this works, let us consider a plane wave solution in a one dimensional x coordinate space given by $e^{-i\omega t} e^{ikx}$ where ω and k represent the angular frequency and wave-number, respectively. This represents a non-attenuating plane wave. If the space variable x is replaced by a complex stretched version of it, say $\tilde{x} = \varepsilon_x x = \left(1 + i \frac{w_x}{\omega}\right) x$, then the plane wave solution modifies to $e^{-i\omega t} e^{ikx} e^{-kw_x x / \omega}$. The third term $e^{-kw_x x / \omega}$ in this solution represents a loss factor that attenuates the wave with

increasing distance. Thus, by choosing a non-zero w_x in the PML layer and setting the remaining areas to have $w_x = 0$, we can simulate an absorbing material at the exterior. It has been shown that an optimum choice of the stretching factors ε_x can yield the desired reflection-less property of the PML region [56].

Most PML formulations employing this coordinate stretching concept however, require an artificial splitting of velocity and stress variables in the FDTD implementation that decreases the computational efficiency of the codes. In order to avoid the computational burden caused due to splitting, a non-split PML based on recursive integration has been employed in the current work [57].

3.4.2 Recursive Integration PML

In the frequency domain, the 2D stretching functions ε_l ($l = x, z$) used in the PML can be written as:

$$\varepsilon_l = a_l + \frac{iw_l}{\omega} \tag{16}$$

where the real part a_l is the scaling factor and the imaginary part w_l corresponds to the loss in the PML region. ω represents the angular frequency. Correspondingly, the spatial derivatives in the stretched-coordinate PML space are given by:

$$\frac{\partial}{\partial \tilde{l}} \Rightarrow \frac{1}{\varepsilon_l} \frac{\partial}{\partial l} \quad (l = x, z) \tag{17}$$

The tilde here indicates that the spatial derivative is taken in the frequency domain. The recursive integration PML technique employs two auxiliary tensors, the stress-rate tensor \mathbf{S} and the strain-rate tensor \mathbf{E} through which the non-split set of equations are obtained. These tensors are defined as follows:

$$\tilde{S}_{ij} = \frac{1}{\varepsilon_j} \frac{\partial \tilde{T}_{ij}}{\partial j} \quad (i, j = x, z) \quad (18)$$

$$\tilde{E}_{ij} = \frac{1}{\varepsilon_j} \frac{\partial \tilde{v}_i}{\partial j} \quad (i, j = x, z) \quad (19)$$

where the tilde corresponds to the frequency domain counterparts of the corresponding variables. By introducing these tensor definitions and using equations (16) – (19) into the frequency domain counterparts of equations (11) and (13), we get the following equations:

$$i\omega\rho\tilde{v}_x = \tilde{S}_{xx} + \tilde{S}_{xz} + \tilde{f}_x \quad (20)$$

$$i\omega\tilde{T}_{xx} + \gamma_{xx}\tilde{T}_{xx} = (\lambda_1 + 2\mu_1)\tilde{E}_{xx} + \lambda_1\tilde{E}_{zz} + i\omega(\lambda_2 + 2\mu_2)\tilde{E}_{xx} + i\omega\lambda_2\tilde{E}_{zz} \quad (21)$$

Transforming these back into time-domain, and following the same procedure for all the equations in (11) – (15), we obtain the following velocity-stress equations:

$$\rho \frac{\partial v_x}{\partial t} = S_{xx} + S_{xz} + f_x \quad (22)$$

$$\rho \frac{\partial v_z}{\partial t} = S_{zx} + S_{zz} + f_z \quad (23)$$

$$\begin{aligned} \frac{\partial T_{xx}}{\partial t} + \gamma_{xx} T_{xx} &= (\lambda_1 + 2\mu_1) E_{xx} + \lambda_1 E_{zz} \\ &+ (\lambda_2 + 2\mu_2) \frac{\partial E_{xx}}{\partial t} + \lambda_2 \frac{\partial E_{zz}}{\partial t} \end{aligned} \quad (24)$$

$$\begin{aligned} \frac{\partial T_{zz}}{\partial t} + \gamma_{zz} T_{zz} &= \lambda_1 E_{xx} + (\lambda_1 + 2\mu_1) E_{zz} \\ &+ \lambda_2 \frac{\partial E_{xx}}{\partial t} + (\lambda_2 + 2\mu_2) \frac{\partial E_{zz}}{\partial t} \end{aligned} \quad (25)$$

$$\frac{\partial T_{xz}}{\partial t} + \gamma_{xz} T_{xz} = \mu_1 (E_{xz} + E_{zx}) + \mu_2 \left(\frac{\partial E_{xz}}{\partial t} + \frac{\partial E_{zx}}{\partial t} \right) \quad (26)$$

The auxiliary tensor components here are obtained by substituting the definition of the complex stretching function equation (16) into equations (18) – (19) and transforming them into time-domain. The following equations result after some rearrangement:

$$w_j \int_{-\infty}^t S_{ij}(\tau) d\tau = \frac{\partial T_{ij}}{\partial j} - a_j S_{ij} \quad (i, j = x, z) \quad (27)$$

$$w_j \int_{-\infty}^t E_{ij}(\tau) d\tau = \frac{\partial v_i}{\partial j} - a_j E_{ij} \quad (i, j = x, z) \quad (28)$$

The recursive property of the integrals become apparent following the discretization of the above equations and is presented in section (3.6.1).

Equations (22) – (26) and (27) – (28) thus effectively incorporate the PML boundary into the original viscoelastic equations. The values of α_l and w_l in the entire domain decide the PML and non-PML regions. A value of $\alpha_l = 1$ and $w_l = 0$ is chosen in the computational non-PML region, and a positive w_l in the PML region to introduce the loss. The reflection-less property of the PML is theoretically achieved only in a continuous spatial coordinate system. While employed in a FDTD scheme, where the domain is discretized, zero reflection cannot be practically achieved. In order to reduce the numerical reflections in the PML region, the loss factor w_l in this region is usually chosen to have a tapered profile as follows:

$$w_l(u) = \frac{3c_p}{2d} \log\left(\frac{1}{R}\right) \left(\frac{u}{d}\right)^m \quad (0 \leq u \leq d) \quad (29)$$

where $u = 0$ corresponds to the location of the interface of the computational domain and the PML region, d represents the thickness of the PML, m is the scaling order, R is the theoretical reflection coefficient and c_p is the longitudinal wave velocity in the PML region [56], [58], [59]. The amount of reflection can be controlled by choosing an optimal R value. In the application presented in this paper, R and m were chosen to be 0.001 and 1 respectively [58].

3.5 Source Model and Initial Conditions

Sound generation in the thorax is an extremely complex phenomenon involving various sources each of which is governed by different mechanisms. For instance, the sounds originating at the heart alone are composed of the opening and closing beats of the four valves, the vibrations of the ventricular and vascular walls and the ones caused due to blood flow haemodynamics. Similarly, modeling the respiratory breath sounds is equally or more challenging as it involves complex air flow dynamics in the trachea and bronchial airways. In the current work, since the primary focus has been on sound propagation rather than generation, the sound source model employed is a simple point source placed at the mitral valve location, say at (x_0, z_0) . A first derivative of a Gaussian pulse, centered at frequency f_0 is used as the z component of the forcing function f_z while the x component of the forcing function f_x is set to zero.

$$\begin{aligned}
 f_z(x, z, t) &= B(t-t_0) \left[\frac{1}{\sqrt{2\pi}\sigma} e^{-\frac{(t-t_0)^2}{2\sigma^2}} \right] \delta(x-x_0)\delta(z-z_0) \quad \forall t \geq 0 \\
 &= 0, \quad \forall t < 0 \\
 f_x(x, z, t) &= 0, \quad \forall t
 \end{aligned}
 \tag{30}$$

where the standard deviation σ and amplitude B are defined such that the peak magnitude at the center frequency f_0 in the Fourier domain is kept constant. The forcing function f_z in the frequency domain is given by:

$$\tilde{f}_z(x, z, \omega) = B\sigma^2 \omega e^{-\frac{\sigma^2 \omega^2}{2}} e^{-j\left(\omega t_0 + \frac{\pi}{2}\right)} \delta(x - x_0) \delta(z - z_0) \quad (31)$$

Thus, by defining the standard deviation σ and amplitude B as follows,

$$\sigma = \frac{1}{\omega_0} = \frac{1}{2\pi f_0} \quad (32)$$

$$B = \frac{Ae^{0.5}}{\sigma} \quad (33)$$

a peak magnitude of A is established at the center frequency f_0 , regardless of the frequency f_0 . The time-shift t_0 is heuristically chosen to be 5 times the standard deviation σ to provide a causal signal so that forcing function approaches to zero at $t = 0$.

Alternatively, instead of a point source, an explosive source may be modeled to simulate a distributed source as follows:

$$\begin{aligned} \tilde{f}(r, t) &= f(t)\tilde{g}(r) \\ f(t) &= B(t - t_0) \left[\frac{1}{\sqrt{2\pi\sigma}} e^{-\frac{(t-t_0)^2}{2\sigma^2}} \right] \delta(x - x_0) \delta(z - z_0) \quad \forall t \geq 0 \\ &= 0, \quad \forall t < 0 \\ \tilde{g}(r) &= \left(1 - \frac{r^2}{a^2}\right)^3 1_{B(a)}\left(\frac{x - x_0}{r}, \frac{z - z_0}{r}\right) \\ r &= \sqrt{(x - x_0)^2 + (z - z_0)^2} \end{aligned} \quad (34)$$

where $1_{B(a)}$ is a unity disc with center (x_0, z_0) and radius a .

The initial conditions for the problem define the velocity and stress variables at time $t = 0$. Since the forcing function as defined in equation (30) is zero for time $t < 0$, we assume that the medium is in equilibrium at time $t = 0$, i.e. all the velocity and stress variables are set to zero at $t = 0$ everywhere in the medium. Consequently, all the components of the auxiliary tensors are also set to zero at $t = 0$.

3.6 Finite-Difference Time-Domain Implementation

There are a slew of finite-difference time-domain (FDTD) schemes available in literature. However, the most commonly employed technique for elastodynamic wave propagation problems is the center differencing scheme with a staggered grid that results in a leapfrog system of equations for the velocity and stress variables [60]. This provides a second order accurate solution to the problem. In order to guarantee stability of the FDTD codes, care must be taken in choosing the smallest time-step while handling the discontinuities of material properties at the interface boundaries.

3.6.1 Discretization scheme

A staggered grid leap-frog center-differencing scheme [61] was used to discretize the momentum and constitutive relation equations described in (22) – (26). For this 2D velocity-stress formulation of the viscoelastic equations, the velocity and stress variables are used in a staggered grid as shown in Figure 3-3. In the discretized equations to follow, the indices i, j and k correspond to the discretization of the spatial variables x, z and the time variable t , respectively. Δx and Δz are the grid steps for the x -axis and z -axis respectively. Δt is the grid step in time. Due to the leapfrog scheme employed, the velocity variables and the stress variables are computed at times separated by half a time-

step $\frac{\Delta t}{2}$.

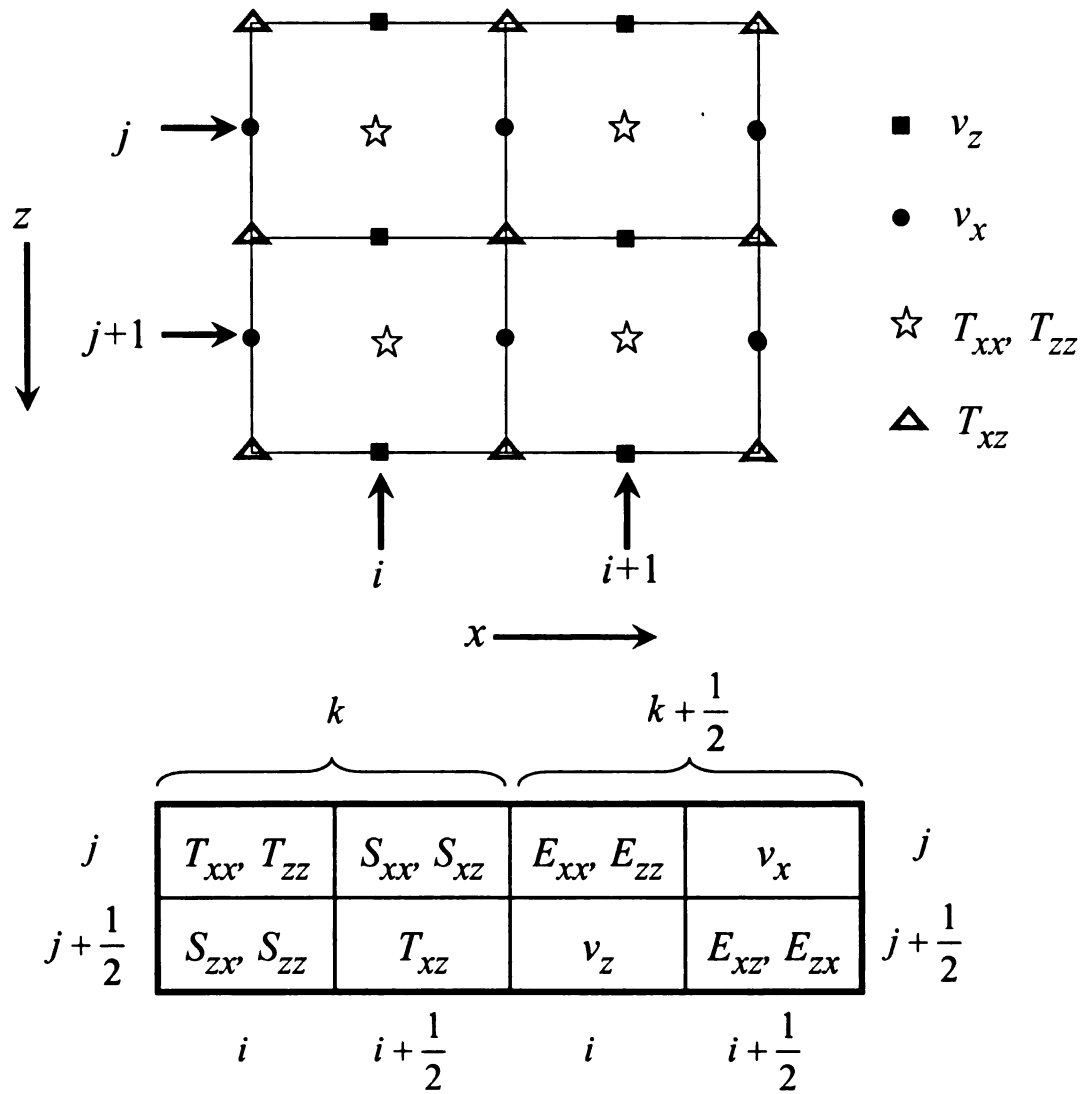


Figure 3-3 Staggered grid layout for the 2D velocity-stress FDTD scheme indicating the relative spatial and time indices at which the variables are computed

Using the center differencing scheme for each of the temporal and spatial derivatives in equations (22) – (26), we get a sequence that constitutes the leapfrog system of equations. Discretized forms of equations (22) and (24) are shown below:

$$\begin{aligned}
v_x\left(i+\frac{1}{2},j,k+\frac{1}{2}\right) &= v_x\left(i+\frac{1}{2},j,k-\frac{1}{2}\right) \\
&+ \frac{\Delta t}{\rho} \left[\begin{aligned} &S_{xx}\left(i+\frac{1}{2},j,k\right) + S_{xz}\left(i+\frac{1}{2},j,k\right) \\ &+ f_x\left(i+\frac{1}{2},j,k\right) \end{aligned} \right]
\end{aligned}
\tag{35}$$

$$\begin{aligned}
T_{xx}(i,j,k+1) &= \frac{\left(\frac{1}{\Delta t} - \frac{\gamma_{xx}}{2}\right)}{\left(\frac{1}{\Delta t} + \frac{\gamma_{xx}}{2}\right)} T_{xx}(i,j,k) \\
&+ \frac{1}{\left(\frac{1}{\Delta t} + \frac{\gamma_{xx}}{2}\right)} \left[\begin{aligned} &(\lambda_1 + 2\mu_1)E_{xx}\left(i,j,k+\frac{1}{2}\right) \\ &+ \lambda_1 E_{zz}\left(i,j,k+\frac{1}{2}\right) \end{aligned} \right] \\
&+ \frac{(\lambda_2 + 2\mu_2)}{\left(\frac{1}{\Delta t} + \frac{\gamma_{xx}}{2}\right)} \frac{1}{2\Delta t} \left[\begin{aligned} &3E_{xx}\left(i,j,k+\frac{1}{2}\right) - 4E_{xx}\left(i,j,k-\frac{1}{2}\right) \\ &+ E_{xx}\left(i,j,k-\frac{3}{2}\right) \end{aligned} \right] \\
&+ \frac{\lambda_2}{\left(\frac{1}{\Delta t} + \frac{\gamma_{xx}}{2}\right)} \frac{1}{2\Delta t} \left[\begin{aligned} &3E_{zz}\left(i,j,k+\frac{1}{2}\right) - 4E_{zz}\left(i,j,k-\frac{1}{2}\right) \\ &+ E_{zz}\left(i,j,k-\frac{3}{2}\right) \end{aligned} \right]
\end{aligned}
\tag{36}$$

Note that the second terms on the left hand side of equations (24) – (26), i.e. the Maxwell’s viscosity terms involving the stress variables are discretized by taking an average of their values at $t = k\Delta t$ and $t = (k+1)\Delta t$ as the stress terms are not evaluated at $(k+1/2)\Delta t$. This averaging has the same second-order accuracy as the other terms involving the center differencing, and thus does not degrade the overall accuracy. Similarly, time derivatives of the strain-rate tensor components, i.e. the Voigt’s viscosity

terms in equations (24) – (26) are discretized using a three-point stencil to provide second-order accuracy.

The integral of the auxiliary tensors in equations (27) – (28) are discretized using a trapezoid rule and appear as follows for the S_{xx} and E_{xx} components.

$$\left(a_x + \frac{w_x \Delta t}{2}\right) S_{xx}\left(i + \frac{1}{2}, j, k\right) = \left[\frac{T_{xx}(i+1, j, k) - T_{xx}(i, j, k)}{\Delta x} \right] - \Delta t \left[\frac{w_x}{2} S_{xx}\left(i + \frac{1}{2}, j, 0\right) + w_x \sum_{m=1}^{k-1} S_{xx}\left(i + \frac{1}{2}, j, m\right) \right] \quad (37)$$

$$\left(a_x + \frac{w_x \Delta t}{2}\right) E_{xx}\left(i, j, k + \frac{1}{2}\right) = \frac{1}{\Delta x} \left[v_x\left(i + \frac{1}{2}, j, k + \frac{1}{2}\right) - v_x\left(i - \frac{1}{2}, j, k + \frac{1}{2}\right) \right] - \Delta t \left[\frac{w_x}{2} E_{xx}\left(i, j, \frac{1}{2}\right) + w_x \sum_{m=1}^{k-1} E_{xx}\left(i, j, m + \frac{1}{2}\right) \right] \quad (38)$$

By imposing the initial conditions on the stress-rate and strain-rate components, and by defining the stress-rate sums and strain-rate sums as follows,

$$\begin{aligned} \Omega_{xx}\left(i + \frac{1}{2}, j, k - 1\right) &= w_x \sum_{m=1}^{k-1} S_{xx}\left(i + \frac{1}{2}, j, m\right) \\ &= \Omega_{xx}\left(i + \frac{1}{2}, j, k - 2\right) + w_x S_{xx}\left(i + \frac{1}{2}, j, k - 1\right) \end{aligned} \quad (39)$$

$$\begin{aligned}
\Psi_{xx}\left(i, j, m + \frac{1}{2}\right) &= w_x \sum_{m=1}^{k-1} E_{xx}\left(i, j, m + \frac{1}{2}\right) \\
&= \Psi_{xx}\left(i, j, m - \frac{1}{2}\right) + w_x E_{xx}\left(i, j, k - \frac{1}{2}\right)
\end{aligned}
\tag{40}$$

we can rewrite equations (37) – (38) as

$$\begin{aligned}
\left(a_x + \frac{w_x \Delta t}{2}\right) S_{xx}\left(i + \frac{1}{2}, j, k\right) &= \frac{T_{xx}(i+1, j, k) - T_{xx}(i, j, k)}{\Delta x} \\
&\quad - \Delta t \Omega_{xx}\left(i + \frac{1}{2}, j, k - 1\right) \\
\Omega_{xx}\left(i + \frac{1}{2}, j, k\right) &= \Omega_{xx}\left(i + \frac{1}{2}, j, k - 1\right) + w_x S_{xx}\left(i + \frac{1}{2}, j, k\right)
\end{aligned}
\tag{41}$$

$$\begin{aligned}
\left(a_x + \frac{w_x \Delta t}{2}\right) E_{xx}\left(i, j, k + \frac{1}{2}\right) &= \frac{1}{\Delta x} \left[\begin{aligned} &v_x\left(i + \frac{1}{2}, j, k + \frac{1}{2}\right) \\ &-v_x\left(i - \frac{1}{2}, j, k + \frac{1}{2}\right) \end{aligned} \right] \\
&\quad - \Delta t \Psi_{xx}\left(i, j, m + \frac{1}{2}\right) \\
\Psi_{xx}\left(i, j, m + \frac{3}{2}\right) &= \Psi_{xx}\left(i, j, m + \frac{1}{2}\right) + w_x E_{xx}\left(i, j, k + \frac{1}{2}\right)
\end{aligned}
\tag{42}$$

Equations (41) – (42) provide a convenient way to recursively compute the integrals involved in the update equations of S_{xx} and E_{xx} . All the remaining components of the auxiliary tensors are discretized and updated in a similar fashion. The above equations thus provide a time-stepping system to track the propagation of viscoelastic waves throughout the medium initiated by the forcing function.

3.6.2 Numerical Stability

For the above described explicit 2D FDTD scheme, one of the stability criteria is provided by the Courant-Levy condition that imposes a limit on the smallest time-step allowed. According to the Courant condition,

$$c_p \Delta t \sqrt{\frac{1}{(\Delta x)^2} + \frac{1}{(\Delta z)^2}} \leq 1 \quad (43)$$

must be satisfied everywhere in the medium. Thus, if $\Delta x = \Delta z$ and $c_{p,max}$ is the maximum longitudinal wave velocity in the medium, then the Courant numerical stability condition reduces to

$$\Delta t \leq \frac{1}{\sqrt{2}} \frac{\Delta x}{c_{p,max}} \quad (44)$$

Equation (44) is thus used to decide on the time-step for the FDTD scheme.

However, the Courant limit on the smallest time-step need not be sufficient to guarantee stability in a heterogeneous medium. Schroder [62] shows that the smallest time-step required for a stable solution in elastodynamic wave propagation problems can be more restrictive than the Courant condition as defined in equation (44) depending on the Lamé constants and densities of the materials at the interface regions in the medium. To ensure that equation (44) is sufficient for stability in any medium, the material properties are averaged at the interface regions, especially at boundaries where the properties differ significantly. While the material densities are averaged linearly in x and

z directions for the momentum equations, the inverse of the shear elasticity μ_I of each of the four adjoining cells is averaged for use in the constitutive equations.

3.7 Numerical Results

The leapfrog system of FDTD equations developed in section (3.6.1) is implemented in Matlab. The codes are validated on a simplified geometry before using them for simulating the sound propagation in the thorax from a source placed at the location of the mitral valve in the heart. Source to receiver transfer functions are computed and analyzed to provide some perspective on how the results may be used for diagnostic purpose.

3.7.1 Validation of FDTD codes

In order to validate the FDTD simulation codes, the numerical results obtained are compared to analytical expressions derived for a simplified case. We consider a homogeneous, infinitely extending, isotropic, and elastic medium with a density of 1000 kg/m^3 , and longitudinal and shear velocities of 1500 m/s and 500 m/s with a point force source acting at the origin. Two types of forcing functions are considered and the comparison results with both of these shall be presented here. In addition to comparison with analytical solutions, the FDTD results, particularly in terms of the effectiveness of its PML layers, are compared with those presented by Collino *et al.* in [58].

3.7.1.1 Comparison with analytical solution

The two f_z forcing functions used to compare the FDTD results with analytical solutions are:

- First derivative of a Gaussian pulse
- Sinusoidal pulse

In both cases, the f_x component of the forcing function is set to zero. The velocity and stress components are calculated at an array of 21 receiver locations at $z = 0.8$ m, $x = [-1, -0.9, -0.8, \dots, -0.1, 0, 0.1, \dots, 0.9, 1]$ m in the x - z coordinate system as shown in Figure 3-4.

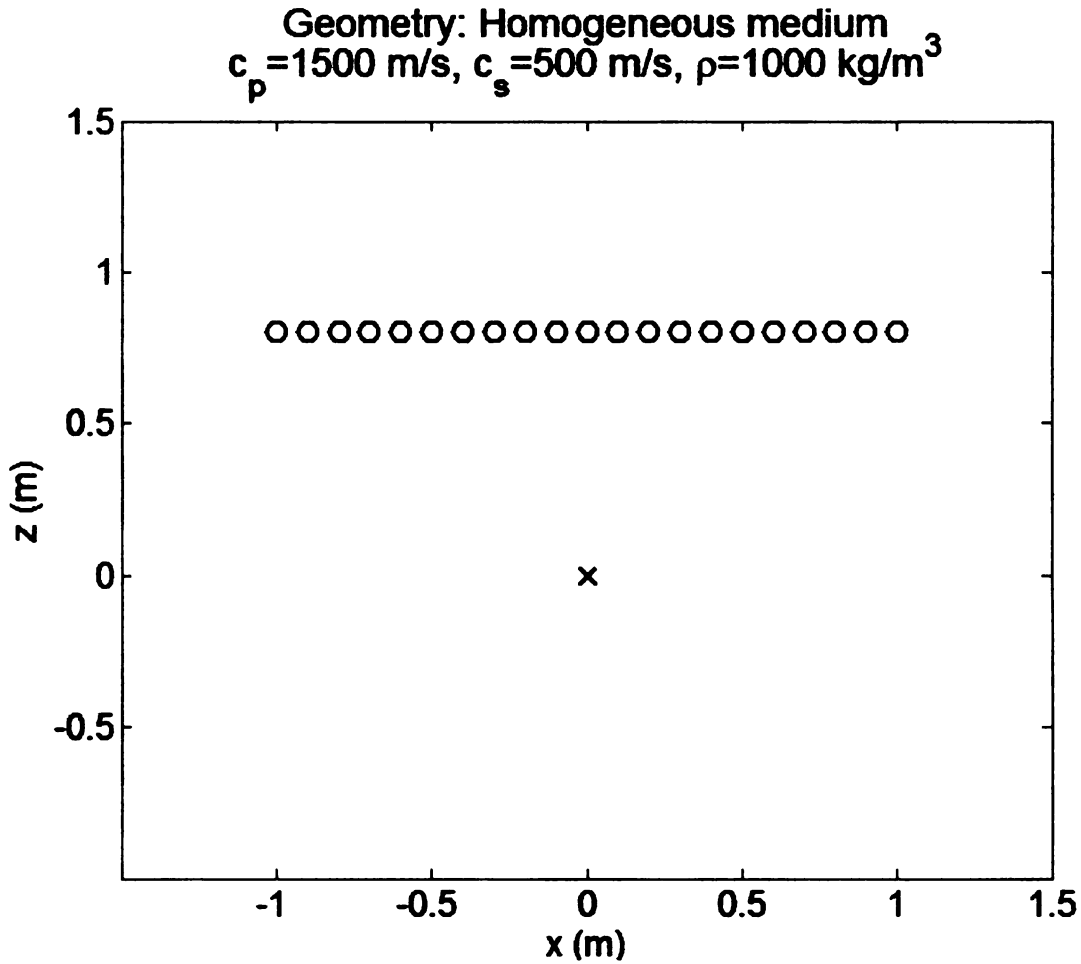


Figure 3-4 Geometry of the problem for validating the FDTD code. Black circles represent the array of receiver locations. Black cross represents the source location.

The 2D FDTD program discretized the domain into 120 X 120 cells with a PML width of 18 cells on each side of the domain. A cell size of 16.66 mm X 16.66 mm and a

time-step of $\Delta t = 1 \mu\text{s}$ is used in the simulation. The displacement solutions for the elastic wave equations for an impulsive point force as derived by Eaton *et al.* are used to obtain analytical results for the applied forcing functions, which are then compared with the FDTD simulation results [63]. Figure 3-5(a) shows a first derivative of a Gaussian pulse with a center frequency of 1 kHz that is used as the f_z component of the forcing function for the first case while Figure 3-5(b) shows the 1 kHz sinusoidal pulse f_z forcing function used in the second case. The velocity components v_x and v_z obtained using the FDTD simulations for the two forcing functions are compared as images in Figure 3-6 and Figure 3-7 [64]. Figure 3-6 compares the results obtained for the Gaussian first derivative forcing pulse while Figure 3-7 compares those for the sinusoidal forcing pulse.

Figure 3-8 compares the normalized v_z component obtained using the analytical expression and the FDTD simulation for the 1 kHz Gaussian first derivative forcing pulse at 11 of the receiver locations, corresponding to $x = [-1, -0.8, -0.6, -0.4, -0.2, 0, 0.2, 0.4, 0.6, 0.8, 1]$ m, by overlapping the 1D signal waveforms obtained in both cases in the same plot. We observe excellent agreement between the numerical and analytical results. The largest normalized mean squared error (NMSE) across all sensors was 2.5% and the mean NMSE was 1.55%. Further, we also notice that the PML is effective in absorbing the outgoing waves as no reflections are observable in Figure 3-8 [58].

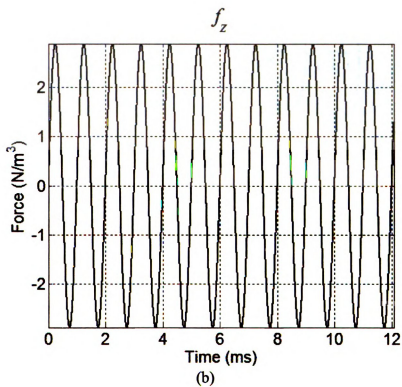
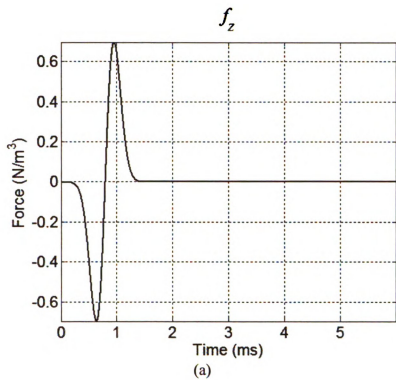


Figure 3-5 f_z components of the forcing functions (a) Gaussian first derivative forcing pulse (b) Sinusoidal forcing pulse

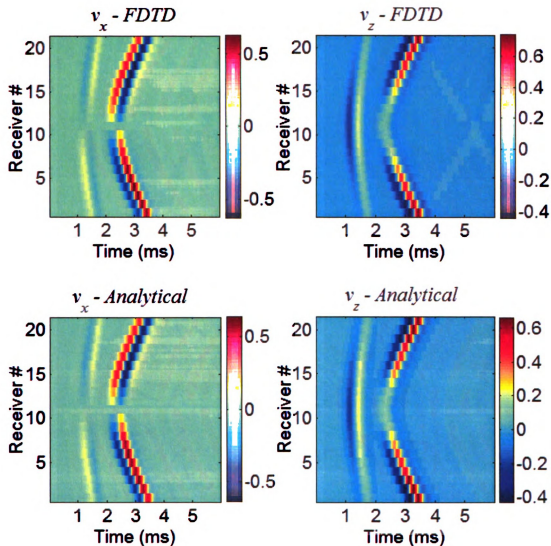


Figure 3-6 Comparison of v_x and v_z components obtained via FDTD to their corresponding analytical counterparts for the 1 kHz Gaussian first derivative forcing pulse (all color-bar units are in m/s)

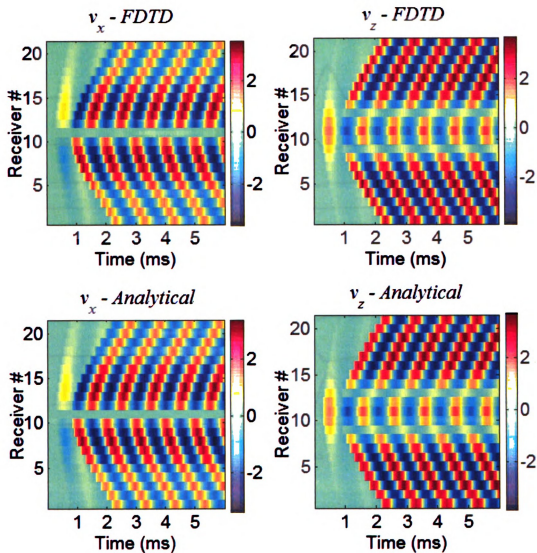


Figure 3-7 Comparison of v_x and v_z components obtained via FDTD to their corresponding analytical counterparts for the 1 kHz sinusoidal forcing pulse (all color-bar units are in m/s)

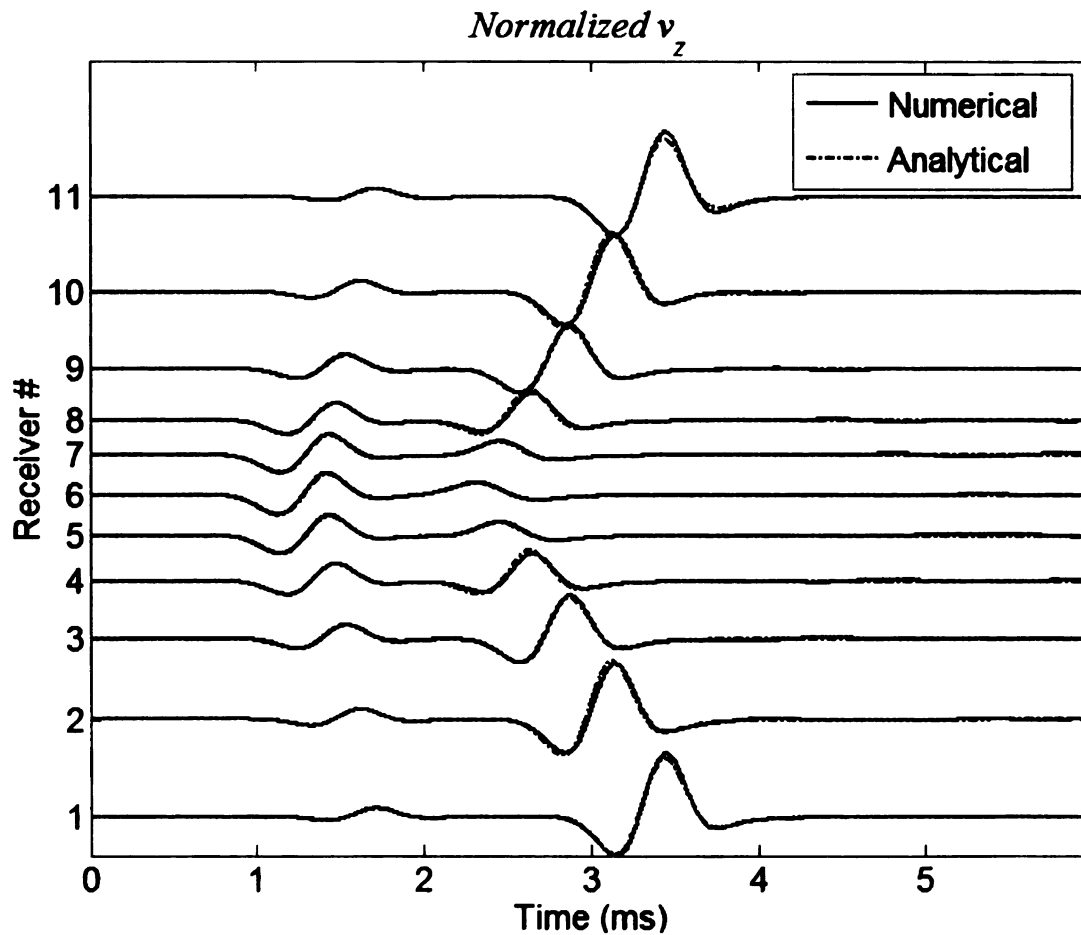


Figure 3-8 Comparison of numerical FDTD with analytical results for a 1 kHz Gaussian first-derivative point forcing f_z source located at origin in a 2D homogeneous medium ($\rho = 1000 \text{ kg/m}^3$, $c_p = 1500 \text{ m/sec}$, $c_s = 500 \text{ m/sec}$) – Normalized v_z component of velocity at 11 receiver locations located at $z = 0.8 \text{ m}$ and $x = (-1 \text{ m to } 1 \text{ m, in steps of } 0.2 \text{ m})$

3.7.1.2 Comparison with results published in literature

Francis Collino *et al.* presented some results on the application of PML to linear elastodynamic problems in [58]. The propagation of elastic waves in a homogeneous elastic medium due to an explosive source at the left top corner is shown as a series of time snapshots of the absolute velocity over the entire domain in Figure 3-9 and Figure 3-

10; the former one being the result published in [58] and the latter one, obtained here using the previously described FDTD code.

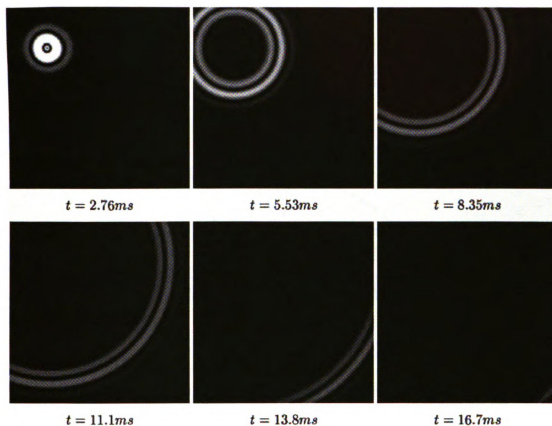


Figure 3-9 Elastic wave propagation results as presented by Collino *et al.* [58] – Snapshots of absolute velocity over the entire homogeneous domain caused due to an explosive source located at the top left corner of the domain

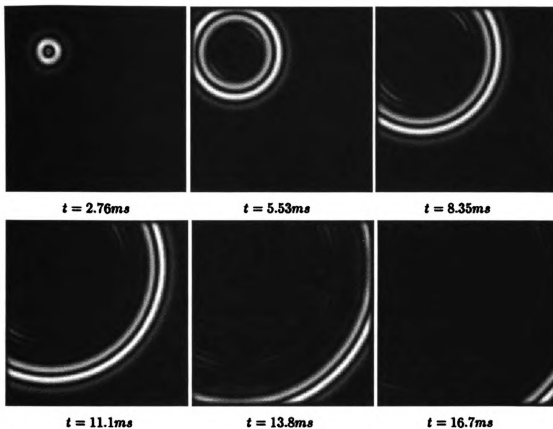


Figure 3-10 FDTD simulation results for the elastic wave propagation problem defined in Collino *et al.* [58] – Snapshots of absolute velocity over the entire domain caused due to an explosive source located at the top left corner of the domain

3.7.2 Simulation results on human thorax

Having validated the FDTD codes for stability and accuracy, they are then used to model the sound wave propagation in the thoracic cavity by discretizing a transverse cross-sectional slice image of the thorax acquired from the Visible Human Project as described in section (3.3). The spatial grid size was determined based on the number of spatial sample points (K_S) chosen to track the shortest wavelength in the medium. Thus,

if $c_{s,min}$ is the slowest shear wave to be traced and f_{max} is the bandwidth of the forcing function, then the grid size is obtained by

$$\Delta x = \Delta z = \frac{1}{K_s} \frac{c_{s,min}}{f_{max}} \quad (45)$$

The rectangular domain of $L_x \times L_z = 35 \text{ cm} \times 25 \text{ cm}$ enclosing the thorax was thus discretized into $N_x \times N_z$ cells using the grid size as determined in equation (45). PML layers, 5 cm thick, surrounded this rectangular domain on each side. The time-step was chosen to be 0.9 times the Courant limit as defined in equation (44). The forcing function f_z was a first derivative of a Gaussian pulse with a center frequency f_0 placed at the mitral valve location as described in section (3.5). The 2D FDTD codes were used to calculate the velocity and stress components at an array of locations (sensor locations) along the torso boundary and were stored at a desired sampling frequency F_S . Figure 3-11 shows the locations of the source and receivers in relation to the thoracic geometry. The location of the source is indicated by a white cross and the receivers on the front chest surface are represented by white circles. All the remaining receiver locations are represented by white triangles. The receivers are indexed in a clockwise manner, the index numbers of few of which are indicated in the figure.

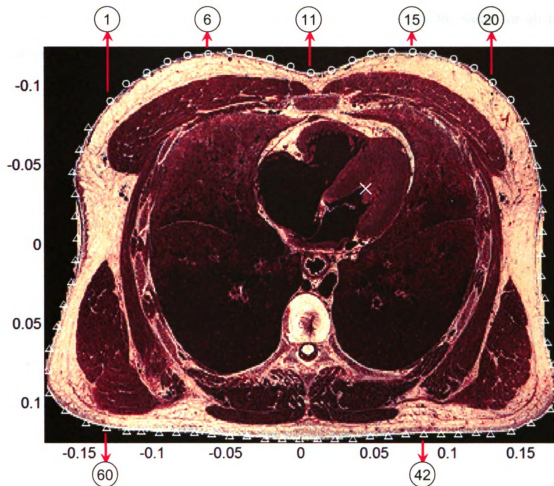


Figure 3-11 Source (white cross) and receiver (white circles and triangles) locations in the thoracic geometry. (The axes are in units of m).

The simulations used a center frequency f_0 of 300 Hz that yielded a 40 dB bandwidth of around 1 kHz. The forcing function f_z and its frequency spectrum are shown in Figures 3-12(a) and 3-12(b) respectively. The source-to-receiver transfer functions (TF) were computed for each of the receiver signals. The normal component of the velocity v_n was used for the receiver signals. Figure 3-13 and Figure 3-14 show the magnitude of the transfer functions of receiver #s 4, 8, 12, 16 and 20 in the frequency range of 0-100 Hz

and 100-400 Hz, respectively. Figure 3-15 and Figure 3-16 show the same for all the receivers around the torso as an image. The following parameter values were used in the FDTD codes to obtain these results [65].

Grid size : $\Delta x = \Delta z = 1mm$

Dimensions : $N_x = 350, N_z = 250, PML_{width} = 150 \text{ layers}$

Time step : $\Delta t = 0.15\mu\text{sec}$

Source function : $f_0 = 300\text{Hz}, A = 10^6$

Sampling frequency : $F_S = 8000\text{Hz}$

(46)

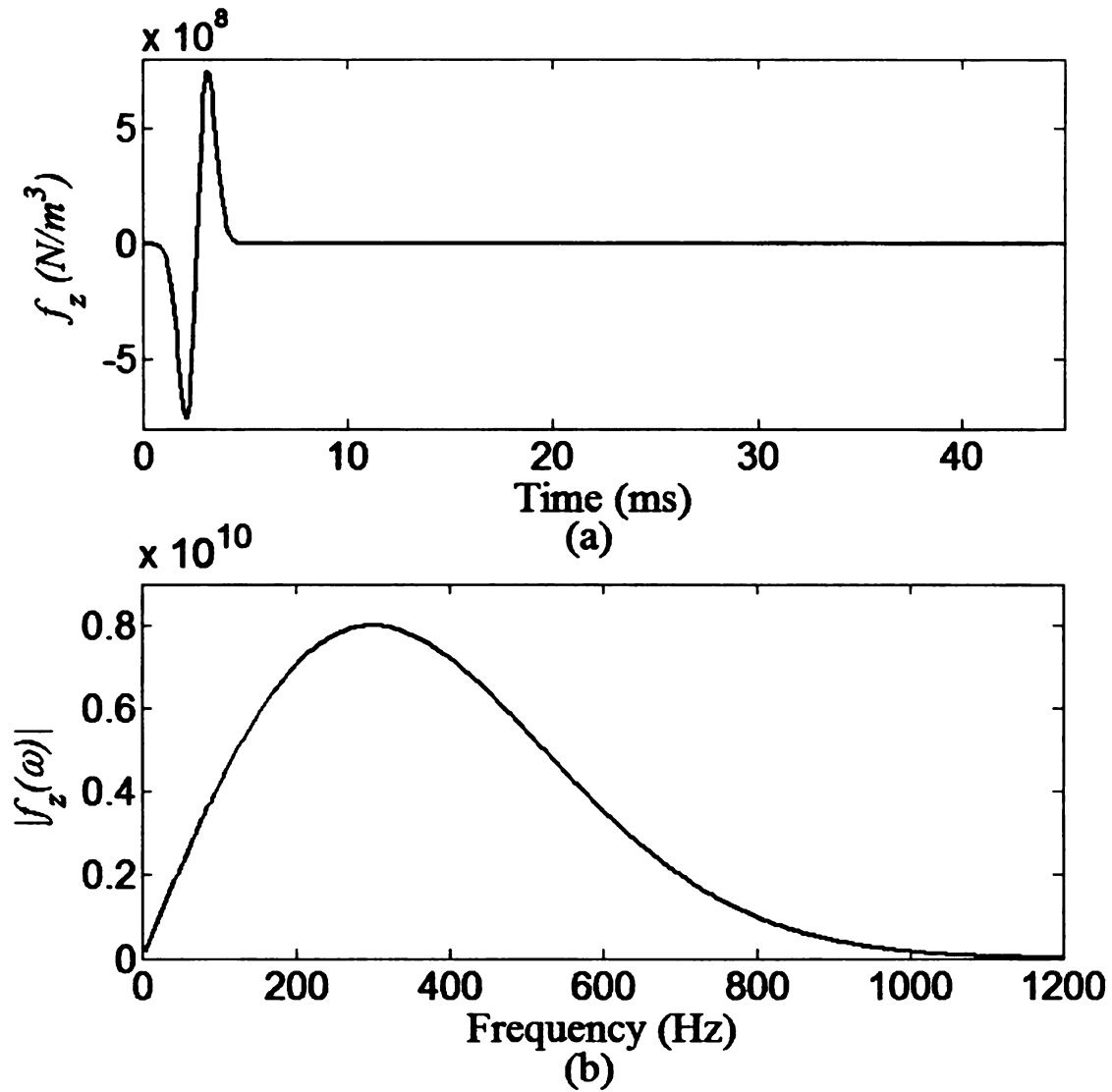


Figure 3-12 A 300Hz Gaussian first derivative source signal f_z used in the FDTD simulations (a) Time waveform of the forcing signal (b) Corresponding Fourier spectrum.

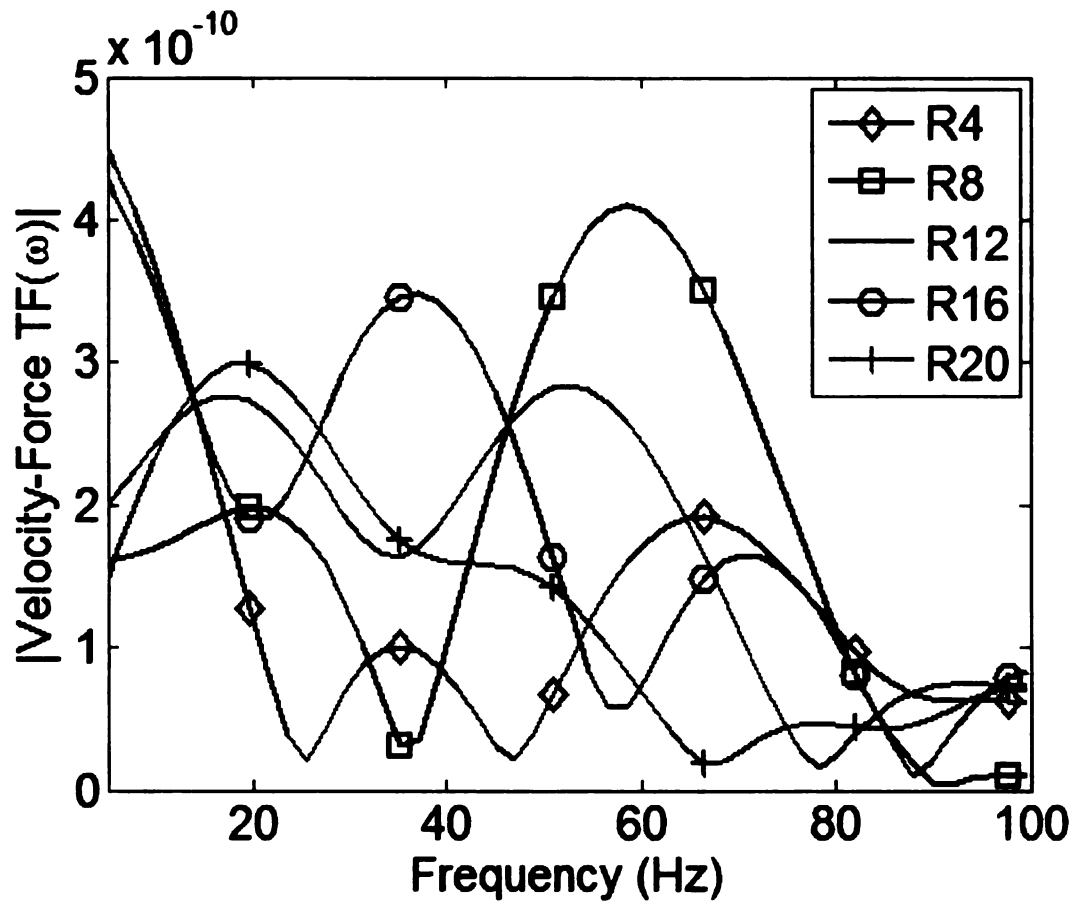


Figure 3-13 Magnitude of source-to-receiver transfer functions (TF) for a source at the mitral valve location – TF plots at receiver #s 4, 8, 12, 16 and 20 in the 0-100 Hz frequency range

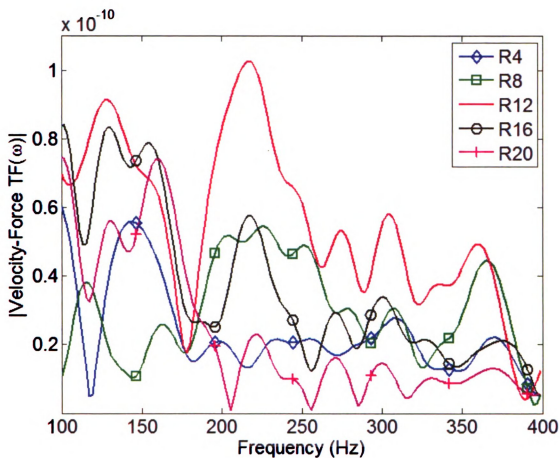


Figure 3-14 Magnitude of source-to-receiver transfer functions (TF) for a source at the mitral valve location – TF plots at receiver #s 4, 8, 12, 16 and 20 in the 100-400 Hz frequency range

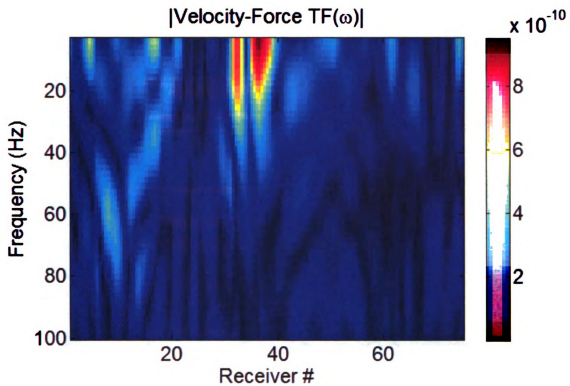


Figure 3-15 Magnitude of source-to-receiver transfer functions (TF) for a source at the mitral valve location – TF image at all receivers in the 0-100 Hz frequency range

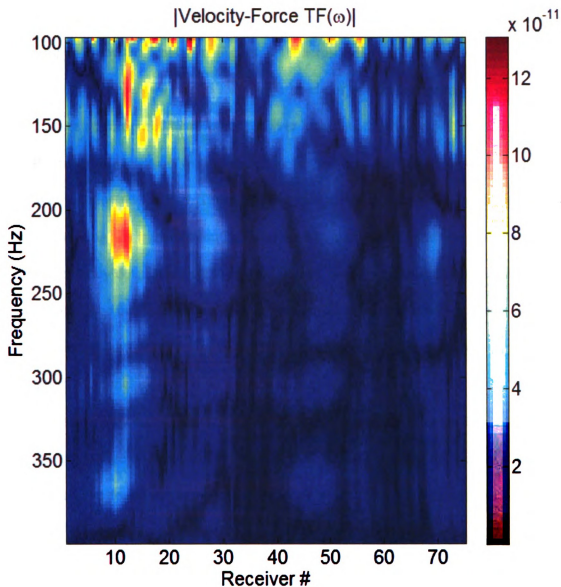


Figure 3-16 Magnitude of source-to-receiver transfer functions (TF) for a source at the mitral valve location – TF image at all receivers in the 100-400 Hz frequency range

From Figure 3-13 and Figure 3-14, it is clear that the heart-to-chest acoustic transfer functions at different receiver locations along the front surface of the thorax differ significantly, although, all of them have most of their energy content lying in the 80-80Hz frequency range. In Figure 3-14 we notice that all the receivers except #R8 have peaks

between 125 Hz and 170 Hz, and a distinct valley at around 180 Hz. Similar observation can be made from the image in Figure 3-16 across all the 20 receivers on the front surface. Also, receivers #8 to #15 have high levels of acoustic transmission in the 180-270 Hz range as compared to all other receiver locations. In Figure 3-15 we observe that the 0-40 Hz signals transmit well to the posterior left corner of the thorax corresponding to receiver location #32 to #40. These observations although cannot be conclusively used for characterizing the transmission paths of an S1 sound that originates from the mitral valve source, they do provide some limited insight into the auscultation sites around the torso that might be better suited for study of certain types of abnormal heart sounds.

The source model described in section (3.5) could be modified to simulate lung sound propagation by modeling explosive sources as suggested in equation (34) at the locations where the secondary bronchi meet the plane of cross-sectional slice in the lungs. Since the frequency range of lung sounds extend well beyond 1 kHz, the center frequency would then have to be set to a higher value of around 1 kHz to incorporate a wider bandwidth into the forcing function [1]. Consequently, the time step and spatial grid size would get reduced according to equations (44) – (45).

3.7.3 Wave Propagation Characteristics

In order to gain a better insight into the propagation of the viscoelastic waves originating from the source, we track the velocity components in the entire domain as a function of time. This allows us to observe the complex paths that the sound waves traverse as they reach the surface of the torso. The effect of the elasticity and viscosity of the various tissues in the thoracic cavity on the sound propagation can thus be studied using this model in an effective manner. Figure 3-17 shows the v_x and v_z component

distributions in the thorax at five time snapshots as the Gaussian first-derivative pulse source waveform propagates from the mitral valve location towards the periphery of the thorax [65]. At the 3 ms snapshot of the v_z image, we see that the initial wave-front of the sound waves have already reached the front surface of the torso right above the heart valve. This speedy conduction can be attributed to the absence of the lung lobes in these paths. The waves passing through the lungs are slowed down and severely attenuated as shown in the v_x and v_z images of all the remaining time snapshots. The images at 15 ms, 25 ms and 40 ms also show effects of multiple reflections at the heart-lung interface. A detailed quantitative and qualitative analysis of these snapshots involving tracing the waveforms in each tissue individually may be performed, if necessary.

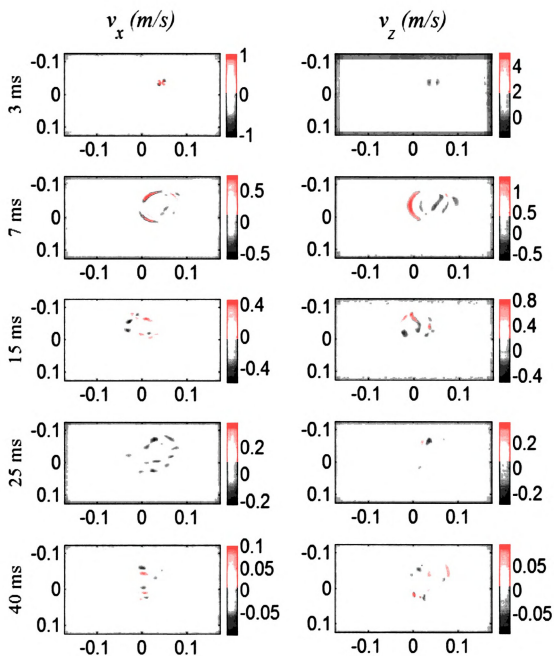


Figure 3-17 Snapshots (at 3, 7, 15, 25 and 40 ms) of velocity v_x and v_z distributions in the entire thorax as a sound wave caused due to a 300 Hz Gaussian first-derivative forcing source propagates from the mitral valve location. (The axes on each of the subplots are in units of m and the color-bars have units of m/s)

3.8 Effects of Anatomical Variations

The viscoelastic FDTD model of the thorax can be used to study the effects of rib structures, shear elasticity of tissues, and size of the thoracic cavity on the signals reaching the surface of the thorax by making subtle modifications to the parameters. The study, whilst aids understanding the effects of such anatomical variations, also justifies the need to incorporate shear elasticity and rib structures into the thoracic geometry.

3.8.1 Effects of ribs and shear elasticity of tissues

It is clear from Table 3-1 to Table 3-4 that the ribs and bones have distinctly different material properties as compared to the other tissues. One thus expects their presence to cause a significant impact on the sound waves reaching the chest surface. A simulation study to observe the effects of ribs on the signals is conducted by assigning the material properties of the muscles to the rib and bone structures. The waveforms thus obtained are compared to the signals obtained on a normal thorax. Similarly, a simulation was carried out to study the effect of shear elasticity of the tissues on the sound signals. This was performed primarily to justify the inclusion of shear elasticity into the model. The coefficient of shear elasticity μ_l was set to zero in the entire domain to simulate the shear-less case. The normal component of the velocity v_n obtained at receiver #15 for a normal thorax, rib-less thorax and shear-less thorax are compared in Figure 3-18 [65]. The simulations used the same parameters as listed in section (3.7.2) in equation (46). Results indicate that the presence of ribs clearly attenuates the signals significantly, although the overall shape of the waveform is not affected as much. However, the

absence of shear elasticity in the thorax results in a completely different waveform shape, thereby illustrating the importance of inclusion of shear elasticity in the model.

Since the shear-wave contribution in certain tissues like the lung-parenchyma are insignificant compared to that of the compressional waves, more efficient numerical schemes could ideally be employed in such regions [5]. However, this would require a more diligent analysis to tackle the internal boundary conditions. The FDTD numerical scheme used in the current work simplifies the task and provides a generic framework, which may be applied to modeling various anatomical and pathological conditions too.

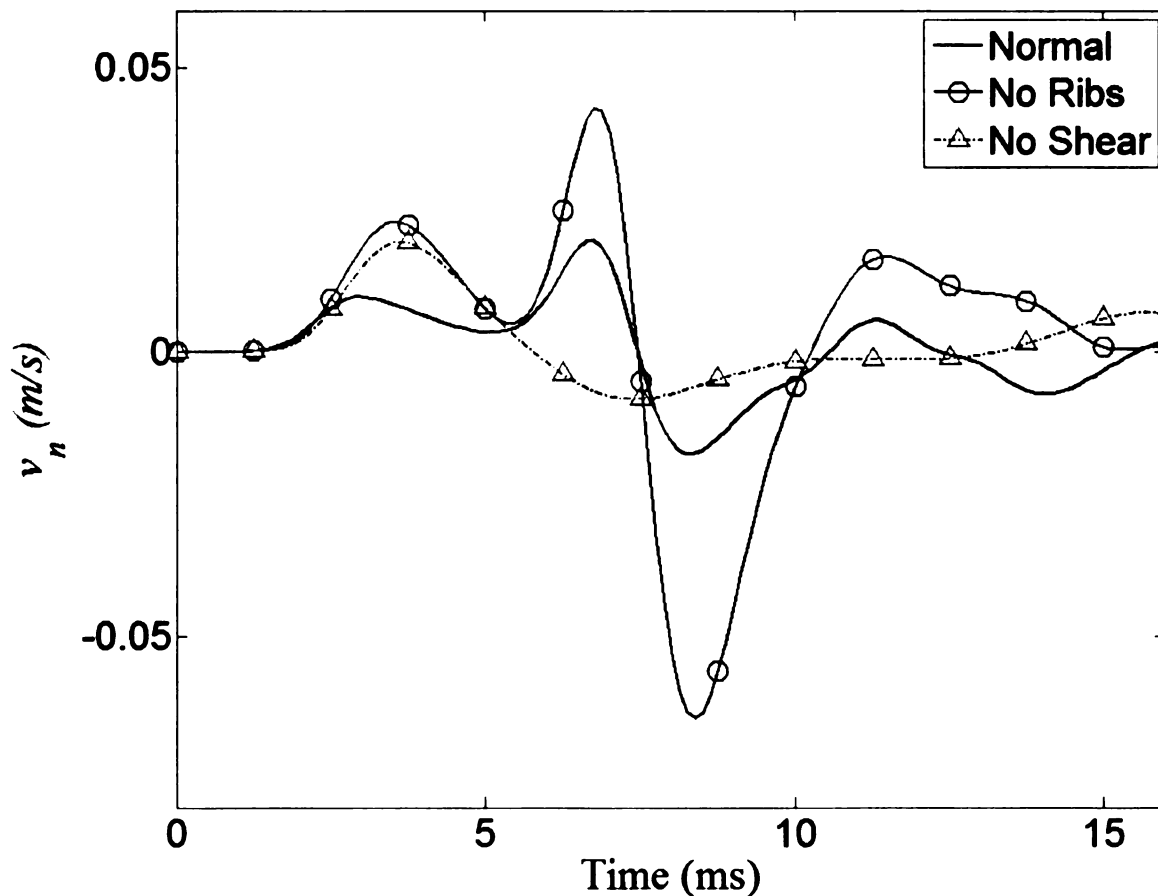


Figure 3-18 Normal component of the velocity v_n at receiver #15 due to a 300 Hz Gaussian first-derivative forcing source at the mitral valve location under three cases – normal thorax, rib-less thorax and shear-less thorax

3.8.2 Effect of size of thorax

All the simulations in the preceding sections have assumed a fixed rectangular domain of $L_x \times L_z = 35 \text{ cm} \times 25 \text{ cm}$ enclosing the thorax. As one would expect, the size of the thorax might also have an effect of the receiver signals. In order to study this, the original thorax image was linearly resized to fit into 30 cm x 20 cm and 40 cm x 30 cm rectangular domains and FDTD simulations were carried out with the same spatial and time discretization. The normal component of the velocity v_n obtained at receiver #12 for the three different thorax sizes are compared in Figure 3-19 [65]. Results indicate that while the amplitude of the signal corresponding to a larger sized thorax is smaller and time-delayed compared to that of the smaller sized thorax, the shape of the waveform is retained atleast upto the first wavefront, corresponding to the dominant longitudinal wave peak and the shear wave peak. The secondary reflections caused by, presumably the rib structures, are not as prominent in the 40 cm X 30 cm thorax as in the 30 cm X 20 cm thorax.

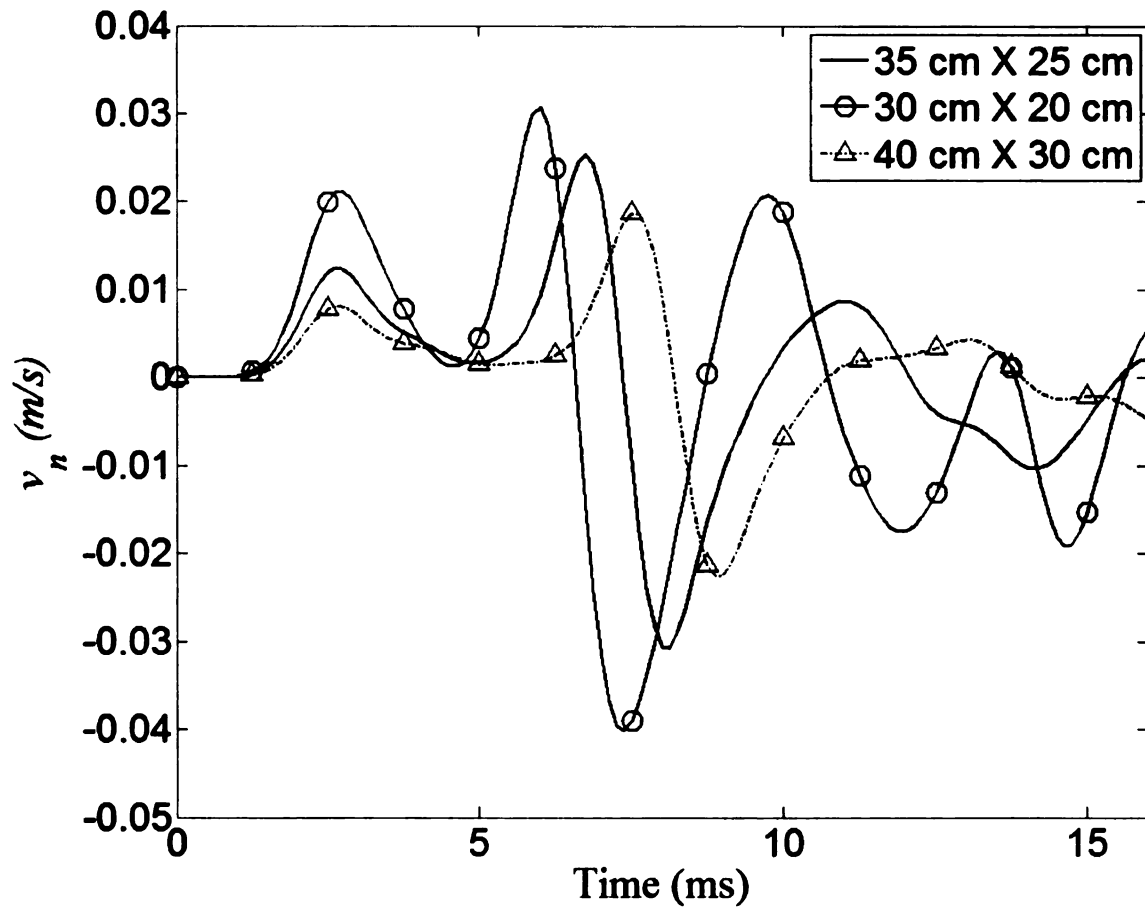


Figure 3-19 Normal component of the velocity v_n at receiver #12 due to a 300 Hz Gaussian first-derivative forcing source at the mitral valve location for three different thorax sizes ($L_x \times L_z$) – 35 cm X 25 cm, 30 cm X 20 cm and 40 cm X 30 cm

CHAPTER 4

STUDY OF SOUNDS UNDER PNEUMOTHORAX CONDITIONS

4.1 Introduction

Pneumothorax is a pathological condition of the lungs in which air collects in the pleural space, i.e. the space that surrounds the lungs, leading to a lung-collapse eventually. Since it is a potentially life threatening disease, and is easily treatable when diagnosed early, there is significant interest in developing a noninvasive, low-cost, quick and advanced diagnostic scheme. Currently, the gold-standard technique for diagnosis of pneumothorax is the chest X-ray or a chest CT although misdiagnosis rates of around 30% have been reported even with these methods [66], [67].

Auscultation sounds offer a viable alternative for the diagnosis of various thoracic pathologies including pneumothorax [68]. Prior experimental studies have shown the effectiveness of breath sounds in differentiating between normal and pneumothorax conditions. By digitizing these sounds using acoustic sensors mounted around the torso, and combined with an intelligent multi-sensor processing scheme, one could devise a low-cost, noninvasive and portable solution for accurate diagnosis that may be even used for out-patient home monitoring purposes. As mentioned in section (1.1) an accurate sound propagation forward model simulating pneumothorax conditions can aid in the development of such multi-sensor processing schemes.

The model would facilitate the study of effects of pneumothorax on the acoustic sensor signals and can be used to develop and validate various multi-sensor processing

algorithms for diagnostic purposes. It also allows one to develop newer inverse problem solutions to localize and quantify the size of the pneumothoracic air cavity in the thorax.

Section (4.2) provides simulations details pertaining to modeling the pneumothorax conditions using the FDTD codes. Preliminary simulation results demonstrating the effect of varying sizes of air cavity on the source-to-sensor transfer functions are presented in section (4.3). Concluding remarks discussing the future steps to be taken to address some of the unresolved issues are also discussed in section (4.3).

4.2 Simulation of Pneumothorax

As described earlier in section (4.1), a pneumothorax is basically an air pocket trapped in the pleural space between the lung and the chest wall. The condition is thus modeled by introducing a region at the exterior edge of the lung that has material properties of air, as shown in Figure 4-1. In order to study the effect of the size of the air-pocket on the chest signals, sizes varying from 1.7 cm to 5 cm was introduced, size being defined as the maximum extent of the air cavity.

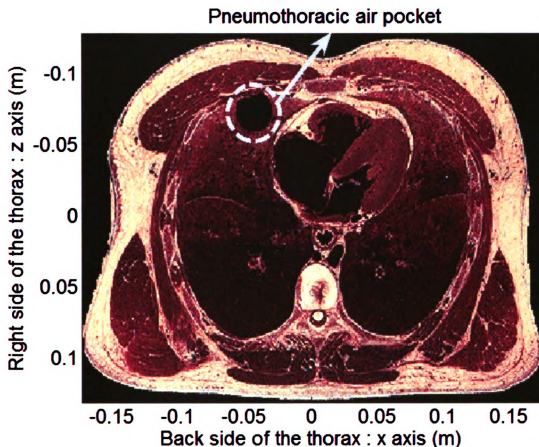


Figure 4-1 Anatomical simulation of a pneumothoracic air cavity on a 2D cross-sectional slice of the human thorax

To model the sound wave propagation in the thoracic cavity, we first discretize the transverse cross-sectional slice image of the thorax. The rectangular domain of $L_x \times L_z = 35 \text{ cm} \times 25 \text{ cm}$ enclosing the thorax is discretized into $N_x \times N_z$ cells using the grid size as determined in equation (45). PML layers, 15 cm thick, surrounded this rectangular domain on each side. The time step was chosen to be 0.8 times the Courant limit as defined in equation (44).

The 2D FDTD codes were used to calculate the velocity and stress components at an array of sensor locations placed all around the torso. Subsequently, the mean pressure, p was computed using the normal stress components as follows:

$$p = -(T_{xx} + T_{zz})/2 \quad (47)$$

The FDTD simulations assumed the Maxwell's model of viscoelasticity for the entire domain and used the following parameter values [69]:

$$\begin{aligned} \text{Grid size : } \Delta x = \Delta z &= 1 \text{ mm} \\ \text{Dimensions : } N_x = 350, N_z &= 250, \\ &PML_{width} = 150 \text{ layers} \\ \text{Time step : } \Delta t &= 0.15 \mu \text{ sec} \\ \text{Source function : } f_0 = 300 \text{ Hz}, A &= 10^6 \\ \text{Sampling frequency : } F_S &= 8000 \text{ Hz} \\ \gamma \text{ values : } \gamma_{xx} = \gamma_{zz} = \gamma_{xz} &= 300 \forall x, z \end{aligned} \quad (48)$$

4.3 Results and Conclusion

Using the simulated pressure waveforms at the sensor locations around the torso and the source forcing function, the source-to-sensor transfer functions (TF) were computed for each pneumothorax simulation. For ease of analysis, we consider only one of the key sensor locations on the front surface of the chest, indicated by a blue cross in the left column of thorax anatomy images of Figure 4-2. The source location is indicated by the white circle in the images. These images represent the various pneumothorax conditions simulated with increasing degree of severity going from top to bottom, the labels on the left indicating the size of the air cavity. The right column plots in Figure 4-2 represent the amplitudes of the source-to-sensor pressure TFs for the corresponding pneumothorax condition. The image and TF plot in the first row corresponds to a normal thorax. The maximum amplitude of the TF obtained for the normal thorax is used as the scaling factor for all the plots in this figure and subsequent figures.

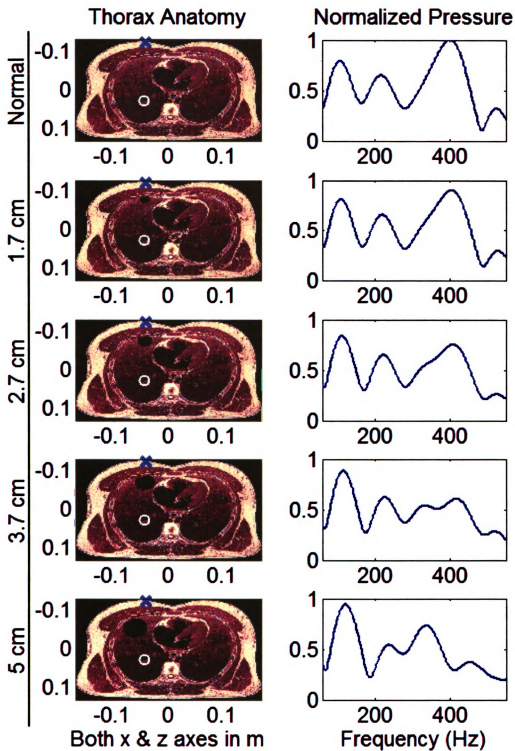


Figure 4-2 Left column of images show the cross-sectional slice of the thorax for varying sizes of the pneumothoracic air pocket in the lung. The labels on the left side indicate the size of the air pocket. The right column of plots represent the corresponding amplitude of the source(o)-to-sensor(x) transfer functions.

In order to further study and compare these TFs, Figure 4-3 plots these on one common axis. We notice that at frequencies around 50-100 Hz there isn't any significant difference in the amplitudes of the TFs. However, the frequency range of 350-475 Hz shows a distinct trend of decreasing amplitudes with increasing degree of severity of pneumothorax. Figure 4-4 considers the amplitudes of the difference transfer functions (DTF), computed as:

$$DTF = TF(Pneumothorax) - TF(Normal) \tag{49}$$

The plot shows that the deviation of the TF from the normal case is the largest for the pneumothorax with the largest air cavity (5 cm, in this case), and shows a clear trend across all the cavity sizes. More importantly, this deviation is enhanced in the 350-475 Hz frequency range, thereby providing some additional insight into possible diagnostic utility of chest signals measured in this frequency range.

Similar results may be obtained from other sensor sites too. As one would expect, sites located significantly distant from the air cavity do not show such prominent deviation. Thus, by combining information from various sensor sites, one could devise a multi-sensor noninvasive auscultatory system for diagnosis of pneumothorax conditions.

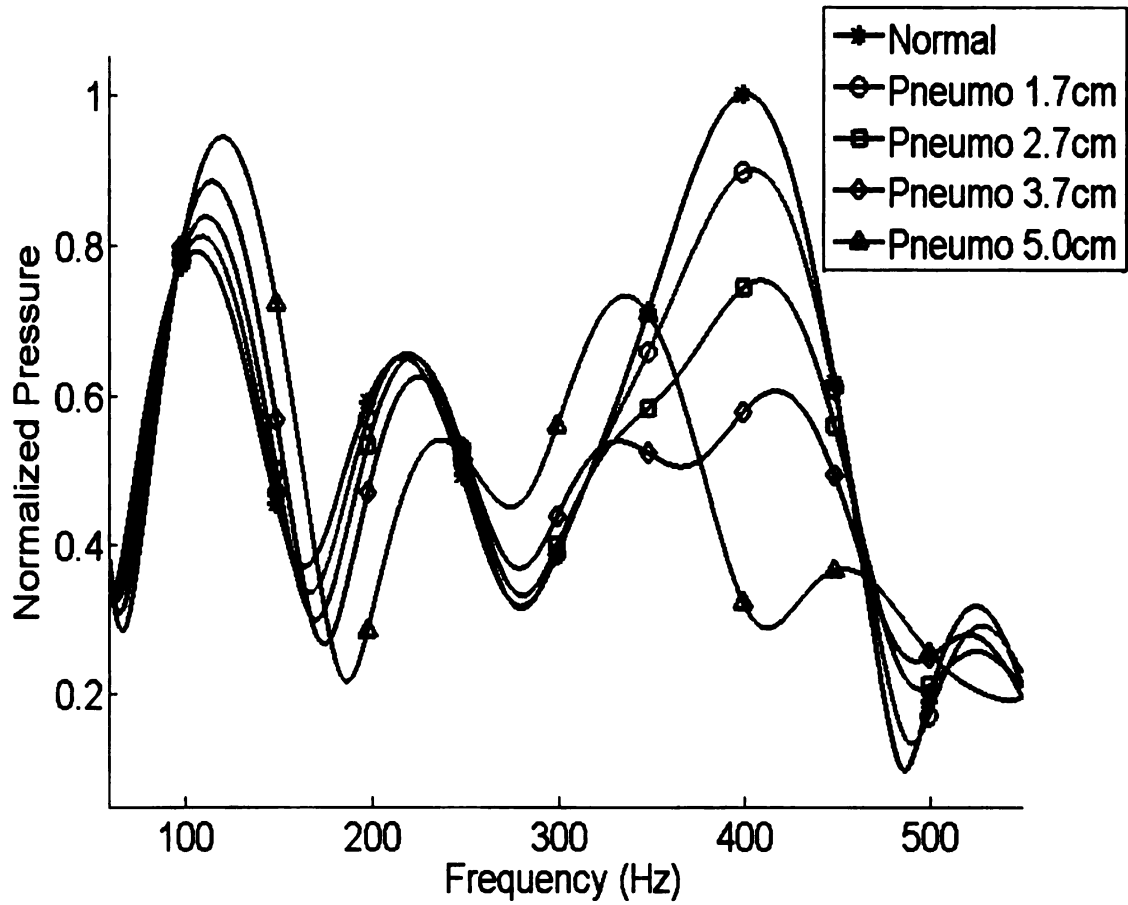


Figure 4-3 Comparison of the amplitudes of the source-to-sensor transfer functions corresponding to varying sizes of the pneumothoracic air pocket

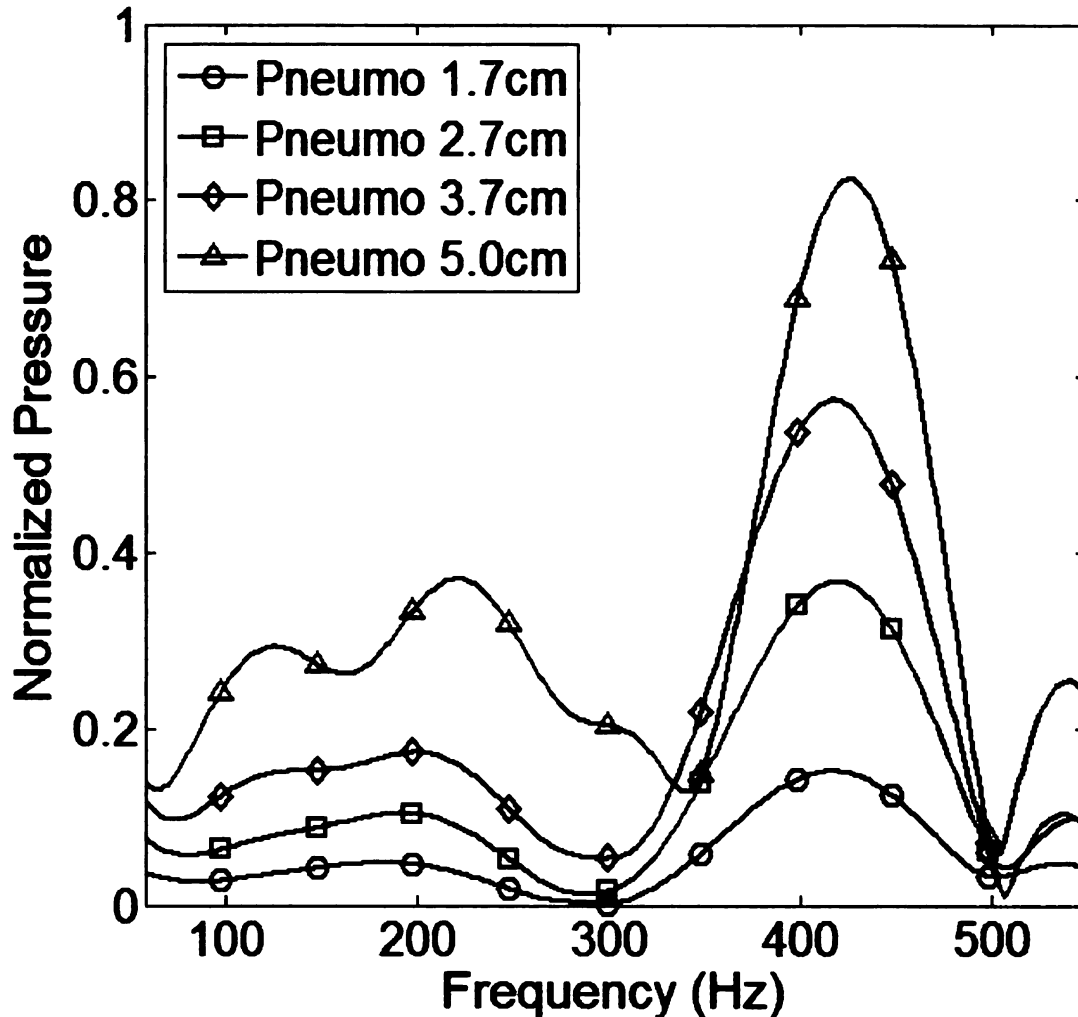


Figure 4-4 Comparison of amplitudes of difference of the transfer functions of varying degrees of pneumothorax severity and that of a normal thorax

The 2D numerical FDTD viscoelastic model developed in chapter (3) has thus been used to study the lung sound propagation in the human thoracic cavity under pneumothorax conditions. The model provides a convenient test-bed to investigate the possibility of using an array of noninvasive acoustic sensors for diagnosing pneumothorax and estimating the extent of severity of the disease. Future efforts would be directed towards developing a 3D model of the torso that may provide a more accurate

representation of the thoracic sounds. Studies pertaining to effects of the location of the cavity in the thorax would be considered. Furthermore, the models could be used to design and evaluate various inversion schemes that can be used to estimate the location and size of the air cavity.

CHAPTER 5

SOURCE LOCALIZATION

5.1 Introduction

Physicians and doctors listen to auscultation sounds and are able to diagnose various heart and lung pathologies using single stethoscope measurements made at distinct sites on the torso. This diagnostic ability can be significantly enhanced with a multi-sensor system that makes simultaneous recordings at a bunch of auscultation sites around the torso. In addition to allowing the physician to listen to or even view the sound signatures of the simultaneously recorded sounds, a multi-sensor system can be used to combine the sensor recordings in an optimal manner to localize the sound, i.e. identify the exact locations of the intra-thoracic acoustic sources. Given the locations of the sources, it may then be used to amplify the sounds originating from only a particular source in the thorax while suppressing the interfering sounds from other sources, thereby aiding physicians in diagnosis. Source localization for thorax can thus assist in developing improved non-invasive diagnostic solutions.

The viscoelastic numerical model of the thorax discussed in the previous chapters can be used as a convenient test bed for validating many of the traditional source localization algorithms as well as development of newer and better schemes. The sections to follow discuss the some of the algorithms used traditionally and assess their performance to this application. Further, an alternate algorithm based on the viscoelastic model is proposed

and assessed. Finally, a modified version of the traditional algorithm is proposed to alleviate some of the problems associated with it.

5.1.1 Beamforming concept

The algorithms that combine the information from distinct, spatially separated, simultaneous recording sensors to localize the sources are popularly termed as beamformers [70]. The beamformer usually weights and combines the sensor signals in an optimal fashion so as to extract the desired signal of a particular frequency originating from a particular point in space while suppressing all contributions of signals from other points in space. One of the challenges associated with beamforming to a desired source thus is, noise and interference from undesirable sources as illustrated in Figure 5-1. If $x_i(n)$ denote the N sensor signals and w_i denote the corresponding weights, $i = 1, 2, \dots, N$, then the beamformer output signal $y(n)$ is given by:

$$y(n) = \sum_{i=1}^N w_i x_i(n) \tag{50}$$

The above is typically expressed in vector form as $\mathbf{y} = \mathbf{w}^H \mathbf{x}$, where $\mathbf{w} = [w_1, w_2, \dots, w_N]$ is the weighting vector that is optimally determined by the beamforming algorithms to meet the desired response of the beamformer.

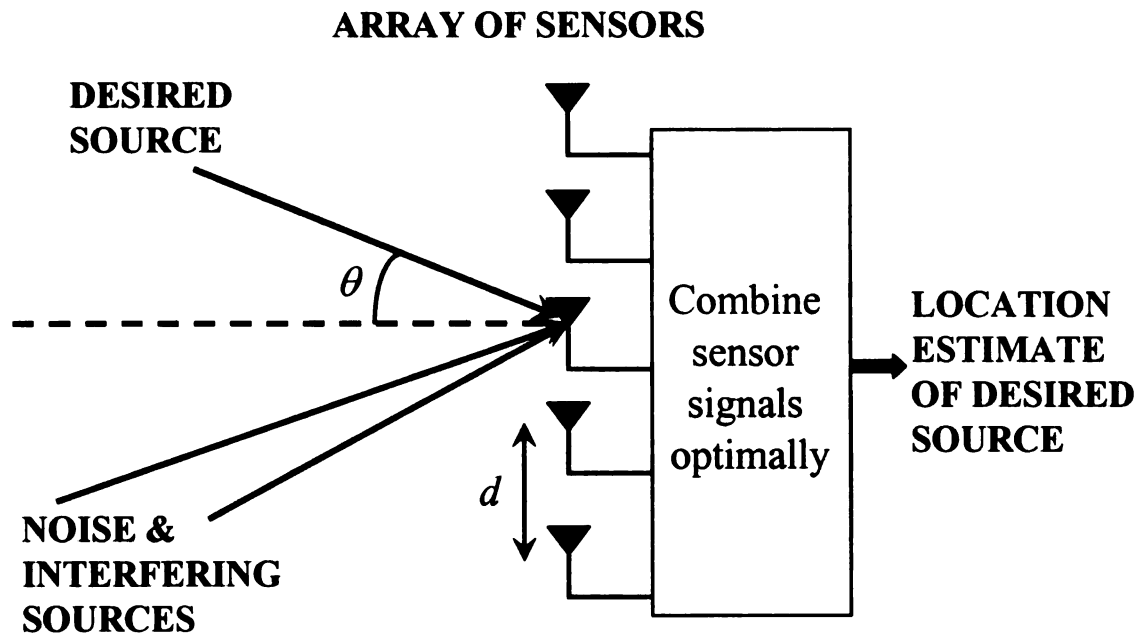


Figure 5-1 Concept of beamforming

The basic element of all beamforming algorithms is a wave propagation model that relates the source signal to the received sensor signals. Hence, the performance of the beamformer not only depends on the strength of noise and interfering sources, but also on relevance of the assumed wave propagation model. Many of the traditionally employed beamforming algorithms were originally developed for radar signal processing and far field applications where the wave propagation model essentially contains a phase delay. However, the current application of sound source localization in the thorax is predominantly a near-field problem, which is far more complex. In recent times, there have been attempts to modify the far-field models to make them suitable to near field propagation problems [3], [4]. However, the extension from far-field to near-field as assumed by these algorithms hold good, if at all, only in a homogeneous medium of transmission. Thus, in practice, the algorithms governed by the near-field propagation

model may have to be tweaked by controlling a few parameters that optimize their performance in complex media of the thorax.

5.1.2 Near-Field Propagation Model

The near-field propagation model assumed by the algorithms is based upon a spherical wave-front transmission through a homogeneous medium of velocity c . Assume there are N sensors receiving signals from K acoustic sources. Let r_{0k} denote the distance of the k^{th} source from the reference sensor and r_{ik} denote the distance of the k^{th} source from the i^{th} sensor as shown below in Figure 5-2.

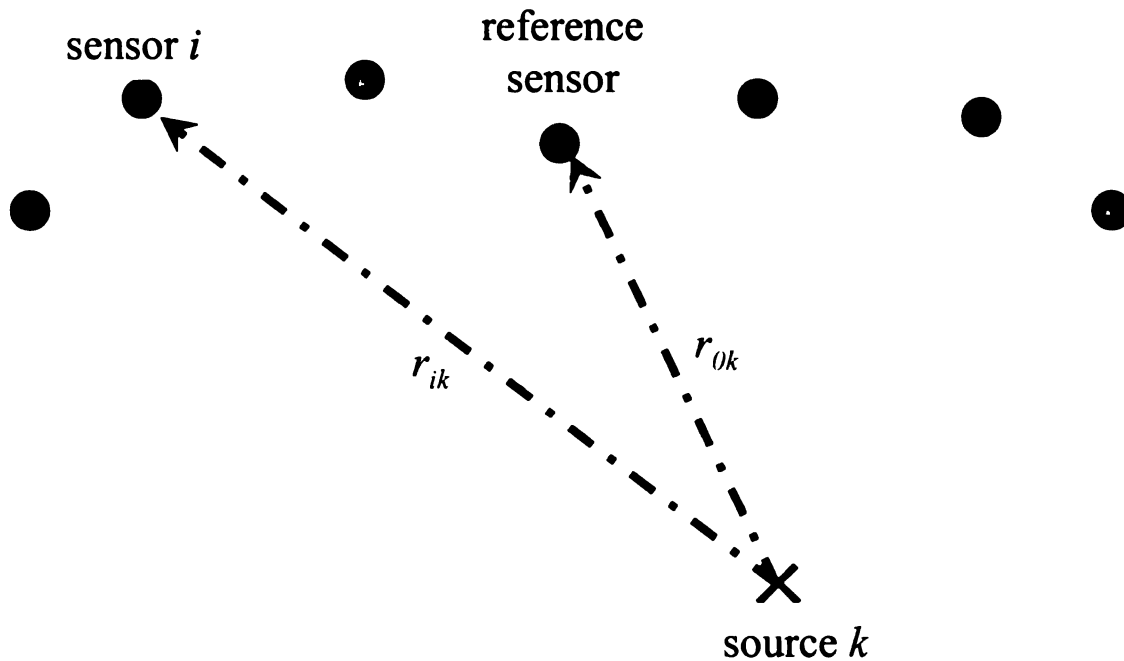


Figure 5-2 Near-field propagation model

If $s_k(t)$ represents the k^{th} source waveform of frequency f , then according to the model, the i^{th} sensor signal $x_i(t)$ can be expressed as in equations (51) and (52). The

noise contribution $n_i(t)$ at each sensor is usually modeled as a zero-mean i.i.d (independent identically distributed) Gaussian noise with variance σ^2 .

$$x_i(t) = \sum_{k=1}^K s_k(t) a_{ik}(r_{0k}, r_{ik}, f, t) + n_i(t), \quad 1 \leq i \leq N \quad (51)$$

where

$$a_{ik}(r_{0k}, r_{ik}, f, t) = \left(\frac{r_{0k}}{r_{ik}} \right)^\beta \exp\left(-\eta \frac{r_{ik}}{r_{0k}} \right) \exp\left(-j2\pi f \frac{r_{ik} - r_{0k}}{c} \right) \quad (52)$$

The vector $\mathbf{a}_k = [a_{1k} \ a_{2k} \ \dots \ a_{Nk}]^T$ is popularly termed as the steering vector, while the a_{ik} 's describe the near-field propagation model [3], [71]. In equation (52), we notice that the model contains three explicit terms that are described below:

- (i) The first term is related to the geometric spreading loss due to the spherical wave expanding from an omnidirectional point source. The factor β , called the geometric spreading loss factor takes a value of 1 for a homogeneous medium.
- (ii) The second term is associated with the energy loss per unit volume in a lossy homogeneous medium, and the factor η is correspondingly called the exponential loss factor of the medium.
- (iii) The last term corresponds to the phase correction associated with the time delay for the signal to propagate from the source to the sensor. The average velocity of propagation c plays an important role in this term.

Clearly, in the above model, the three factors (β , η , c) do not possess a well defined meaning while being used in a complex heterogeneous thoracic medium. Hence these factors are chosen from a range of values that optimize the performance of the algorithms.

The following section shall describe three different source localization algorithms that were implemented to validate their utility for localizing an acoustic source in the human thorax. Results obtained using these algorithms have been discussed in the subsequent section.

5.2 Near-Field Propagation Model based Source Localization

Algorithms

The three algorithms employing the near-field propagation model described in the previous subsection considered are:

- i) Multiple Signal Classification method (MUSIC)
- ii) Conventional Focused Beamformer (CFB)
- iii) Linearly Constrained Minimum Variance beamformer (LCMV)

5.2.1 Multiple Signal Classification (MUSIC)

The MUSIC algorithm [3], [72] is a subspace-based estimation technique that uses the eigen structure of the sensor data-covariance matrix to determine the source locations. Using equation (51), the data covariance matrix $\mathbf{R} = E\{\mathbf{xx}^H\}$ can be expressed as follows:

$$\mathbf{R} = \mathbf{A}E\{\mathbf{ss}^H\}\mathbf{A}^H + \sigma^2\mathbf{I} = \mathbf{A}\mathbf{R}_s\mathbf{A}^H + \sigma^2\mathbf{I} \quad (53)$$

where $\mathbf{A} = [a_1, a_2, \dots, a_K]$ is the steering matrix and \mathbf{I} is the identity matrix obtained assuming a spatially white Gaussian noise distribution. It is clear from equation (53) that if there exists K incoherent sources, then the singular value decomposition of \mathbf{R} will result in K signal eigen-vectors (with an eigen-value $\sigma_k^2 + \sigma^2$, $k = 1, 2, \dots, K$ where each σ_k^2 corresponds to the signal power of the k^{th} source signal) and $(N - K)$ noise eigen-

vectors (each with an eigen value of σ^2). Thus, if v_k is a noise eigen-vector (i.e. $k > K$),

then the following hold good:

$$\mathbf{R}v_k = \sigma^2 v_k$$

$$\Rightarrow (\mathbf{A}\mathbf{R}_s\mathbf{A}^H + \sigma^2\mathbf{I})v_k = \sigma^2 v_k \quad \dots \text{ from equation (53)}$$

$$\Rightarrow \mathbf{A}\mathbf{R}_s\mathbf{A}^H v_k = 0$$

$$\Rightarrow \mathbf{A}^H v_k = 0 \quad (\text{since } \mathbf{R}_s \text{ and } \mathbf{A} \text{ are both of rank } K)$$

This implies that the $(N - K)$ noise eigen-vectors are orthogonal to the K source direction vectors, and lie in the null-space of \mathbf{A} . This forms the basis for most of the eigen-vector based algorithms. The MUSIC algorithm uses this concept and estimates the source locations by identifying the peaks of a function defined as follows:

$$P(r, \theta, \phi) = \frac{1}{\left\| \sum_{k=K+1}^N v_k^H a(r, \theta, \phi) \right\|^2} \quad (54)$$

where $a(r, \theta, \phi)$ is the near-field propagation model based steering vector corresponding to the location (r, θ, ϕ) in the search space. If $a(r, \theta, \phi)$ corresponds to the steering vector from a source location, then the denominator of the function approaches zero, thus peaking the function at that location.

5.2.2 Conventional Focused Beamformer (CFB)

The conventional focused beamformer, also called as Bartlett beamformer, determines the weights defined in equation (50) by maximizing the output power [72]. In

other words, the optimal weight vector \mathbf{w} is obtained by maximizing the quantity $E\{\mathbf{y}\mathbf{y}^H\}=\mathbf{w}^H\mathbf{R}\mathbf{w}$. In order to obtain a non-trivial solution the weight vector is restricted to have a norm of 1. Substituting the sensor signal model as defined in equation (51) into the output power expression, we can obtain the optimal weight vector \mathbf{w} solution as:

$$\mathbf{w} = \frac{a(r, \theta, \phi)}{\sqrt{a^H(r, \theta, \phi)a(r, \theta, \phi)}} \quad (55)$$

The expression for the output power thus becomes:

$$P(r, \theta, \phi) = \frac{a^H(r, \theta, \phi)\mathbf{R}a(r, \theta, \phi)}{a^H(r, \theta, \phi)a(r, \theta, \phi)} \quad (56)$$

Thus, the source location for the CFB is obtained by finding the (r, θ, ϕ) in the search space that maximizes $P(r, \theta, \phi)$ in equation (56).

5.2.3 Linearly Constrained Minimum Variance Beamformer (LCMV)

The linearly constrained minimum variance beamformer, also termed as the Capon's beamformer, finds the optimal weight vector \mathbf{w} by minimizing the variance in the output while subject to constraints that preserve the signals from certain desired directions and minimize contributions from noise or interfering sources arriving from other directions [71], [72]. If $\mathbf{C} = [a_{c1}, a_{c2}, \dots, a_{cq}]$ are the q constraint steering vector directions and $\mathbf{g} = [g_1, g_2, \dots, g_q]^T$ are the corresponding constraint values, then the LCMV formulates the problem as:

$$\min_{\mathbf{w}} \mathbf{w}^H \mathbf{R} \mathbf{w} \quad \text{subject to} \quad \mathbf{C}^H \mathbf{w} = \mathbf{g} \quad (57)$$

The optimum weights are then provided by:

$$\mathbf{w} = \mathbf{R}^{-1} \mathbf{C} [\mathbf{C}^H \mathbf{R}^{-1} \mathbf{C}]^{-1} \mathbf{g} \quad (58)$$

The output power for this weight vector thus becomes:

$$P(r, \theta, \phi) = \mathbf{g}^H [\mathbf{C}^H \mathbf{R}^{-1} \mathbf{C}]^{-1} \mathbf{g} \quad (59)$$

One of the most popular approaches of LCMV is to minimize the output power contributed by noise and any signals coming from directions other than (r, θ, ϕ) while maintaining a fixed unity gain in the (r, θ, ϕ) direction, i.e. the constraint matrix \mathbf{C} is set to $\mathbf{a}(r, \theta, \phi)$ and \mathbf{g} to 1. In such cases, equation (59) becomes:

$$P(r, \theta, \phi) = \frac{1}{\mathbf{a}^H(r, \theta, \phi) \mathbf{R}^{-1} \mathbf{a}(r, \theta, \phi)} \quad (60)$$

Thus, the source location for the LCMV is obtained by finding the (r, θ, ϕ) in the search space that maximizes $P(r, \theta, \phi)$ in equation (60).

5.3 Algorithm Parameters

In the sections to follow, each of the above discussed source localization algorithms are tested on the simulated thorax signals obtained using the viscoelastic FDTD model in Chapter 3. The search for the intra-thoracic source location is carried out in a fixed rectangular x - z search space of $D_x \times D_z = 22.4 \text{ cm} \times 19.2 \text{ cm}$ inside the thorax that is discretized into tiny rectangular cells governed by the spatial grid-size parameter. Figure 5-3 shows this search domain and the corresponding grid size. The steering vector $a(x, z)$ corresponding to the center of each of these cells is used to compute the power $P(x, z)$ for each (x, z) cell. For all the simulations, the spatial grid size was set to 8 mm \times 8 mm. A finer grid size could yield more accurate results in cases where the true source location does not coincide with the center of a cell. However, a search over a finer grid space requires more computational time.

Search Space and Grid Size

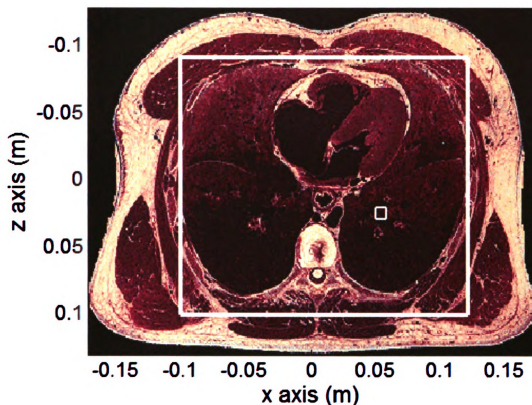


Figure 5-3 The outer white box corresponds to the x - z search space used in the algorithms. The inner white box shows the size of the finest cell used in the search.

The three parameters governing the near-field propagation model as described in section (5.1.2) were optimized as follows:

- (i) The geometric spread factor β was set to 2 as this yielded the best results for all cases.
- (ii) The loss factor η was searched over two values of 0 and 1. For cases pertaining to a homogeneous medium, η was set to 0.

- (iii) The velocity c was searched over a wide range of values from 5 m/s to 3500 m/s as plotted in Figure 5-4. For cases, pertaining to a homogeneous medium, the search was conducted over [100 m/s, 1500 m/s, 1605 m/s].

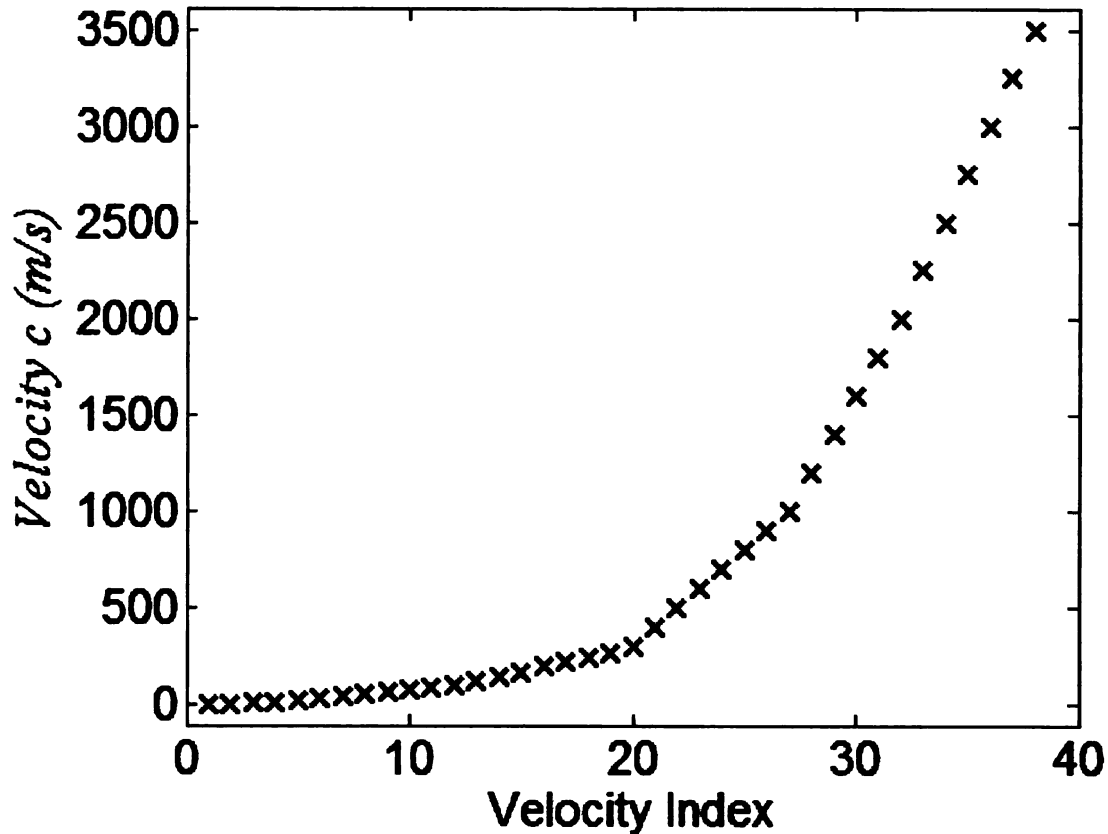


Figure 5-4 Velocity c search values

The sensor locations play a key role in most source localization algorithms. Optimization of sensor locations, however, is an extremely challenging problem and beyond the scope of this work. Typically, most applications employ an evenly spaced distribution of sensors to their problems. A similar approach has been chosen here. Simulated signals from a set of 19 receiver sites, evenly spaced along the periphery of the torso have been employed for source localization except for one case in section (5.5.1)

that uses only 5 sensors on the front surface of the torso. Figure 5-5 shows the receiver index numbers and corresponding locations on the thorax surface.

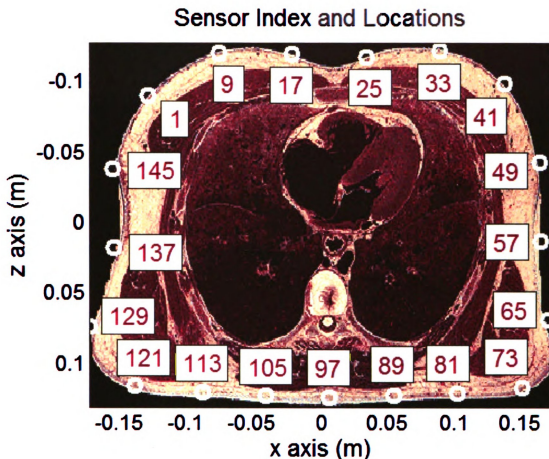


Figure 5-5 Sensor index and locations of the 19 sensor sites used in the source localization algorithms

In addition to the location of the sensor, the type of sensor measurement also plays an important role in many applications. Pressure, velocity, acceleration, and displacement are the most commonly measured quantities for sound studies. In the current work, both the mean pressure p and normal component of the velocity v_n are used for source localization. Results obtained using both of these are reported.

Finally, the number of time snapshots and the time-window of the sensor signals used also dictate the performance of the algorithms. A time-window of 16.5 ms sampled at 8 kHz was used in the current work. Other shorter windows were also evaluated; but none of them yielded significantly better results.

5.4 Algorithm Testing Procedure

The following test protocol was adhered to assess the performance of each of the source localization algorithms discussed in this chapter.

- (i) The sensor signals, both p and v_n were obtained from the viscoelastic FDTD simulations that used a 300 Hz Gaussian first derivative pulse as the f_z sourcing function.
- (ii) White Gaussian noise of varying Signal-to-Noise Ratio (SNR) levels, ranging from 15 dB to -10 dB, was added to artificially introduce noise into the sensor signals. Figure 5-6 compares the noisy waveforms of p and v_n to the noiseless signals obtained due to a mitral valve source for 3 different SNR levels at receiver #s 9, 25, 41 and 57.
- (iii) The noisy signals are then filtered using a 7th order low-pass Chebyshev filter with the stop-band ripple 20 dB down and with a cut-off frequency of 1200 Hz to eliminate the high frequency contributions of the noise.
- (iv) The noisy signals are then passed through the source localization modules. Each of the source localization algorithms computes its objective function over the x - z search space for every η and velocity c as described in section (5.3).

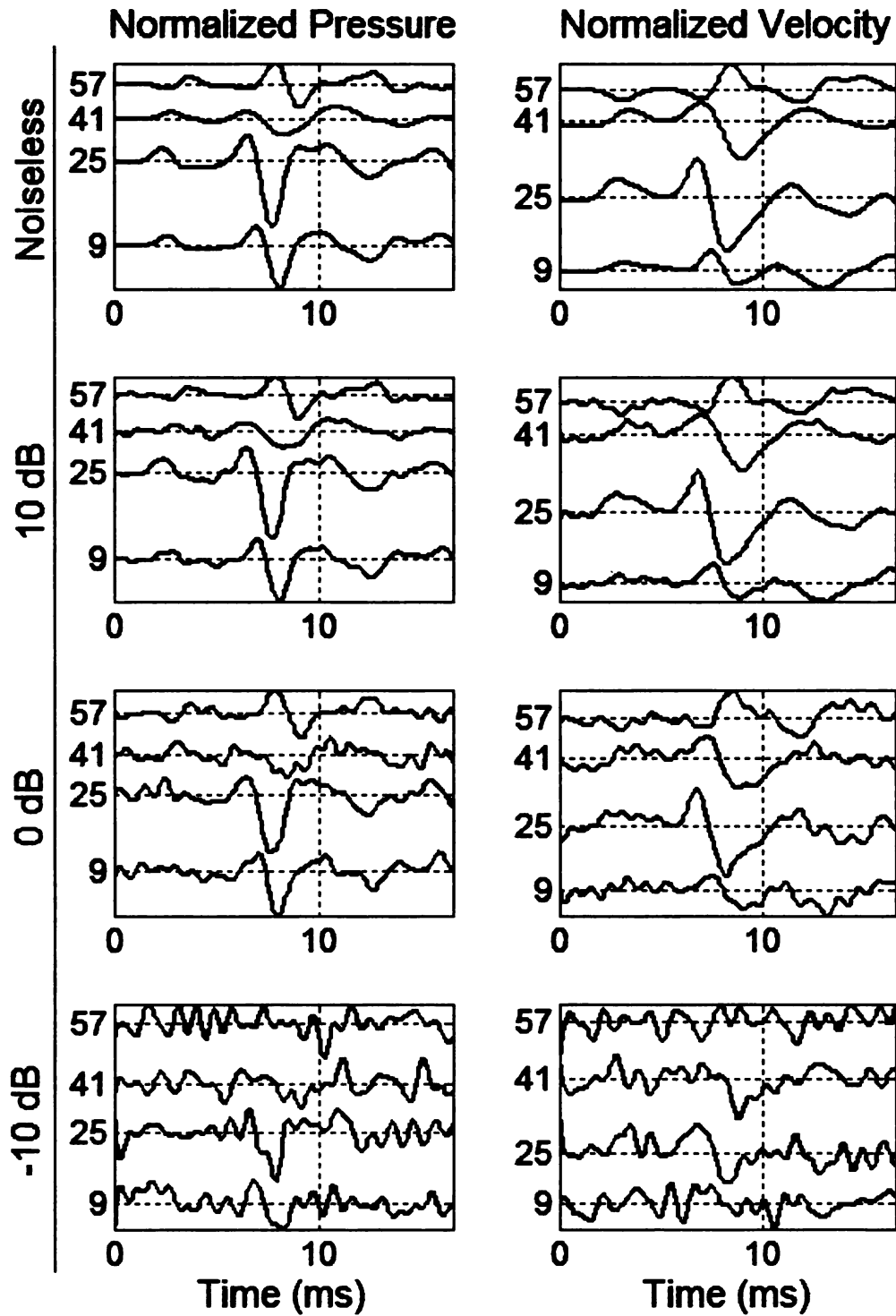


Figure 5-6 An illustration of noisy waveforms at 10 dB, 0dB and -10dB compared to the corresponding noiseless normalized pressure p and velocity v_n signals at four different receiver sites - #s 9, 25, 41 and 57

- (v) The objective function image is normalized and then smoothed using a 4 cm X 4 cm averaging filter to eliminate any noisy peaks in the function.
- (vi) The x - z location of the maximum intensity in the smoothed objective function for every η and velocity c is stored. The median x - z location across the range of velocities is used as the final estimate of the source location for each η and SNR level.
- (vii) The localization error ε , i.e. the distance between the true source location and the estimate is tabulated and plotted against the SNR values.
- (viii) The above procedure from step (iii) to (vii) is performed for both pressure p and velocity v_n signals and for every source localization algorithm.

In the following sections, the results obtained using the MUSIC algorithm on pressure p waveforms is titled as MUSIC-P while that obtained on velocity v_n waveforms is titled as MUSIC-V. Similar convention is adhered to for the remaining two localization algorithms (CFB and LCMV).

5.5 Results using the Near-Field Propagation Model based Techniques

This section presents the results of the MUSIC, CFB and LCMV algorithms employing the near-field propagation model on the simulated signals for two different source locations in the thorax. In addition, results on a homogeneous thorax are also presented for comparison.

5.5.1 Homogeneous Thorax

A homogeneous thorax with a longitudinal velocity c_p of 1605 m/s and density ρ of 1055 kg/m^3 is considered. The medium is considered shear-less and viscous-less. In other words, shear wave contributions are absent and the medium is loss-less. Figure 5-7 shows the locations of the true source and sensors used in the source localization codes.

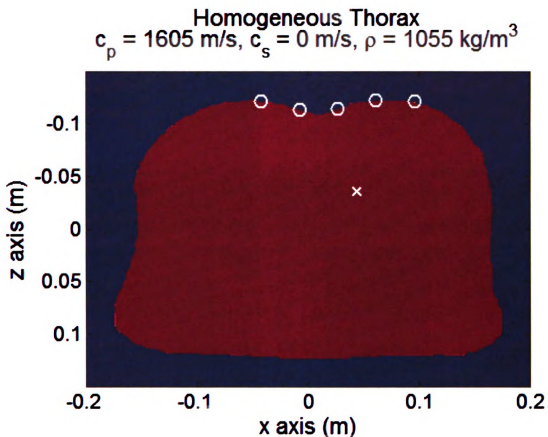


Figure 5-7 Location of the true source in the homogeneous thoracic medium is indicated by the white cross. The white circles correspond to the sensor locations used in the source localization codes.

Figure 5-8 shows the objective function images obtained for each of the source localization algorithms using a loss factor η of 0, for both pressure and velocity input signals at an SNR of 5 dB. The images in the figure also indicate the true source location by a white cross and the estimated location by a white circle. Further, the title of each image provides the localization error ϵ of the corresponding algorithm.

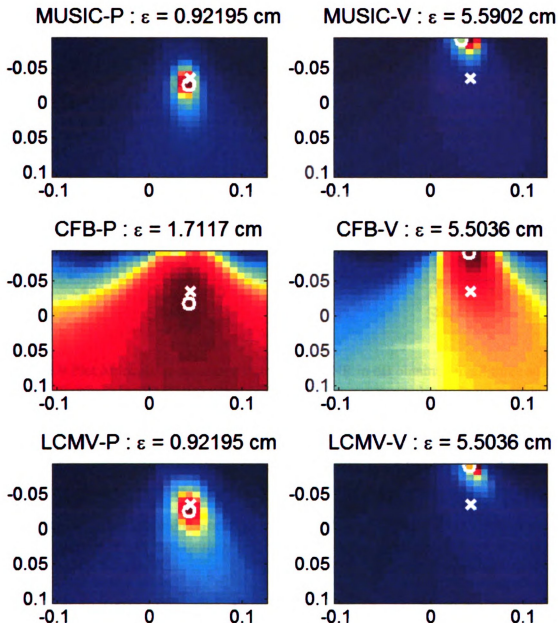


Figure 5-8 Objective function images of all three source localization algorithms using $\eta = 0$ obtained on both pressure and velocity input signals at an SNR of 5 dB in a homogeneous thoracic medium. Both x and z axes of all images are in m. White cross indicates the true source location while the white circle corresponds to the estimated source location.

The localization error ε of each of the algorithms using $\eta = 0$ is plotted against SNR in Figure 5-9 for both the pressure and velocity input signals.

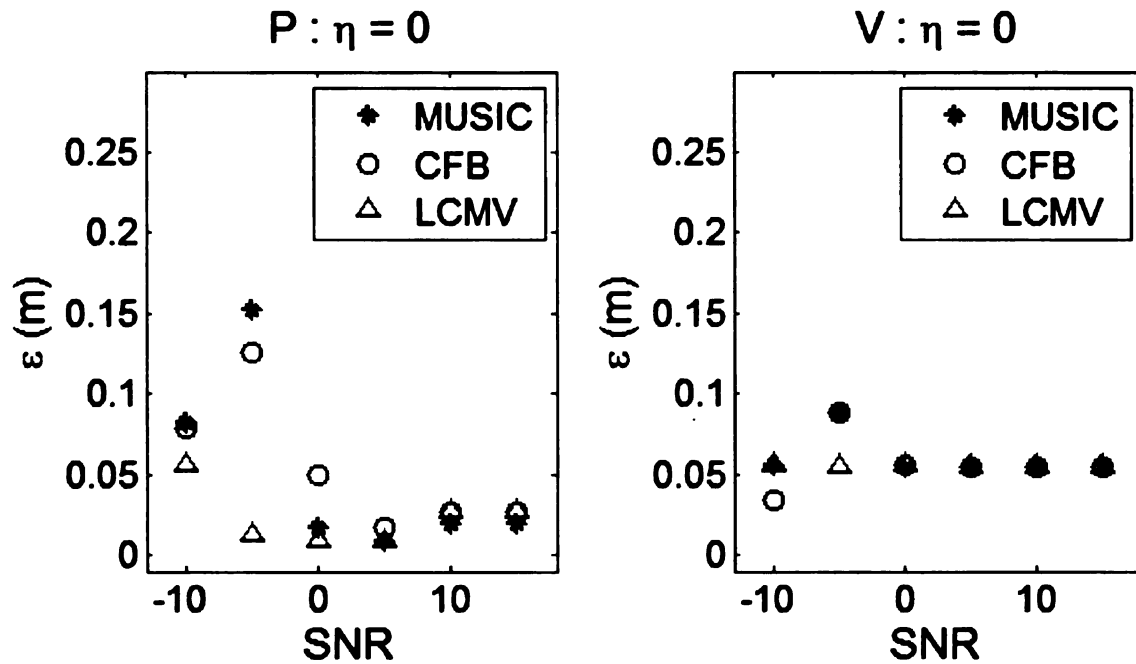


Figure 5-9 Plot of localization error ε in m versus SNR in dB obtained in all three source localization algorithms using $\eta = 0$, for both pressure and velocity input signals in a homogeneous thoracic medium.

Table 5-1 presents the same results as illustrated in Figure 5-9 in a tabulated form.

Table 5-1 Localization error ε in cm versus SNR in dB obtained in all three source localization algorithms using $\eta = 0$, for both pressure and velocity input signals in a homogeneous thoracic medium.

SNR (dB)	15	10	5	0	-5	-10
η	0	0	0	0	0	0
ε MUSIC-P (cm)	1.97	1.97	0.92	1.71	15.16	8.19
ε CFB-P (cm)	2.69	2.69	1.71	4.94	12.59	7.83
ε LCMV-P (cm)	2.69	2.69	0.92	0.92	1.22	5.59
ε MUSIC-V (cm)	5.59	5.59	5.59	5.50	8.81	5.59
ε CFB-V (cm)	5.50	5.50	5.50	5.53	8.81	3.45
ε LCMV-V (cm)	5.50	5.50	5.50	5.59	5.50	5.59

The above results indicate that the near-field model assumed by the algorithms fit the pressure signals better than the velocity signals. From Figure 5-8, it appears that although the direction of the beam-shape is fairly accurate, the range estimate obtained for the velocity signals is erred. For the pressure signals, the source location estimates are significantly accurate, MUSIC and LCMV algorithms performing the best. All the algorithms show a deterioration of performance with decrease in SNR level as expected.

5.5.2 Mitral Valve Source

A point source located at the mitral valve in the thorax is considered. Figure 5-10 shows the locations of the true source and sensors used in the source localization codes.

Figure 5-11 shows the objective function images obtained for each of the source localization algorithms using a loss factor η of 1, for both pressure and velocity input signals at an SNR of 10 dB. The images in the figure also indicate the true source location by a white cross and the estimated location by a white circle. Further, the title of each image provides the localization error ε of the corresponding algorithm.

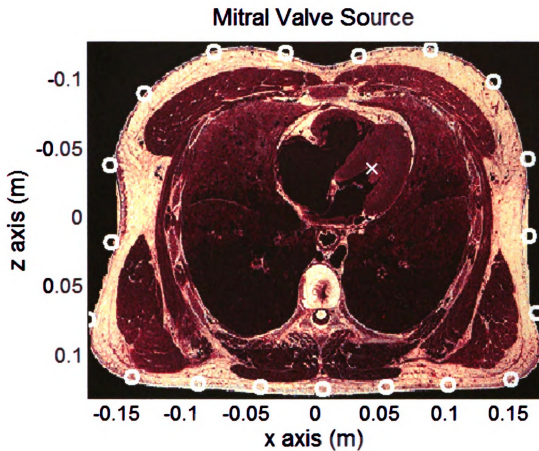


Figure 5-10 Location of the true source at the mitral valve in the thoracic medium is indicated by the white cross. The white circles correspond to the sensor locations used in the source localization codes.

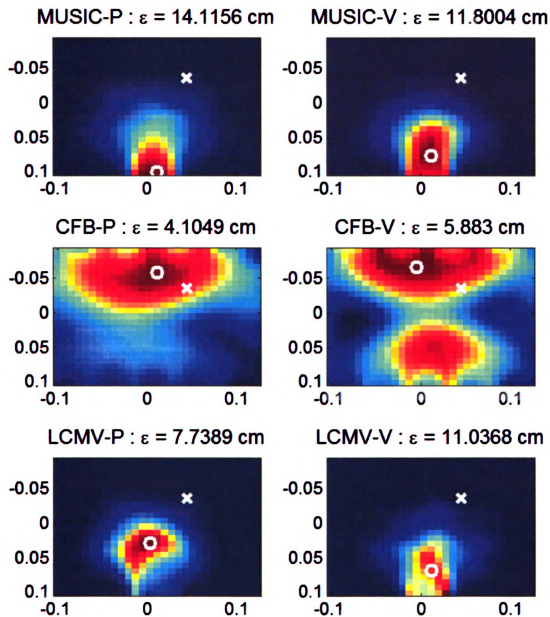


Figure 5-11 Objective function images of all three source localization algorithms using $\eta = 1$ obtained on both pressure and velocity input signals at an SNR of 10 dB for a mitral valve source. Both x and z axes of all images are in m. White cross indicates the true source location while the white circle corresponds to the estimated source location.

The localization error ε of each of the algorithms using $\eta = 0$ and $\eta = 1$ is plotted against SNR in Figure 5-12 for both the pressure and velocity input signals.

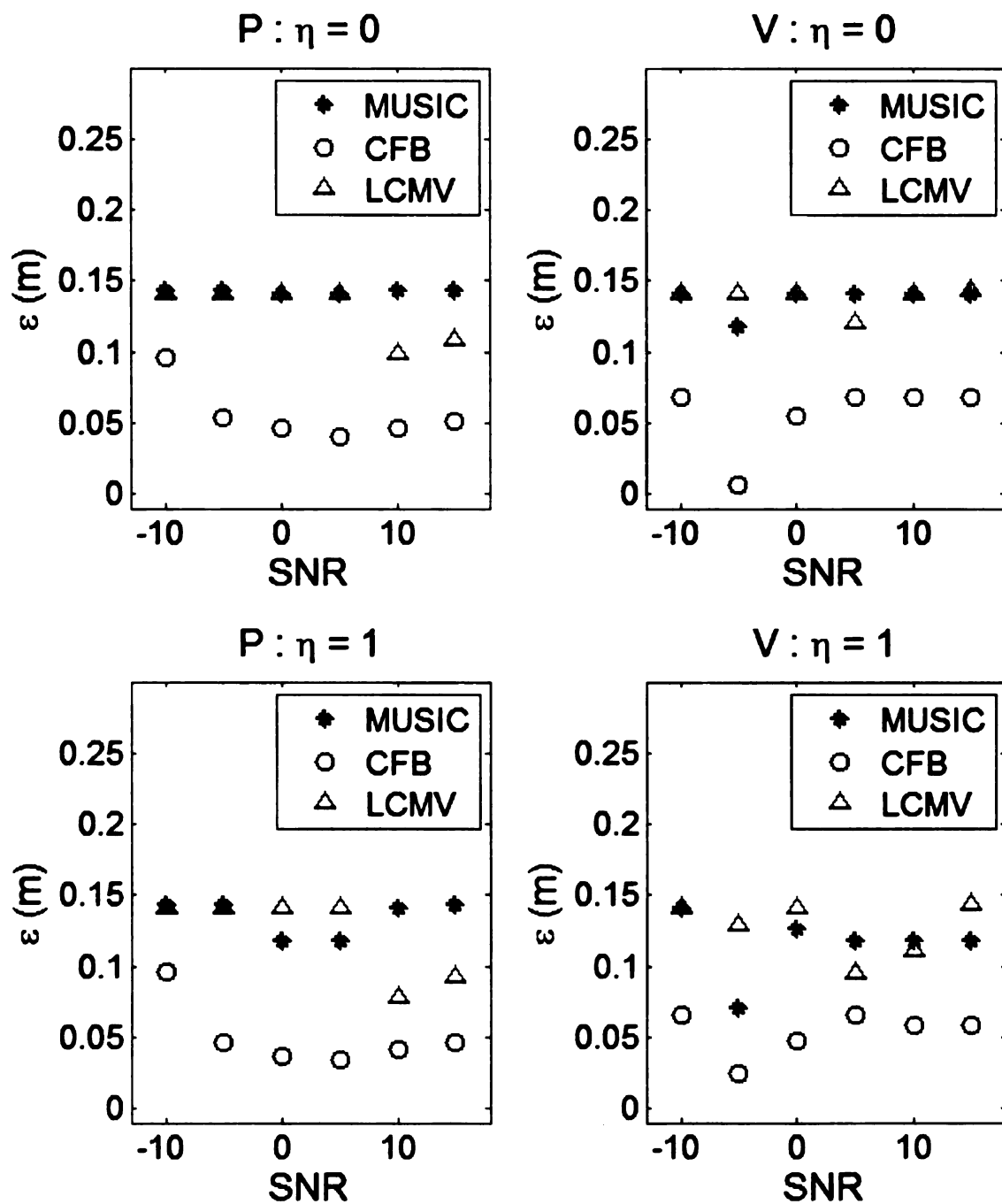


Figure 5-12 Plot of localization error ε in m versus SNR in dB obtained in all three source localization algorithms using $\eta = 0$ (top row) and $\eta = 1$ (bottom row), for both pressure and velocity input signals for a mitral valve source.

Tables 5-2 and 5-3 present the same results as illustrated in Figure 5-12 in a tabulated form.

Table 5-2 Localization error ϵ in cm versus SNR in dB obtained in all three source localization algorithms using $\eta = 0$, for both pressure and velocity input signals for a mitral valve source.

SNR (dB)	15	10	5	0	-5	-10
η	0	0	0	0	0	0
ϵ MUSIC-P (cm)	14.33	14.33	14.12	14.12	14.33	14.33
ϵ CFB-P (cm)	5.17	4.60	4.05	4.60	5.37	9.54
ϵ LCMV-P (cm)	10.82	9.84	14.12	14.12	14.12	14.12
ϵ MUSIC-V (cm)	14.12	14.12	14.12	14.12	11.80	14.12
ϵ CFB-V (cm)	6.86	6.86	6.86	5.53	0.61	6.86
ϵ LCMV-V (cm)	14.33	14.12	12.06	14.12	14.12	14.12

Table 5-3 Localization error ϵ in cm versus SNR in dB obtained in all three source localization algorithms using $\eta = 1$, for both pressure and velocity input signals for a mitral valve source.

SNR (dB)	15	10	5	0	-5	-10
η	1	1	1	1	1	1
ϵ MUSIC-P (cm)	14.33	14.12	11.80	11.80	14.33	14.33
ϵ CFB-P (cm)	4.60	4.10	3.47	3.72	4.60	9.54
ϵ LCMV-P (cm)	9.27	7.74	14.12	14.12	14.12	14.12
ϵ MUSIC-V (cm)	11.80	11.80	11.80	12.57	7.00	14.12
ϵ CFB-V (cm)	5.88	5.88	6.58	4.74	2.51	6.58
ϵ LCMV-V (cm)	14.33	11.04	9.53	14.12	12.81	14.12

The above results indicate that the near-field model assumed by the algorithms result in significantly erroneous estimates of the source locations for both the pressure and velocity signals. From Figure 5-11, it appears that neither the direction of the beam-shape

nor the range estimates are accurate. Among the three algorithms, CFB provides the best estimates, although not as accurate as desired. Also, the results appear to be marginally better for $\eta = 1$ as compared to $\eta = 0$.

5.5.3 Right Lung Source

A point source located in the right lung of the thorax is considered. Figure 5-13 shows the locations of the true source and sensors used in the source localization codes.

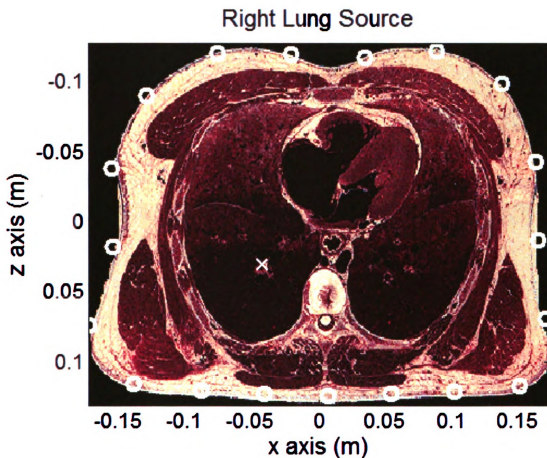


Figure 5-13 Location of the true source in the right lung of the thorax is indicated by the white cross. The white circles correspond to the sensor locations used in the source localization codes.

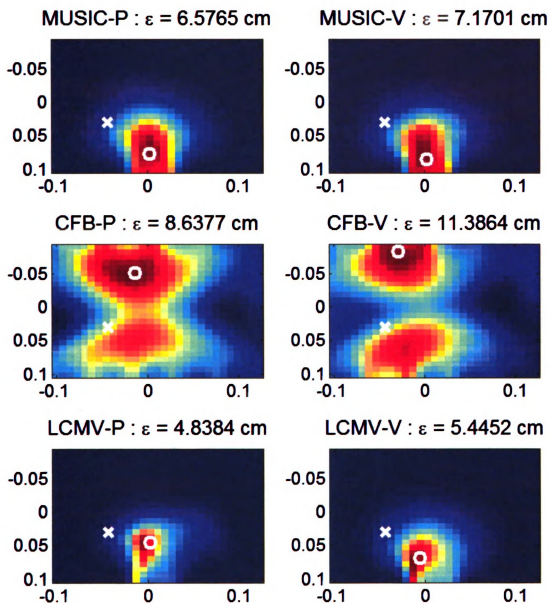


Figure 5-14 Objective function images of all three source localization algorithms using $\eta = 1$ obtained on both pressure and velocity input signals at an SNR of 10 dB for a right lung source. Both x and z axes of all images are in m. White cross indicates the true source location while the white circle corresponds to the estimated source location.

Figure 5-14 shows the objective function images obtained for each of the source localization algorithms using a loss factor η of 1, for both pressure and velocity input signals at an SNR of 10 dB. The images in the figure also indicate the true source

location by a white cross and the estimated location by a white circle. Further, the title of each image provides the localization error ε of the corresponding algorithm.

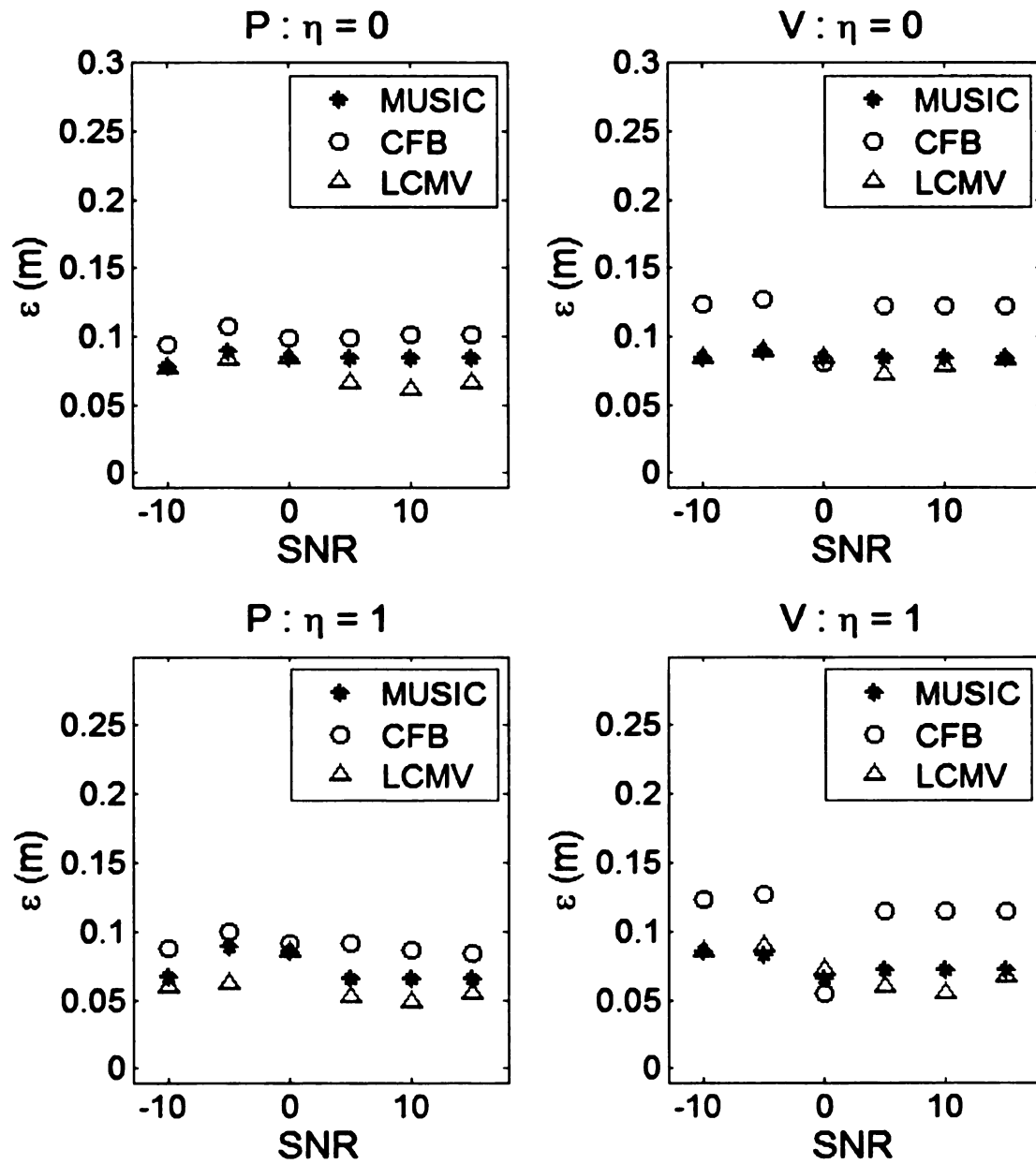


Figure 5-15 Plot of localization error ε in m versus SNR in dB obtained in all three source localization algorithms using $\eta = 0$ (top row) and $\eta = 1$ (bottom row), for both pressure and velocity input signals for a right lung source.

The localization error ε of each of the algorithms using $\eta = 0$ and $\eta = 1$ is plotted against SNR in Figure 5-15 for both the pressure and velocity input signals. Tables 5-4 and 5-5 present the same results as illustrated in Figure 5-15 in a tabulated form.

Table 5-4 Localization error ε in cm versus SNR in dB obtained in all three source localization algorithms using $\eta = 0$, for both pressure and velocity input signals for a right lung source.

SNR (dB)	15	10	5	0	-5	-10
η	0	0	0	0	0	0
ε MUSIC-P (cm)	8.46	8.46	8.46	8.46	8.92	7.78
ε CFB-P (cm)	10.15	10.15	9.95	9.95	10.74	9.44
ε LCMV-P (cm)	6.61	6.03	6.58	8.46	8.30	7.71
ε MUSIC-V (cm)	8.46	8.46	8.46	8.46	8.92	8.46
ε CFB-V (cm)	12.18	12.18	12.18	8.05	12.68	12.30
ε LCMV-V (cm)	8.30	7.80	7.16	8.46	8.92	8.46

Table 5-5 Localization error ε in cm versus SNR in dB obtained in all three source localization algorithms using $\eta = 1$, for both pressure and velocity input signals for a right lung source.

SNR (dB)	15	10	5	0	-5	-10
η	1	1	1	1	1	1
ε MUSIC-P (cm)	6.58	6.58	6.58	8.46	8.92	6.61
ε CFB-P (cm)	8.39	8.64	9.17	9.17	10.02	8.73
ε LCMV-P (cm)	5.40	4.84	5.14	8.46	6.23	5.87
ε MUSIC-V (cm)	7.17	7.17	7.17	6.58	8.30	8.46
ε CFB-V (cm)	11.39	11.39	11.39	5.45	12.68	12.30
ε LCMV-V (cm)	6.66	5.45	5.87	7.17	8.92	8.46

The above results obtained for the right lung source indicate that the source location estimates are significantly erred for both the pressure and velocity signals. Figure 5-14 shows that neither the direction of the beam-shape nor the range estimates are accurate. Among the three algorithms, LCMV provides the best estimates, although not as accurate as desired. Also, the results appear to be marginally better for $\eta = 1$ as compared to $\eta = 0$.

5.5.4 Discussion

Comparing the source localization algorithm performance for the mitral valve (and right lung) source case to the homogeneous medium case, it is clear that the heterogeneity and complexity of the thoracic medium in the former is not handled appropriately by the near-field propagation model. Also, the sensor locations used for the two cases were different, which might also contribute to the difference in the performance of the algorithms.

In order to compare their performance for the same sensor locations, the algorithms were tested on the homogeneous thoracic medium with sensor locations as illustrated in Figure 5-16, similar to that used in the mitral valve source study.

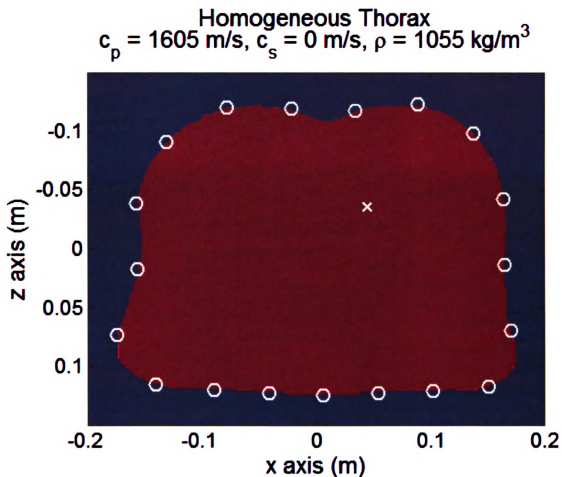


Figure 5-16 Location of the true source in the homogeneous thoracic medium is indicated by the white cross. The white circles correspond to the sensor locations used in the source localization codes.

Figure 5-17 shows the objective function images obtained for each of the source localization algorithms using a loss factor η of 0, for only the pressure signals at an SNR of 5 dB. The images in the figure also indicate the true source location by a white cross and the estimated location by a white circle. Further, the title of each image provides the localization error ε of the corresponding algorithm.

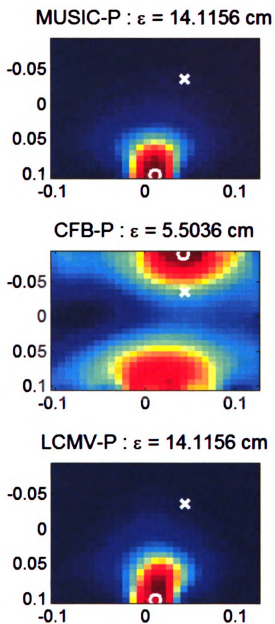


Figure 5-17 Objective function images of all three source localization algorithms using $\eta = 0$ obtained on only the pressure input signals at an SNR of 5 dB in a homogeneous thoracic medium. Both x and z axes of all images are in m. White cross indicates the true source location while the white circle corresponds to the estimated source location.

The localization error ε in cm of each of the algorithms using $\eta = 0$ is tabulated against SNR in Table 5-6 for the pressure input signals.

Table 5-6 Localization error ϵ in cm versus SNR in dB obtained in all three source localization algorithms using $\eta = 0$, for only pressure input signals in a homogeneous thoracic medium.

SNR (dB)	15	10	5	0	-5	-10
η	0	0	0	0	0	0
ϵ MUSIC-P (cm)	14.12	14.12	14.12	14.12	14.12	14.12
ϵ CFB-P (cm)	6.08	6.08	5.50	13.77	8.39	13.94
ϵ LCMV-P (cm)	14.33	14.33	14.12	14.12	14.12	14.12

The above results, at first glance, seem quite unexpected. Comparing the source location estimates for pressure signals in Tables 5-1 and 5-6, we notice that for the same homogeneous medium, a change of sensor locations has resulted in significant performance degradation. Although the directions of the beam-shapes seem to be fairly accurate in Figure 5-17, the range estimates are highly inaccurate.

This leads us to conclude that the near-field propagation model as defined in section (5.1.2) does not accurately portray the signals obtained using the FDTD codes, even for the homogeneous case. One primary reason for this discrepancy can be attributed to the source model. The near-field propagation model is in theory applicable to only a radial omni-directional point source. However, in all the FDTD simulations, the source was assumed to be an f_z directional point source.

Thus, in conclusion, two major factors that seem to impair the near-field propagation model based source localization algorithms are:

- (i) heterogeneity and viscous nature of the medium
- (ii) non-radial, non omni-directional source orientation

One of the ways to counter these two issues is to employ a true viscoelastic model of the thorax obtained via the source-to-sensor transfer functions described in Chapters 3 and 4 in sections (3.7.2) and (4.3). This approach is undertaken in the following section.

5.6 Transfer Function based Source Localization Algorithms

As mentioned in the concluding remarks of the previous section, a transfer function based model is likely to provide better results as it inherently incorporates the effects of complex inhomogeneities and viscosity of the various tissues into its model. Further, the transfer functions are obtained from simulations that employ the same source model as used in generating the sensor signals.

Four different transfer function based source localization algorithms are considered. They are briefly described in the subsections below. Each of algorithms employ the source-to-sensor transfer functions, say $h_{kl}(\omega) = [x_l(\omega) / f_{zk}(\omega)]$ in their algorithms, where k and l correspond to the source and sensor location indices, respectively, ω corresponds to the angular frequency, $x_l(\omega)$ is the Fourier spectrum of the l^{th} sensor signal and $f_{zk}(\omega)$ is the Fourier spectrum of the k^{th} f_z source function. For every source location k , the viscoelastic FDTD simulations provide the transfer functions $h_{kl}(\omega)$ for all the source-to-sensor combinations. In all 56 such simulations corresponding to 56 distinct source locations are carried out, each simulation employing $N = 19$ sensor sites, thus providing 56 x 19 transfer functions $h_{kl}(\omega)$, $k = 1, 2, \dots, 56$ and $l = 1, 2, \dots, N$. Figure 5-18 shows the locations of all the sources and sensors considered.

Source and Sensor Locations

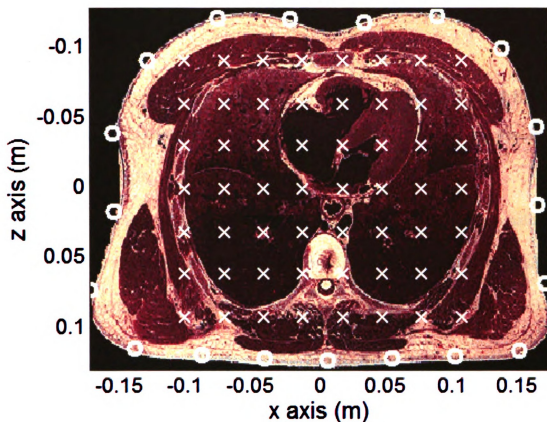


Figure 5-18 All source and sensor locations considered for the transfer functions

5.6.1 Transfer Function – Source Waveform Energy (SWE)

The name “Source Waveform Energy (SWE)” stems from the fact that this algorithm attempts to find the location that maximizes the energy of the source waveform estimate.

The source function energy estimate for one particular location k is obtained as follows:

- (i) The source function $\hat{f}_{zkl}(\omega)$ is computed using the inverse of the transfer function $h_{kl}(\omega)$ for every sensor location l as follows:

(ii)

(ii)

The

the ind

5.6.2

Th

algori

vecto

... h_k

frequ

$$\hat{f}_{zkl}(\omega) = \frac{x_l(\omega)}{h_{kl}(\omega)} \quad \forall l \quad (61)$$

- (ii) It is then filtered using a band-pass filter with cut-off frequencies of 20 Hz and 700 Hz and transformed into time domain using the inverse Fourier transform to yield $\hat{f}_{zkl}(t)$.
- (iii) Each of the l time domain source function estimates are then normalized. Finally, the median signal from the l time domain signals is computed and its energy P_k is stored as the source waveform energy for the location k .

$$P_k = \left\| \text{median}_l \frac{\hat{f}_{zkl}(t)}{\max \hat{f}_{zkl}(t)} \right\|^2 \quad (62)$$

The above procedure is repeated for all k . The source location is finally estimated as the index k that maximizes P_k .

5.6.2 Transfer Function – MUSIC

The transfer function based MUSIC algorithm is derived from the original MUSIC algorithm described in section (5.2.2). The only difference is that the near-field steering vector $a(r, \theta, \square)$ is replaced by the transfer function $\mathbf{h}_k(\omega) = [h_{k1}(\omega), h_{k2}(\omega), \dots, h_{kN}(\omega)]^T$ in objective function equation (54). Since the transfer function is in the frequency domain, the eigen vectors corresponding to the signal and noise subspace are

also computed in the frequency domain [73]. The objective function of the transfer function based MUSIC thus becomes:

$$P_k(\omega) = \frac{1}{\left\| \sum_{i=K+1}^N v_i^H(\omega) \mathbf{h}_k(\omega) \right\|^2} \quad (63)$$

where $v_i(\omega)$, $i = K+1, K+2, \dots, N$ correspond to the $(N-K)$ noise eigen vectors of the data covariance matrix computed in the frequency domain. The objective function P_k is computed only at the central frequency in the current work. However, a wideband extension involving all frequencies is trivial.

5.6.3 Transfer Function – CFB

The transfer function based CFB, popularly known as Matched Field Processing follows the same idea as explained above [22], [73], i.e. the near-field steering vector $a(r, \theta, \square)$ is replaced by the transfer function $\mathbf{h}_k(\omega) = [h_{k1}(\omega), h_{k2}(\omega), \dots, h_{kN}(\omega)]^T$ in objective function equation (56). The objective function in this case is thus given by:

$$P_k(\omega) = \mathbf{h}_k^H(\omega) \mathbf{R}(\omega) \mathbf{h}_k(\omega) \quad (64)$$

where $\mathbf{R}(\omega)$ corresponds to the data covariance matrix in the frequency domain.

5.6.4 Transfer Function – LCMV

The same ideology applies to the transfer function based LCMV algorithm too. The objective function in this case becomes:

$$P_k(\omega) = \frac{1}{\mathbf{h}_k^H(\omega) \mathbf{R}^{-1}(\omega) \mathbf{h}_k(\omega)}$$

(65)

5.7 Results using Transfer Function based Techniques

This section presents the results of the SWE, MUSIC, CFB and LCMV algorithms employing the transfer function model on the simulated signals for three different source locations in the thorax. The testing protocol is the same as explained in section (5.4) except that in this case there are no loss factor η and velocity c parameters to be optimized. The search for the intra-thoracic source location is carried out in the fixed rectangular x - z search space of $D_x \times D_z = 22.4 \text{ cm} \times 19.2 \text{ cm}$ inside the thorax as illustrated in Figure 5-3. However the spatial grid-size in this case is $3 \text{ cm} \times 3 \text{ cm}$.

5.7.1 Mitral Valve Source

A point source located at the mitral valve in the thorax is considered here as shown in Figure 5-10 in section (5.5.2). Figure 5-19 shows the objective function images obtained for each of the source localization algorithms for both pressure and velocity input signals at an SNR of 5 dB. The images in the figure also indicate the true source location by a white cross and the estimated location by a white circle. Further, the title of each image provides the localization error ϵ of the corresponding algorithm.

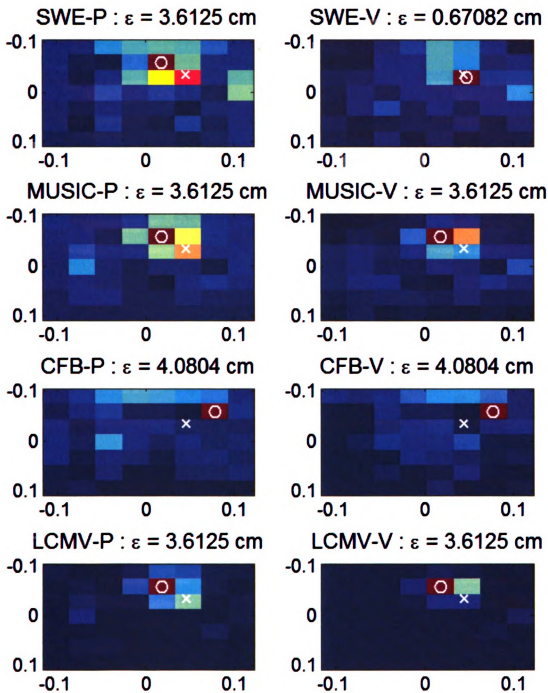


Figure 5-19 Objective function images of all four source localization algorithms obtained on both pressure and velocity input signals at an SNR of 5 dB for a mitral valve source. Both x and z axes of all images are in m. White cross indicates the true source location while the white circle corresponds to the estimated source location.

The localization error ε of each of the algorithms is plotted against SNR in Figure 5-20 for both the pressure and velocity input signals.

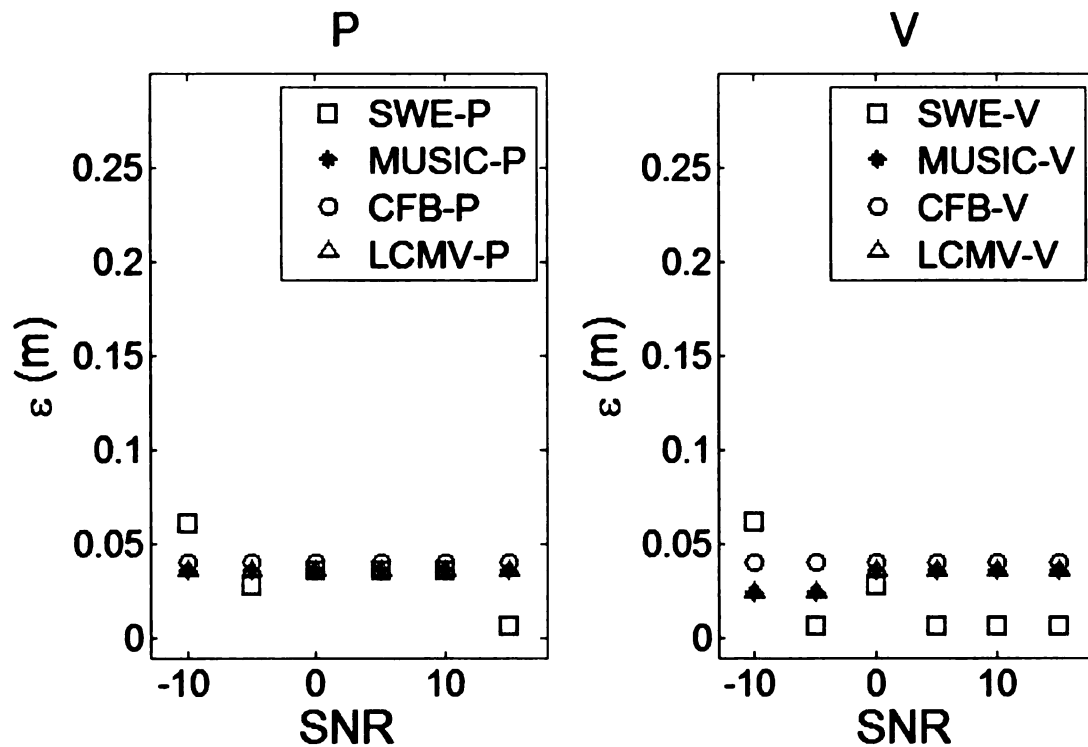


Figure 5-20 Plot of localization error ε in m versus SNR in dB obtained in all four source localization algorithms for both pressure and velocity input signals for a mitral valve source.

Table 5-7 presents the same results as illustrated in Figure 5-20 in a tabulated form.

Table 5-7 Localization error ϵ in cm versus SNR in dB obtained in all four source localization algorithms for both pressure and velocity input signals for a mitral valve source.

SNR (dB)	15	10	5	0	-5	-10
ϵ SWE-P (cm)	0.67	3.61	3.61	3.61	2.77	6.13
ϵ MUSIC-P (cm)	3.61	3.61	3.61	3.61	3.61	3.61
ϵ CFB-P (cm)	4.08	4.08	4.08	4.08	4.08	4.08
ϵ LCMV-P (cm)	3.61	3.61	3.61	3.61	3.61	3.61
ϵ SWE-V (cm)	0.67	0.67	0.67	2.77	0.67	6.18
ϵ MUSIC-V (cm)	3.61	3.61	3.61	3.61	2.42	2.42
ϵ CFB-V (cm)	4.08	4.08	4.08	4.08	4.08	4.08
ϵ LCMV-V (cm)	3.61	3.61	3.61	3.61	2.42	2.42

The above results indicate that the transfer function model employed by the algorithms result in significantly better estimates of the source locations for both the pressure and velocity signals as compared to the near-field model based techniques. From Table 5-7, it appears that the SWE algorithm provides the best source location estimates.

5.7.2 Right Lung Source

A point source located in the right lung of the thorax is considered here as shown in Figure 5-13 in section (5.5.3). Figure 5-21 shows the objective function images obtained for each of the source localization algorithms for both pressure and velocity input signals at an SNR of 10 dB. The images in the figure also indicate the true source location by a white cross and the estimated location by a white circle. Further, the title of each image provides the localization error ϵ of the corresponding algorithm.

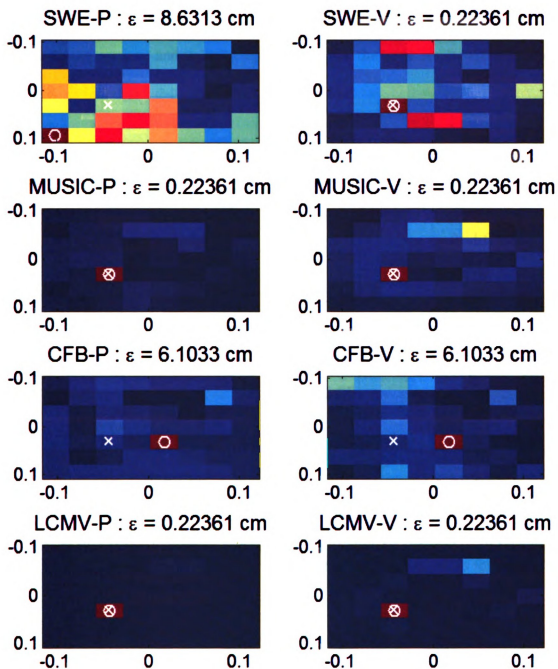


Figure 5-21 Objective function images of all four source localization algorithms obtained on both pressure and velocity input signals at an SNR of 10 dB for a right lung source. Both x and z axes of all images are in m. White cross indicates the true source location while the white circle corresponds to the estimated source location.

Th

22 for

Table

ϵ (m)

Figure

The localization error ε of each of the algorithms is plotted against SNR in Figure 5-22 for both the pressure and velocity input signals and the same results are tabulated in Table 5-8.

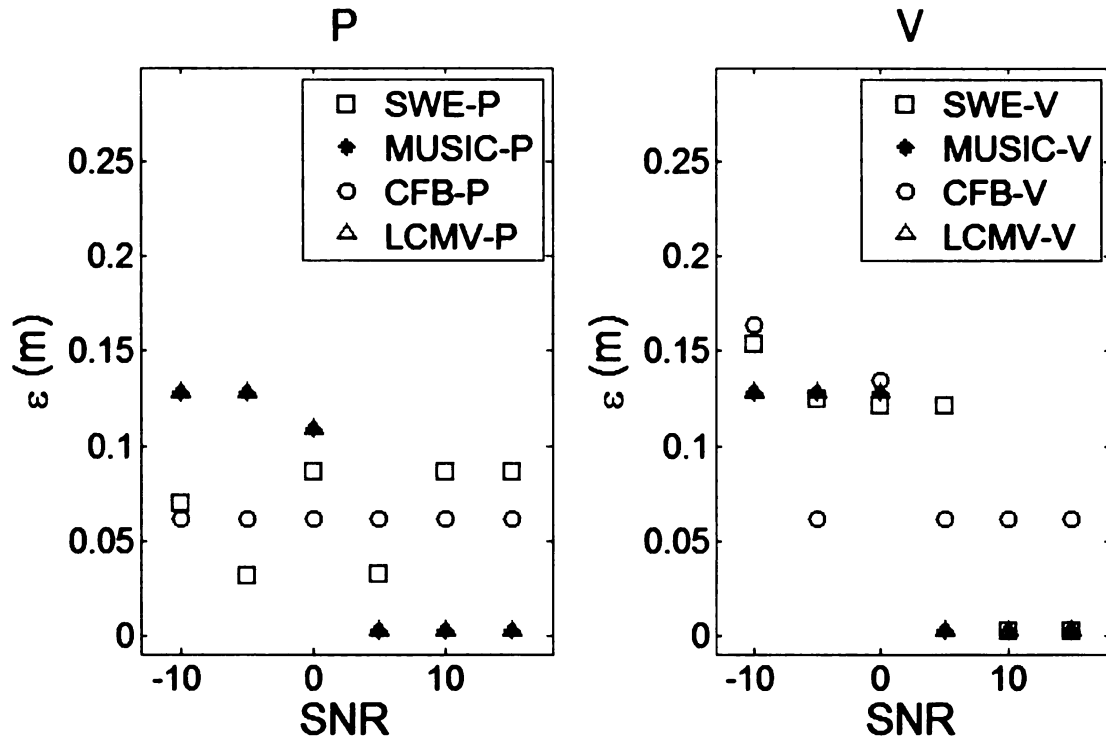


Figure 5-22 Plot of localization error ε in m versus SNR in dB obtained in all four source localization algorithms for both pressure and velocity input signals for a right lung source.

Th

algori

pressu

Table

identi

veloc

5.7.3

A

the lo

F

locali

The

Table 5-8 Localization error ϵ in cm versus SNR in dB obtained in all four source localization algorithms for both pressure and velocity input signals for a right lung source.

SNR (dB)	15	10	5	0	-5	-10
ϵ SWE-P (cm)	8.63	8.63	3.20	8.63	3.11	6.94
ϵ MUSIC-P (cm)	0.22	0.22	0.22	10.87	12.80	12.80
ϵ CFB-P (cm)	6.10	6.10	6.10	6.10	6.10	6.10
ϵ LCMV-P (cm)	0.22	0.22	0.22	10.87	12.80	12.80
ϵ SWE-V (cm)	0.22	0.22	12.10	12.10	12.49	15.38
ϵ MUSIC-V (cm)	0.22	0.22	0.22	12.80	12.80	12.80
ϵ CFB-V (cm)	6.10	6.10	6.10	13.46	6.10	16.36
ϵ LCMV-V (cm)	0.22	0.22	0.22	12.80	12.80	12.80

The above results indicate that the transfer function model employed by the algorithms result in significantly better estimates of the source locations for both the pressure and velocity signals as compared to the near-field model based techniques. From Table 5-8, it appears that the MUSIC and LCMV algorithms provide the best (and identical) source location estimates. Also, the SWE algorithms seem to fare better with velocity signals as compared to pressure signals for high SNR values.

5.7.3 Left Lung Source

A point source located in the left lung of the thorax is considered. Figure 5-23 shows the locations of the true source and sensors used in the source localization codes.

Figure 5-24 shows the objective function images obtained for each of the source localization algorithms for both pressure and velocity input signals at an SNR of 10 dB. The images in the figure also indicate the true source location by a white cross and the

estimated location by a white circle. Further, the title of each image provides the localization error ε of the corresponding algorithm.

The localization error ε of each of the algorithms is plotted against SNR in Figure 5-25 for both the pressure and velocity input signals and the same results are tabulated in Table 5-9.

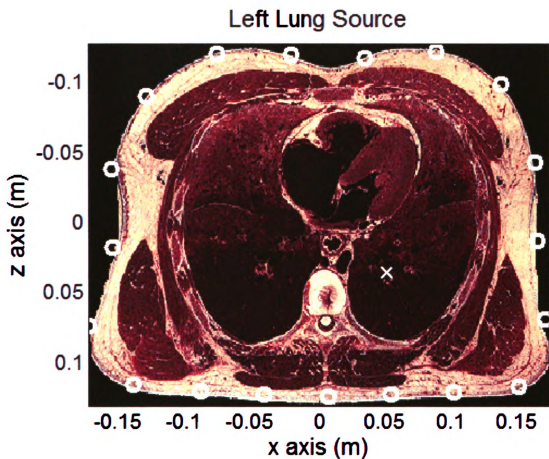


Figure 5-23 Location of the true source in the left lung of the thorax is indicated by the white cross. The white circles correspond to the sensor locations used in the source localization codes.

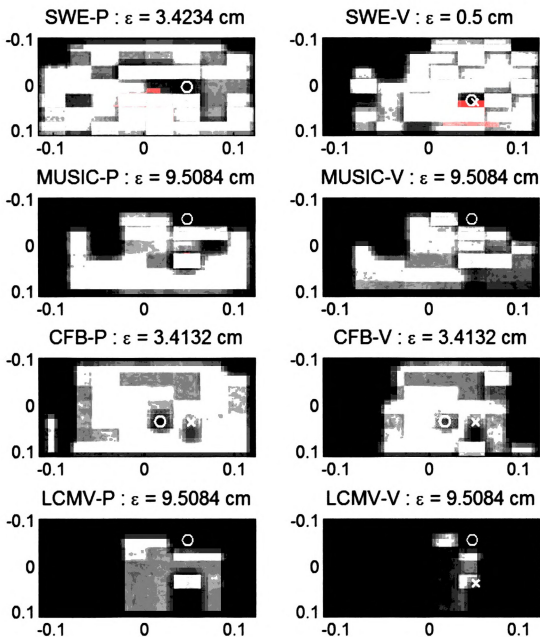


Figure 5-24 Objective function images of all four source localization algorithms obtained on both pressure and velocity input signals at an SNR of 10 dB for a left lung source. Both x and z axes of all images are in m. White cross indicates the true source location while the white circle corresponds to the estimated source location.

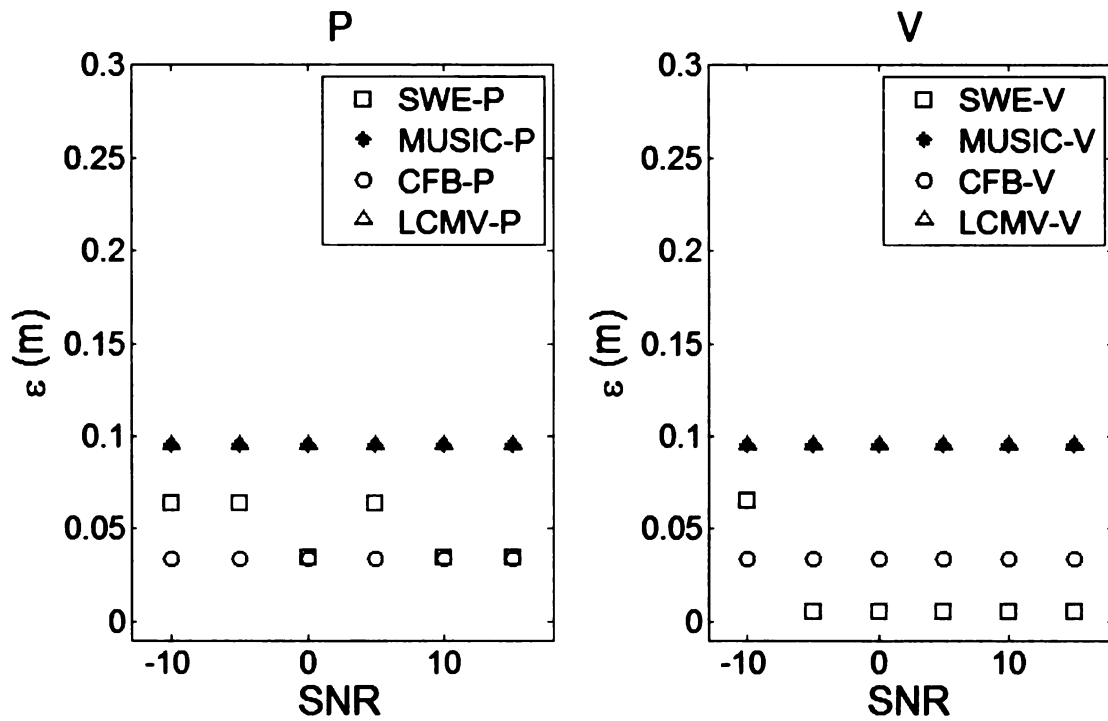


Figure 5-25 Plot of localization error ε in m versus SNR in dB obtained in all four source localization algorithms for both pressure and velocity input signals for a left lung source.

Table 5-9 Localization error ε in cm versus SNR in dB obtained in all four source localization algorithms for both pressure and velocity input signals for a left lung source.

SNR (dB)	15	10	5	0	-5	-10
ε SWE-P (cm)	3.42	3.42	6.41	3.42	6.41	6.41
ε MUSIC-P (cm)	9.51	9.51	9.51	9.51	9.51	9.51
ε CFB-P (cm)	3.41	3.41	3.41	3.41	3.41	3.41
ε LCMV-P (cm)	9.51	9.51	9.51	9.51	9.51	9.51
ε SWE-V (cm)	0.50	0.50	0.50	0.50	0.50	6.55
ε MUSIC-V (cm)	9.51	9.51	9.51	9.51	9.51	9.51
ε CFB-V (cm)	3.41	3.41	3.41	3.41	3.41	3.41
ε LCMV-V (cm)	9.51	9.51	9.51	9.51	9.51	9.51

The above results indicate that the transfer function model employed by the SWE and CFB algorithms result in good estimates of the source locations for both the pressure and velocity signals as compared to the MUSIC and LCMV algorithms. From Figure 5-24, it appears that the MUSIC and LCMV algorithms although provide inaccurate source location estimates, their objective function images show a second peak at the true source location estimate. Also, the SWE algorithms seem to fare better with velocity signals as compared to pressure signals.

5.7.4 Discussion

Overall, the transfer function based algorithms outperform the near-field based methods in all cases. This was an expected result as indicated in the beginning of section (5.6). We also notice that among the four localization algorithms considered for the transfer function based approach, the SWE algorithm using velocity signals appear to be the most consistent and accurate.

The objective function images of LCMV and MUSIC appeared to have a distinct peak in the region close to the mitral valve for all cases. In some cases, this peak was stronger than the true source peak thereby leading to an erroneous source location estimate. The additional false peak around the mitral valve region may be attributed to strong reflections coming off from that region that corrupt the contributions of the original signal waveforms from the true source. Since the LCMV and MUSIC techniques rely predominantly on the stronger eigen-vectors of the data covariance matrix, it is possible that the undesirable reflections contribute significantly towards the signal-subspace, thereby impairing the source location estimates of the algorithms. The SWE algorithm, however, by virtue of the *median* operation in its source waveform estimate

and due to the fact that it gives equal weightage to the information gained from all sensors, is not affected as long as there are enough sensors employed in the algorithm.

5.8 Methods to improve Near-Field Propagation Model based Techniques

As mentioned in the concluding sections of section (5.5), the non omni-directional source orientation could be one of the potential reasons for impairing performance of the near-field propagation model based source localization algorithms. In order to tackle this problem, this section proposes a method to incorporate an approximate “ f_z directional source” behavior into the near-field propagation model. Preliminary results supporting this proposed scheme are also provided.

5.8.1 Distributed Source Model

The idea of employing a distributed source model for beamforming applications has been studied in the past [74], [75]. The ability to model any source orientation using a distributed set of point omni-directional sources can be exploited to yield better source localization results. In the current work, we propose to model the f_z directional source using a vertical strip of a few, say Q , closely spaced omnidirectional point sources as shown in Figure 5-26. Thus, the near-field propagation model is now governed by steering vectors associated with each of these Q omnidirectional point sources.

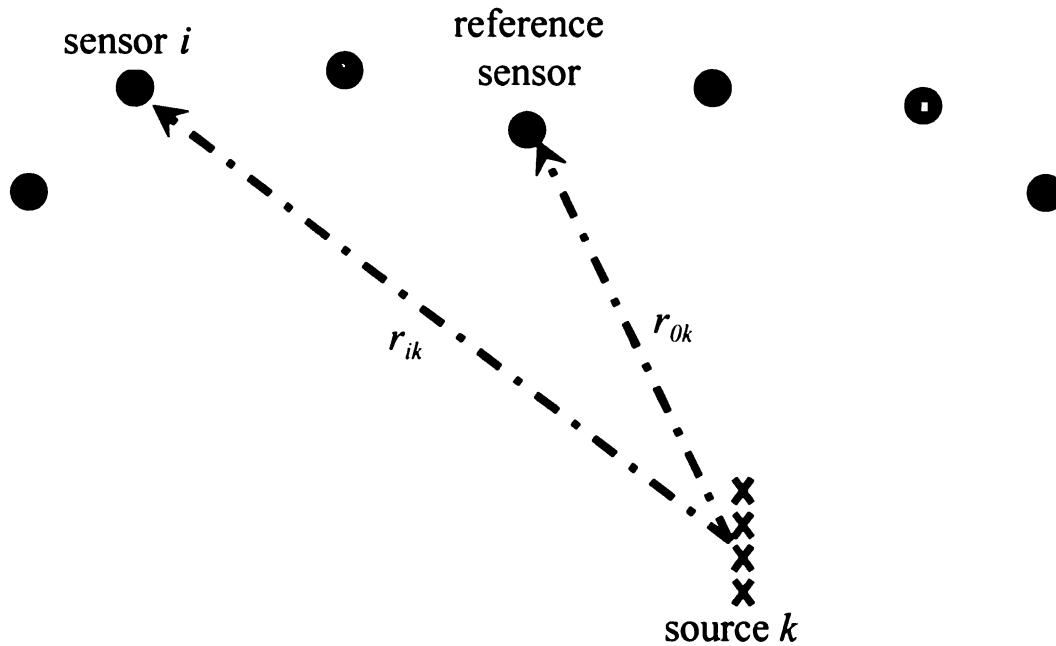


Figure 5-26 Distributed source model

The above scheme is incorporated into each of the near-field propagation model algorithms. Preliminary results are presented in the subsection below.

5.8.2 Preliminary results using Distributed Source Model Techniques

The MUSIC, CFB and LCMV algorithms used the distributed source model as explained above assuming $Q = 5$. Results obtained on the homogeneous thoracic medium and for a mitral valve source are presented below.

5.8.2.1 Homogeneous Thorax

In order to compare the performance of the proposed scheme, the algorithms were tested on the same homogeneous thoracic medium with sensor locations as illustrated in Figure 5-16.

Figure 5-27 shows the objective function images obtained for each of the distributed source based localization algorithms using a loss factor η of 0, for both pressure and velocity input signals at an SNR of 5 dB. The images in the figure also indicate the true source location by a white cross and the estimated location by a black diamond. Further, the title of each image provides the localization error ε of the corresponding algorithm.

The localization error ε of each of the algorithms is plotted against SNR in Figure 5-28 for both the pressure and velocity input signals and the same results are tabulated in Table 5-10.

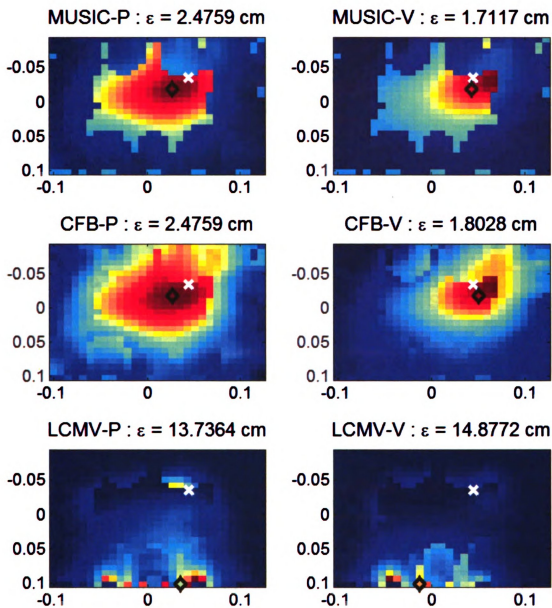


Figure 5-27 Objective function images of all three distributed source based algorithms using $\eta = 0$ obtained on both pressure and velocity input signals at an SNR of 5 dB in a homogeneous thoracic medium. Both x and z axes of all images are in m. White cross indicates the true source location while the black diamond corresponds to the estimated source location.

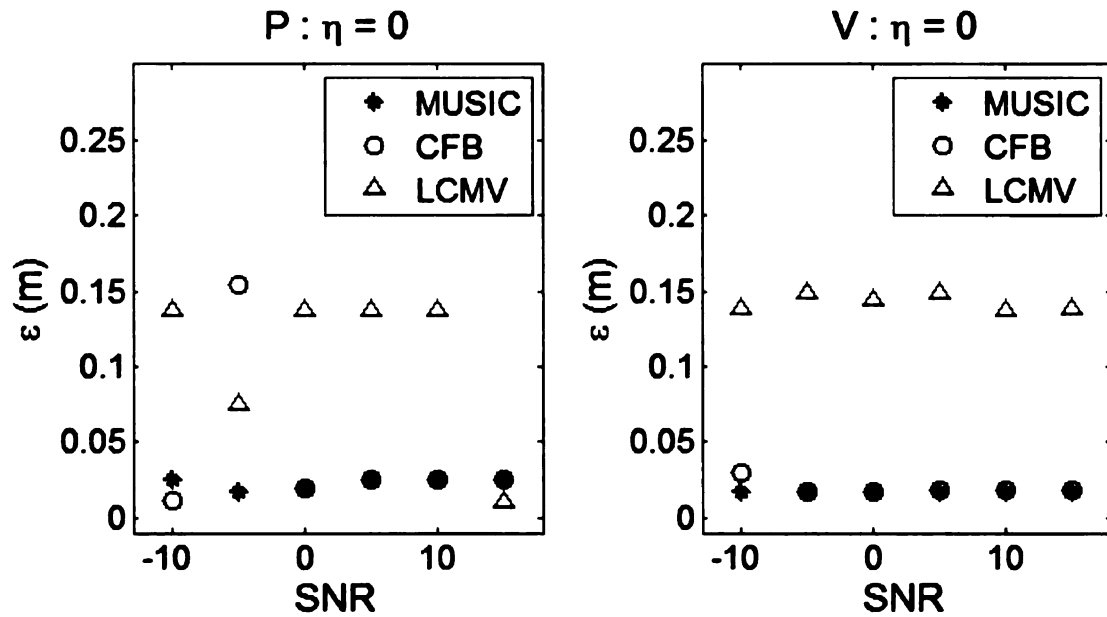


Figure 5-28 Plot of localization error ε in m versus SNR in dB obtained in all distributed source based algorithms using $\eta = 0$, for both pressure and velocity input signals in a homogeneous thoracic medium.

Table 5-10 Localization error ε in cm versus SNR in dB obtained in all distributed source based algorithms using $\eta = 0$, for both pressure and velocity input signals in a homogeneous thoracic medium.

SNR (dB)	15	10	5	0	-5	-10
η	0	0	0	0	0	0
ε MUSIC-P (cm)	2.48	2.48	2.48	1.97	1.71	2.48
ε CFB-P (cm)	2.48	2.48	2.48	1.97	15.38	1.08
ε LCMV-P (cm)	1.01	13.74	13.74	13.74	7.52	13.74
ε MUSIC-V (cm)	1.71	1.71	1.71	1.71	1.71	1.71
ε CFB-V (cm)	1.80	1.80	1.80	1.71	1.71	3.00
ε LCMV-V (cm)	13.82	13.74	14.88	14.33	14.88	13.82

The above results in Table 5-10 when compared to those obtained by the near-field single-source model in Table 5-6 shows a dramatic improvement, especially for the MUSIC and CFB algorithms.

5.8.2.2 Mitral Valve Source

The point source located at the mitral valve location as discussed in section (5.5.2) is considered here. Figure 5-29 shows the objective function images obtained for each of the distributed source based localization algorithms using a loss factor η of 0, for both pressure and velocity input signals at an SNR of 5 dB. The images in the figure also indicate the true source location by a white cross and the estimated location by a black diamond. Further, the title of each image provides the localization error ε of the corresponding algorithm.

The localization error ε of each of the algorithms is plotted against SNR in Figure 5-30 for both the pressure and velocity input signals and the same results are tabulated in Tables 5-11 and 5-12.

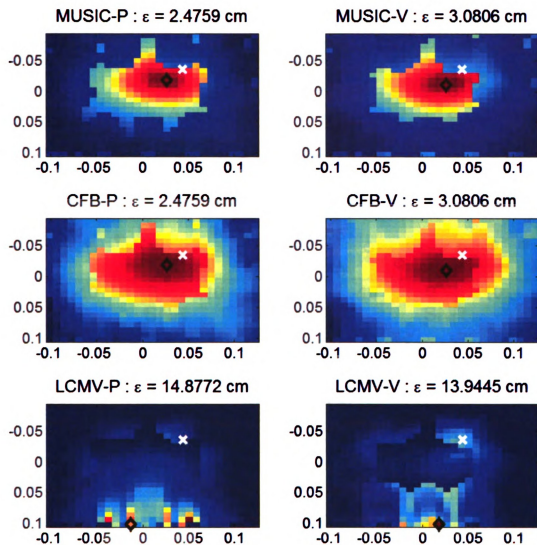


Figure 5-29 Objective function images of all distributed source based algorithms using $\eta = 0$ obtained on both pressure and velocity input signals at an SNR of 5 dB for a mitral valve source. Both x and z axes of all images are in m. White cross indicates the true source location while the black diamond corresponds to the estimated source location.

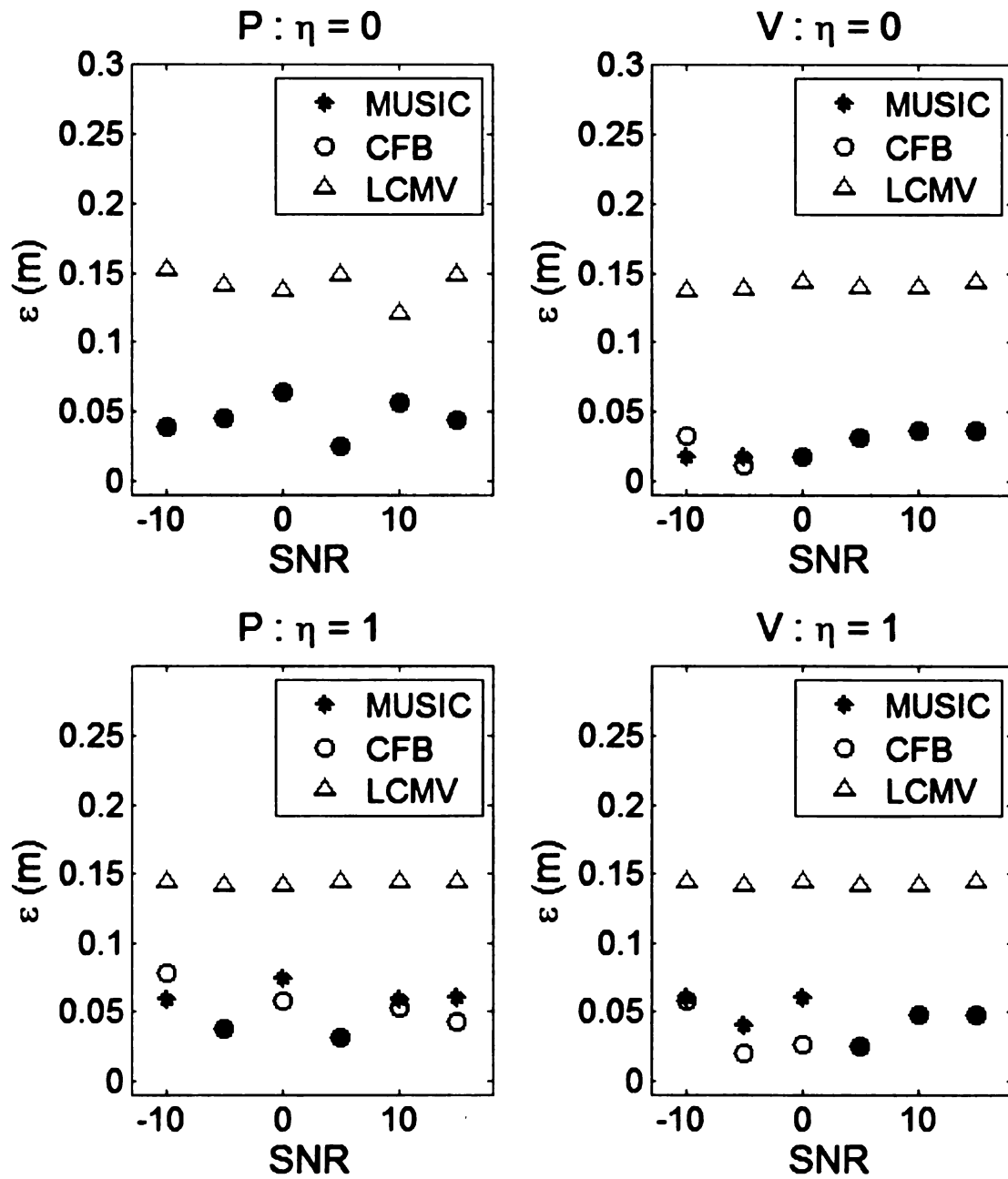


Figure 5-30 Plot of localization error ε in m versus SNR in dB obtained in all distributed source based algorithms using $\eta = 0$ (top row) and $\eta = 1$ (bottom row), for both pressure and velocity input signals for a mitral valve source.

Table 5-11 Localization error ε in cm versus SNR in dB obtained in all distributed source based algorithms using $\eta = 0$, for both pressure and velocity input signals for a mitral valve source.

SNR (dB)	15	10	5	0	-5	-10
η	0	0	0	0	0	0
ε MUSIC-P (cm)	4.30	5.59	2.48	6.32	4.53	3.80
ε CFB-P (cm)	4.30	5.59	2.48	6.32	4.53	3.80
ε LCMV-P (cm)	14.88	12.06	14.88	13.74	14.12	15.21
ε MUSIC-V (cm)	3.61	3.61	3.08	1.71	1.71	1.71
ε CFB-V (cm)	3.61	3.61	3.08	1.71	1.08	3.26
ε LCMV-V (cm)	14.33	13.94	13.94	14.33	13.82	13.74

Table 5-12 Localization error ε in cm versus SNR in dB obtained in all distributed source based algorithms using $\eta = 1$, for both pressure and velocity input signals for a mitral valve source.

SNR (dB)	15	10	5	0	-5	-10
η	1	1	1	1	1	1
ε MUSIC-P (cm)	6.08	5.88	3.08	7.43	3.76	5.88
ε CFB-P (cm)	4.20	5.28	3.08	5.80	3.76	7.77
ε LCMV-P (cm)	14.33	14.33	14.33	14.12	14.12	14.33
ε MUSIC-V (cm)	4.74	4.74	2.51	6.08	4.05	6.08
ε CFB-V (cm)	4.74	4.74	2.51	2.57	2.01	5.79
ε LCMV-V (cm)	14.33	14.12	14.12	14.33	14.12	14.33

The results obtained for the distributed source based model in Table 5-11 and Table 5-12 when compared to those obtained using the near-field single-source model in Tables 5-2 and 5-3 appear to have improved significantly for the MUSIC and CFB algorithms.

5.9 Conclusion

From all the source localization studies conducted in the above sections, it is clear that model-based techniques can yield improved results when the model matches the true conditions. The near-field propagation model, being based on an omnidirectional point source in a homogeneous medium, does not perform well to localize the intra-thoracic acoustic sources that were generated using an f_z directional source. The transfer-function based approach, being based on the true viscoelastic forward model, is able to provide very accurate results. However, further studies need to be conducted to assess their performance in cases of model-mismatch. The distributed source model approach provides a scheme to improve the performance of the near-field propagation model and may be used in absence of a transfer function model.

CHAPTER 6

SUMMARY AND CONCLUSIONS

6.1 Summary

A 2D finite difference time domain viscoelastic model of the human thorax has been developed that facilitates the study of sound propagation in the thorax. The model employs the true human anatomical geometry and accurate estimates of the material properties of all the tissue structures in the thorax. It thus tracks both the shear and longitudinal waves and all the associated mode conversions that occur at the various tissues interfaces in the thorax. The FDTD codes are validated for a simple geometry by comparing the simulation results to the analytical solutions and to results obtained in a previously published work. Simulations illustrating the sound propagation from the mitral valve location to the surface of the thorax are presented. The acoustic source-to-receiver transfer functions corresponding to the various auscultation sites on the thorax are briefly analyzed. Further, the effects of rib structures, shear elasticity of tissues and dimensions of the thorax on the sound waves are also studied.

The FDTD viscoelastic model has also been used to study the lung sound propagation in the human thoracic cavity under pneumothorax conditions. By simulating varying degrees of severity of the disease, the model assists in determining the key frequency bands that contain the most information to aid in diagnosis. The work thus lends itself for development of advanced auscultatory techniques for detection of pneumothorax using noninvasive acoustic sensors.

Finally, three different source localization algorithms based on the traditional near-field propagation model are studied and implemented. The localizing ability of these algorithms to detect an intra-thoracic source are assessed and compared. In addition, four methods based on a transfer-function approach are proposed to alleviate the issues of the near-field propagation model based techniques. The results of the transfer function based algorithms are compared to those obtained by the near-field model to demonstrate the improved localizing ability of the former. Further, one more strategy employing a distributed source model is proposed to counter one of the issues of the near-field propagation model. Results demonstrating the performance improvement are presented.

6.2 Conclusions and Future Work

The 2D model in the present state may be used to simulate and study the various auscultation sounds associated with certain diseased conditions of the heart or lungs, like pneumothorax, and thereby provide a limited understanding of the following:

- optimal auscultation sites that contain significant diagnostic information
- relation of the sensor signals to the extent and location of the damaged tissue or the diseased state
- type of multi-sensor algorithms that might be suitable for localizing the pathological sites in the thorax
- variations in sensor signals that can be attributed to changes in the torso geometry

Future efforts could be directed towards developing a 3D model of the torso that would provide a more accurate representation of these thoracic sounds. In addition, source localization techniques to localize multiple sources in the thoracic cavity and methods to estimate the source waveforms could also be considered.

The 2D viscoelastic FDTD model needs to be extended to a 3D model for it to be used as an advanced diagnostic tool. In addition, incorporation of appropriate sound-generation models to account for the various intra-thoracic sound sources would add immense value to the FDTD models, thereby allowing it to be used to design various array processing and inversion schemes for diagnosis of various thoracic pathologies.

REFERENCES

REFERENCES

- [1] H. Pasterkamp, S. S. Kraman, and G. R. Wodicka, "Respiratory sounds - Advances beyond the stethoscope," *Am. J. Respir. Crit. Care Med.* **156**(3), 974-987 (1997).
- [2] A. Sarvazyan, "Audible-frequency medical diagnostic methods: Past, present and future," *J. Acoust. Soc. Am.* **117**, 2586 (2005).
- [3] Y. Bahadirlar and H. Ö. Gülçür, "Cardiac passive acoustic localization: CARDIOPAL," *Elektrik, Turkish J. of Electrical Engineering & Computer Science* **6**(3), 243-259 (1998).
- [4] N. L. Owsley and A. J. Hull, "Beamformed nearfield imaging of a simulated coronary artery containing a stenosis," *IEEE Trans. Medical Imaging* **17**(6), 900-909 (1998).
- [5] T. J. Royston, X. Zhang, H. A. Mansy, and R. H. Sandler, "Modeling sound transmission through the pulmonary system and chest with application to diagnosis of a collapsed lung," *J. Acoust. Soc. Am.* **111**, 1931-1946 (2002).
- [6] H. Banks and N. Luke, "Modeling of propagating shear waves in biotissue employing an internal variable approach to dissipation," CRSC Tech. Report, NCSU (February 2007).
- [7] R. Zalter, H. C. Hardy, and A. A. Luisada, "Acoustic transmission characteristics of the thorax," *J. Appl. Physiol* **18**(2), 428-436 (1963).
- [8] J. J. Faber, "Damping of sound on the chest surface," *Circulation Res.* **13**, 352-358 (1963).
- [9] L. G. Durand, J. Genest, and R. Guardo, "Modeling of the transfer function of the heart-thorax acoustic system in dogs," *IEEE Trans. Biomed. Eng.* **BME-32**(8), 592-601 (1985).
- [10] J. Verburg, "Transmission of vibrations of the heart to the chestwall," *Adv. Cardiovasc. Phys.* **5**(III), 84-103 (1983).
- [11] G. R. Wodicka, K. N. Stevens, and D. C. Shannon, "A theoretical model of sound transmission in the thorax," *Proceedings of the Annual Int. Conf. of the IEEE Engineering in Engineering in Medicine and Biology Society*, Vol. 1, 248-249 (1989).
- [12] G. Wodicka, K. Stevens, H. Golub, E. Cravalho, and D. Shannon, "A model of acoustic transmission in the respiratory system," *IEEE Trans. Biomed. Eng.* **36**, 925-934 (1989).

- [13] G. R. Wodicka, A. Aguirre, P. D. DeFrain, and D. C. Shannon, "Phase delay of pulmonary acoustic transmission from trachea to chest wall," *IEEE Trans. Biomed. Eng.* **39**(10), 1053-1059 (1992).
- [14] G. R. Wodicka, P. D. DeFrain, and S. S. Kraman, "Bilateral asymmetry of respiratory acoustic transmission," *Med. Biol. Eng. Comput.* **32**(5), 489-494 (1994).
- [15] S. Lu, P. Doerschuk, and G. Wodicka, "Parametric phase-delay estimation of sound transmitted through intact human lung," *Med. Biol. Eng. Comput.* **33**(3), 293-298 (1995).
- [16] I. V. Vovk, V. T. Grinchenko, and V. N. Oliynik, "Modeling the acoustic properties of the chest and measuring breath sounds," *Acoust. Phys.* **41**, 667-676 (1995).
- [17] I. V. Vovk, V. T. Grinchenko, and V. N. Oliynik, "Measurement of breath noise from the surface of human thorax," *Proceedings of the IEEE Instrumentation and Measurement Technology Conference*, Vol. 2, 1330-1335 (1996).
- [18] H. Vermarien and E. van Vollenhoven, "The Recording of Heart Vibrations: A Problem of Vibration Measurement on Soft Tissue," *Med. Biol. Eng. Comput.* **22**, 168-178 (1984).
- [19] A. H. Leung and S. Sehati, "Sound transmission through normal and diseased human lungs," *Engineering Science and Education Journal* **5**(1), 25-31 (1996)
- [20] Q. Grimal, A. Watzky, and S. Naili, "A one-dimensional model for the propagation of transient pressure waves through the lung," *J. Biomechanics* **35**(8), 1081-1089 (2002).
- [21] T. J. Royston, Y. Yazicioglu, and F. Loth, "Surface response of a viscoelastic medium to subsurface acoustic sources with application to medical diagnosis," *J. Acoust. Soc. Am.* **113**, 1109-1121 (2003).
- [22] M. B. Ozer, S. Acikgoz, T. J. Royston, H. A. Mansy, and R. H. Sandler, "Boundary element model for simulating sound propagation and source localization within the lungs," *J. Acoust. Soc. Am.* **122**(1), 657-671 (2007).
- [23] C. Narasimhan, R. Ward, K. L. Kruse, M. Guddati, and G. Mahinthakumar, "A high resolution computer model for sound propagation in the human thorax based on the Visible Human data set," *Computers in Biology and Medicine* **34**(2), 177-192 (2004).
- [24] H. T. Banks and N. S. Luke, "Modeling of propagating shear waves in biotissue employing an internal variable approach to dissipation," *Communications in Computational Physics* **3**(3), 603-640 (2008).
- [25] Y. C. Fung, *Biomechanics: Mechanical Properties of Living Tissues* (Springer-Verlag, New York, 1993).

- [26] M. Cozic, L. G. Durand, and R. Guardo, "Development of a cardiac acoustic mapping system," *Proceedings of the 17th International Conference of the IEEE Engineering in Medicine and Biology Society*, Vol. 2, 1029-1030 (1995).
- [27] James V. Candy, "Model-based signal processing in acoustics: An overview," *J. Acoust. Soc. Am.* **101**(5), 3155 (1997).
- [28] Y. Bahadirlar and H. O. Gulcur, "Time-frequency cardiac passive acoustic localization," *Proceedings of the 23rd Annual International Conference of the IEEE Engineering in Medicine and Biology Society*, Vol. 2, 1850-1853 (2001).
- [29] M. Kompis and G. R. Wodicka, "Spatial information in simultaneous multimicrophone recordings of thoracic sounds," *J. Acoust. Soc. Am.* **99**(4), 2478-2500 (1996).
- [30] M. Kompis, H. Pasterkamp, Y. Motai, and G. R. Wodicka, "Spatial representation of thoracic sounds," *Proceedings of the 20th Annual International Conference of the IEEE Engineering in Medicine and Biology Society*, Vol. 3, 1661-1664 (1998).
- [31] M. Kompis, H. Pasterkamp, and G. R. Wodicka, "Acoustic imaging of the human chest," *Chest* **120**, 1309-1321 (2001).
- [32] N. Owsley, "Passive Acoustic Array Processing of Heart Sounds," First IEEE Sensor Array and Multichannel Signal Processing Workshop (2000).
- [33] A. M. McKee and R. A. Goubran, "Sound Localization in the Human Thorax," *Proceedings of the IEEE Instrumentation and Measurement Technology Conference*, Vol. 1, 117-122 (2005).
- [34] A. M. McKee and R. A. Goubran, "Chest sound pick-up using a multisensor array," *Proceedings of IEEE Conference on Sensors*, 780-783 (2005).
- [35] John Semmlow and Ketaki Rahalkar, "Acoustic Detection of Coronary Artery Disease," *Annual Review of Biomedical Engineering* **9**, 449-469 (2007).
- [36] L. E. Kinsler and A. R. Frey, *Fundamentals of acoustics* (Wiley, New York, 3rd edition, 1982).
- [37] B. A. Auld, *Acoustic fields and elastic waves in solids* (John Wiley & Sons, Inc., 1973).
- [38] H. L. Oestreicher, "Field and impedance of an oscillating sphere in a viscoelastic medium with an application to biophysics," *J. Acoust. Soc. Am.* **23**, 707-714 (1951).
- [39] A. Hosokawa, "Ultrasonic pulse waves in cancellous bone analyzed by finite-difference time-domain methods," *Ultrasonics* **44**(1), e227-e231 (2006).

- [40] Visible Human Project, www.nlm.nih.gov/research/visible/visible_human.html (date last viewed 1/9/09).
- [41] A Guided Tour of the Visible Human, www.madsci.org/~lynn/VH/tour.html (date last viewed 06/03/09), MAD Scientist Network, Washington University Medical School (1996).
- [42] M. Otani, T. Hirahara, S. Shimizu, and S. Adachi, "Numerical simulation of transfer and attenuation characteristics of soft-tissue conducted sound originating from vocal tract," *Applied Acoustics* **70**(3), 469-472 (2009).
- [43] T. D. Mast, L. M. Hinkelman, L. A. Metlay, M. J. Orr, and R. C. Waag, "Simulation of ultrasonic pulse propagation, distortion, and attenuation in the human chest wall," *J. Acoust. Soc. Am.* **106**(6), 3665-3677 (1999).
- [44] A. Kemper, C. McNally, E. Kennedy, S. Manoogian, A. Rath, T. Ng, J. Stitzel, E. Smith, S. Duma, and F. Matsuoka, "Material Properties of Human Rib Cortical Bone from Dynamic Tension Coupon Testing," *Stapp Car Crash Journal* **49**, 199-230 (2005).
- [45] A. Hosokawa, "Simulation of ultrasound propagation through bovine cancellous bone using elastic and Biot's finite-difference time-domain methods," *J. Acoust. Soc. Am.* **118**, 1782-1789 (2005).
- [46] T. D. Mast, "Empirical relationships between acoustic parameters in human soft tissues," *Acoustics Research Letters Online* **1**, 37-42 (2000).
- [47] M. Fatemi, A. Manduca, and J. F. Greenleaf, "Imaging elastic properties of biological tissues by low-frequency harmonic vibration," *Proceedings of the IEEE*, Vol. **91**(10), 1503-1519 (2003).
- [48] X. Zhang, T. J. Royston, H. A. Mansy, and R. H. Sandler, "Radiation impedance of a finite circular piston on a viscoelastic half-space with application to medical diagnosis," *J. Acoust. Soc. Am.* **109**, 795-802 (2001).
- [49] K. Hoyt, T. Kneezel, B. Castaneda, and K. J. Parker, "Quantitative sonoelastography for the in vivo assessment of skeletal muscle viscoelasticity," *Phys. Med. Biol.* **53**, 4063-4080 (2008).
- [50] E. L. Madsen, H. J. Sathoff, and J. A. Zagzebski, "Ultrasonic shear wave properties of soft tissues and tissuelike materials," *J. Acoust. Soc. Am.* **74**(5), 1346-1355 (1983).
- [51] R. Natarajan, J. Williams, and G. Andersson, "Modeling changes in intervertebral disc mechanics with degeneration," *J. Bone Joint Surgery Am.* **88**(2), 36-40 (2006).
- [52] Viscosity, <http://hypertextbook.com/physics/matter/viscosity> (date last viewed 06/03/09), The Physics Hypertextbook by Glenn Elert, (2008).

- [53] J. Gennisson, T. Baldeweck, M. Tanter, S. Catheline, M. Fink, L. Sandrin, C. Cornillon, and B. Querleux, "Assessment of elastic parameters of human skin using dynamic elastography," *IEEE Trans. Ultrason. Ferroelectr. Freq. Control* **51**(8), 980-989 (2004).
- [54] M. Jahed and S. J. Lai-Fook, "Stress wave velocity measured in intact pig lungs with cross-spectral analysis," *J. Appl. Physiol.* **76**(2), 565-571 (1994).
- [55] E. L. Mazuchowski and L. E. Thibault, "Biomechanical properties of the human spinal cord and pia mater," ASME Key Biscayne, FL. Presented at the Summer Bioengineering Conference (2003).
- [56] J. P. Bérenger, "A perfectly matched layer for absorption of electromagnetic waves," *J. Comput. Phys.* **114**, 185-200 (1994).
- [57] F. H. Drossaert and A. Giannopoulos, "A non-split complex frequency shifted PML based on recursive integration for FDTD modeling of elastic waves," *Geophysics* **72**(2), T9-T17 (2007).
- [58] F. Collino and C. Tsogka, "Application of the perfectly matched absorbing layer model to the linear elastodynamic problem in anisotropic heterogeneous media," *Geophysics* **68**, 294-307 (2001).
- [59] Q. H. Liu and J. Tao, "The perfectly matched layer for acoustic waves in absorptive media," *J. Acoust. Soc. Am.* **102**(4), 2072-2082 (1997).
- [60] J. Virieux, "P-SV wave propagation in heterogeneous media: velocity–stress finite-difference method," *Geophysics* **51**, 889-901 (1986).
- [61] K. S. Yee, "Numerical solution of initial boundary value problems involving Maxwell's equations in isotropic media," *IEEE Trans. Antennas and Propagation* **14**, 302-307 (1996).
- [62] C. Schroder and W. Scott, Jr., "On the stability of the FDTD algorithm for elastic media at a material interface," *IEEE Trans. Geosci. Remote Sensing* **40**(2), 474-481 (2002).
- [63] G. Eason, J. Fulton, and I. N. Sneddon, "The generation of waves in an infinite elastic solid by variable body forces," *Phil. Trans. Royal Soc. London (A)* **248**, 575-607 (1956).
- [64] S. Ramakrishnan, S. Udpa, and L. Udpa, "A numerical model simulating sound propagation in human thorax (Periodical style – Accepted for publication)," *Proceedings of IEEE International Symposium on Biomedical Imaging* (2009), to be published.

- [65] S. Ramakrishnan, S. Udpa, and L. Udpa, "A viscoelastic 2D finite-difference time-domain model of sound propagation in human thorax (Periodical style – Submitted for publication)," *J. Acoust. Soc. Am.*, submitted for publication.
- [66] H. A. Mansy, T. J. Royston, R. A. Balk, and R. H. Sandler, "Pneumothorax detection using pulmonary acoustic transmission measurements," *Med. Biol. Eng. Comput.* **40**, 520-525 (2002).
- [67] D. Lichenstein, G. Meziere, P. Biderman, and A. Gepner, "The 'lung point': an ultrasound sign specific to pneumothorax," *Intensive Care Med.* **29**, 1434-1440 (2000).
- [68] H. A. Mansy, T. J. Royston, R. A. Balk, and R. H. Sandler, "Pneumothorax detection using computerised analysis of breath sounds," *Med. Biol. Eng. Comput.* **40**, 526-532 (2002).
- [69] S. Ramakrishnan, S. Udpa, and L. Udpa, "A numerical model to study auscultation sounds under pneumothorax conditions (Periodical style – Accepted for publication)," *Proceedings of the 31st Annual International Conference of IEEE Engineering in Medicine and Biology Society* (2009), to be published.
- [70] B. D. Van Veen and K. M. Buckley, "Beamforming: A Versatile Approach to Spatial Filtering," *IEEE ASSP Magazine* **5**(5), 4-24 (1988).
- [71] I. A. McCowan, D. C. Moore, and S. Sridharan, "Near-field Adaptive Beamformer for Robust Speech Recognition," *Digital Signal Processing* **12**(1), 87-106 (2002).
- [72] H. Krim and M. Viberg, "Two decades of array signal processing research: the parametric approach," *IEEE Signal Processing Magazine* **13**(4), 67-94 (1996).
- [73] J. G. Berryman, L. Borcea, G. C. Papanicolaou, and C. Tsogka, "Statistically stable ultrasonic imaging in random media," *J. Acoust. Soc. Am.* **112**(4), 1509-1522 (2002).
- [74] Y. R. Zheng, R. A. Goubran, and M. El-Tanany, "Robust near-field adaptive beamforming with distance discrimination," *IEEE Trans. Speech and Audio Processing* **12**(5), 478-488 (2004).
- [75] Y. Jin and B. Friedlander, "Detection of distributed sources using sensor arrays," *IEEE Trans. Signal Processing* **52**(6), 1537-1548(2004).

MICHIGAN STATE UNIVERSITY LIBRARIES



3 1293 03063 0556